

Submitted by  
**Dipl.-Ing.**  
**Ida Aichinger**

Submitted at  
**Institute of Financial  
Mathematics and Ap-  
plied Number Theory**

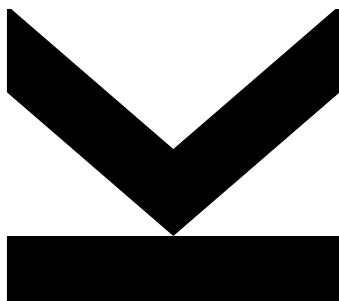
Supervisor and  
First Examiner  
**Univ.-Prof. Dr.**  
**Gerhard Larcher**

Second Examiner  
**Privatdoz. Dipl.-Ing.**  
**Dr.techn.**  
**Michael Benedikt**

Co-Supervisor  
**Roberto Kersevan**

October, 2017

# Vacuum Simulations in High Energy Accelerators and Distribution Proper- ties of Continuous and Discrete Particle Motions



Doctoral Thesis  
to obtain the academic degree of  
**Doktorin der technischen Wissenschaften**  
in the Doctoral Program  
**Technische Wissenschaften**



---

---

## Abstract

The underlying thesis on mathematical simulation methods in application and theory is structured into three parts.

The first part sets up a mathematical model capable of predicting the performance and operation of an accelerator's vacuum system based on analytical methods. A coupled species-balance equation system describes the distribution of the gas dynamics in an ultra-high vacuum system considering impacts of conductance limitations, beam induced effects (ion-, electron-, and photon-induced desorption), thermal outgassing and sticking probabilities of the chamber materials. A new solving algorithm based on sparse matrix representations, is introduced and presents a closed form solution of the equation system. The model is implemented in a Python environment, named PyVasco, and is supported by a graphical user interface to make it easy available for everyone. A sensitivity analysis, a cross-check with the Test-Particle Monte Carlo simulation program Molflow+ and a comparison of the simulation results to readings of the Large Hadron Colliders (LHC) pressure gauges validate the code. The computation of density profiles considering several effects (as mentioned above) is performed within a short computation time for indefinitely long vacuum systems. This is in particular interesting for the design of a stable vacuum system for new large accelerators like the Future Circular Colliders (FCC) with 100 km in circumference. A simulation of the FCC is shown at the end of this part. Additionally, PyVasco was presented twice at international conferences in Rome and Berlin and has been submitted in July with the title "Analytical vacuum simulations in high energy accelerators for future machines based on the LHC performance" to the Journal "Physical Review Accelerator and Beams".

The second and third part of the thesis study properties of quasi-Monte Carlo (QMC) methods in the scope of the special research project "Quasi-Monte Carlo methods: Theory and Applications". Instead of solving a complex integral analytically, its value is approximated by function evaluation at specific points. The choice of a good point set is critical for a good result. It turned out that continuous curves provide a good tool to define these point sets. So called "bounded remainder sets" (BRS) define a measure for the quality of the uniform distribution of a curve in the unit-square. The trajectory of a billiard path with an irrational slope is especially well distributed.

Certain criteria to the BRS are defined and analysed in regard to the distribution error. The idea of the proofs is based on Diophantine approximations of irrational numbers and on the unfolding technique of the billiard path to a straight line in the plane. New results of the BRS for the billiard path are reported to the “Journal of Uniform Distribution”.

The third part analyses the distribution of the energy levels of quantum systems. It was stated that the eigenvalues of the energy spectra for almost all integrable quantum systems are uncorrelated and Poisson distributed. The harmonic oscillator presents already one counter example to this assertion. The particle in a box on the other hand obtains these properties. This thesis formulates a general statement that describes under which conditions the eigenvalues do not follow the poissonian property. The concept of the proofs is based on the analysis of the pair correlations of sequences. The former particle physicist Ian Sloan also exposed this topic and he became specialized as a skilled mathematician in this field. To honour his achievements a Festschrift for his 80th birthday is written and the results of the work of this thesis are published there. The book will appear in 2018.

---

---

## Zusammenfassung

Die vorliegende Dissertation behandelt drei Themenschwerpunkte im Bereich der mathematischen Simulation in Anwendung und Theorie.

Der erste Teil wurde am Kernforschungszentrum CERN erarbeitet und beschäftigt sich mit dem Erstellen eines passenden mathematischen Modells um die Vakuumqualität in einem Teilchenbeschleuniger zu bestimmen. Am CERN werden Teilchen, meist Protonen, auf nahezu Lichtgeschwindigkeit beschleunigt und mit extrem hoher kinetischer Energie zur Kollision gebracht. Für diesen Vorgang ist ein Vakuum in der Strahlröhre absolute Voraussetzung, dessen Erhalt aber durch zahlreiche, dynamische Phänomene ständig beeinträchtigt wird. Ein System von gekoppelten Massenbilanzgleichungen der residualen Gasteilchen beschreibt dessen Verteilung und berücksichtigt ebenso den Einfluss von Senken (Vakuumpumpen) und Quellen (Strahl induzierte Effekte). Dieses wird bestmöglichst gelöst und anschließend unter dem Namen “PyVasco” in einer programmierspezifischen Python-Umgebung implementiert. PyVasco wurde anschließend ausführlich an Hand von Sensitivitätsanalysen, Monte-Carlo Simulationen und mit Real-Case Szenarien des Vakuumsystems des Large Hadron Collider (LHC) getestet. Nun soll PyVasco ein vertrauenswürdiges Simulationsprogramm darstellen, um das Vakuumsystems von zukünftigen Beschleunigern wie den “Future Circular Colliders” (FCC) zu analysieren. PyVasco wurde zwei Mal auf einer internationalen Konferenz in Rom und in Berlin präsentiert und wurde mit dem Titel: “Analytical methods for vacuum simulations in high energy accelerators for future machines based on LHC performances” im Journal “Physical Review-Accelerator and Beams” eingereicht.

Der zweite und dritte Teil der Dissertation beschäftigt sich mit Eigenschaften von Quasi-Monte Carlo (QMC) Methoden und wird von Univ.-Prof. Dr. Gerhard Larcher (JKU) im Rahmen des SFB-Forschungsprojekts “Quasi-Monte Carlo Methods: Theory and Applications” betreut. Anstatt komplexe Integrale analytisch zu lösen, wird deren Wert mit QMC-Methoden durch Funktionsauswertungen an Punkten angenähert. Die Wahl einer optimalen Punktmenge ist kritisch für ein gutes Ergebnis. Es hat sich herausgestellt, dass stetige Bewegungen eine gute Möglichkeit bieten, um diese Punktmengen festzulegen. Sogenannte Regionen mit beschränkten Restmengen (BRS) definieren ein Maß, für die Qualität der Gleichverteilung einer Bewegung in einem Einheitsquadrat.

Die Trajektorie einer Billardkugel mit irrationalem Anfangswinkel ist besonders gut gleichverteilt. Bestimmte Kriterien an die BRS werden aufgestellt und detailgenau analysiert. Die Beweise basieren auf diophantischen Approximationen von irrationalen Zahlen und auf der Entfaltung des Billiardpfades zu einer Geraden in der Ebene. Neue Resultate der BRS für Billiardbewegungen wurden im “Journal of Uniform Distribution Theory” eingereicht.

Im dritten Teil wird die Verteilung der Energielevel von Quantensystemen analysiert. Es wurde behauptet, dass die Eigenwerte der Energiespektra für beinahe alle integrierbaren Systeme unkorreliert und Poisson verteilt sind. Der harmonische Oszillator stellt bereits ein Gegenbeispiel dieser These dar. Das Teilchen in einer Box andererseits bestätigt die Behauptung. Es wird hier eine allgemeine Aussage formuliert, die beschreibt unter welchen Bedingungen die Eigenwerte nicht Poisson verteilt sind. Die Beweisidee basiert auf dem Studium der Paar-Korrelationen von Folgen. Der ehemalige Teilchenphysiker und mittlerweile Mathematiker Ian Sloan hat sich ebenso mit diesem Thema auseinander gesetzt. Ihm zu Ehren wird eine Festschrift zu seinem 80. Geburtstag erstellt und die Forschungsergebnisse von diesem Teil der Dissertation werden in dieser Festschrift im Springer Verlag publiziert. Das eingereichte Paper dazu wurde bereits angenommen.

---

## Acknowledgements

---

I am very grateful for the opportunity to work on my PhD thesis at CERN, where scientists with various specialisations meet. My horizon on general science and research increased by combining solution concepts and ideas from physics, mathematics, chemistry and computer sciences. To all of the people I met here, especially to the members of the Vacuum, Surface and Coating group (VSC), I express my sincere thanks!

In particular, I would like to express my gratitude to my CERN supervisor Roberto Kersevan, one of the world experts in vacuum science (ESRF, ITER, Cornell University Chicago) who was available any-time for critical discussions about particle physics, vacuum science and daily-life problems. We met usually twice a day for a coffee break and these informal reunions were a privilege that not many PhD students can enjoy.

My university supervisor Gerhard Larcher, a world-expert in the field of quasi Monte Carlo methods, equally deserves my gratitude. He made it possible for me to write a mathematical thesis in the framework of physical applications. To strengthen my fundamental mathematical proofing skills he invited me to join his research group at JKU and supported and taught me in the field of Quasi Monte Carlo methods.

The third person, I am deeply thankful for, is my group leader at CERN Paolo Chiggiato. Despite his high position to manage the entire vacuum group, he dedicated time and energy to follow the progress of all the PhD students in his group. We had a meeting every two weeks to present our progress, discuss problems and give an outlook for our work. These meetings were challenging, but they helped to reach my goals.

Moreover, I would like to thank the FCC-project leader Michael Benedikt, who established the contact to the vacuum group - to Paolo and Roberto at the beginning of my thesis and he joins now the examination committee at my doctoral defense. He always gave me a friendly “hello” and showed interest in my work progress when we met.

Next, I want to thank my family and my boyfriend Alejandro. They all followed my progress with big interest, gave me useful advice, listened to my presentations and proof-read my texts. After

tough periods, we planned nice holidays and activities together such as skiing and mountaineering in the Swiss and French Alps or simply enjoyed a great home-made dinner.

A special thank you is also dedicated to Siyuan Sun, a particle physicist from Harvard University, who introduced me to the fascinating field of quantum mechanics, so that I could develop my mathematical research on the basic-fundamental understanding, he gave me.

Additionally, I am deeply thankful to all the amazing people who I met here at CERN coming from different nations, inviting me to discover their research area in different fields of physics and spending time together with me in the beautiful mountains of this area. Lisa, Lucie, Anne-Laure, Quentin, Marlene, Ingmar, Marton, Marta, Volker and Tenar are only a few names that I like mention.

Last but not least I thank the library at CERN that provides an amazing source of information. Within a few days I had the chance to order any science book.

Ida Aichinger  
Geneva, October 2017

---

# Contents

---

<b>Summary of Paper</b>	x
<b>I. Detailed and Supplementary Presentation of Scientific Results</b>	<b>1</b>
<b>1. Introduction</b>	<b>3</b>
1.1. Simulation techniques - theory and applications . . . . .	3
1.2. Organization of the thesis . . . . .	5
<b>2. Vacuum simulations in high energy accelerators</b>	<b>7</b>
2.1. Ultra high vacuum . . . . .	8
2.1.1. Specification of beam chamber: . . . . .	8
2.1.2. Sinks and Sources . . . . .	9
2.2. Mathematical model . . . . .	13
2.2.1. Assumptions . . . . .	14
2.2.2. Schematic of the model . . . . .	15
2.2.3. Single-gas model . . . . .	15
2.2.4. Multi-gas model . . . . .	20
2.2.5. Appendix to Multi-gas model . . . . .	23
2.3. Computer implementation . . . . .	27
2.4. Simulation results for the FCC . . . . .	30
2.4.1. FCC-hh . . . . .	31
2.4.2. FCC-ee . . . . .	38
2.5. Validation and error estimation . . . . .	38
2.6. Physics at the FCC . . . . .	39
2.7. Summarized parameter and variable acronyms . . . . .	40
<b>3. Sets of Bounded Remainder for the Billiard on a Square</b>	<b>45</b>
3.1. Monte-Carlo vs. Quasi Monte Carlo methods . . . . .	46
3.1.1. Uniformly distributed curves . . . . .	49

## CONTENTS

3.2.	Summary of paper and an expanded detailed proof description . . . . .	51
3.2.1.	BRS for the billiard in a square . . . . .	56
3.2.2.	Exceptions: Not BRS for the billiard in a square . . . . .	56
<b>4.</b>	<b>Distribution Properties of Quasi Energy Spectra in Quantum Mechanics</b>	<b>61</b>
4.1.	Introduction to Quantum Mechanics . . . . .	61
4.2.	Distribution of eigen-energy levels in integrable quantum systems . . . . .	63
4.3.	Mathematical aspects of the nearest neighbour spacing problem . . . . .	64
4.3.1.	Pair correlation statistics for certain sequences . . . . .	66
4.3.2.	Conditions for a sequence to have the asymptotical Poissonian property .	69
4.4.	Examples of integrable quantum systems . . . . .	72
4.4.1.	1-dimensional harmonic oscillator . . . . .	73
4.4.2.	Particle in a box . . . . .	74
4.4.3.	The hydrogen atom . . . . .	75
<b>II.</b>	<b>Papers</b>	<b>77</b>
<b>Paper 1:</b>	<b>Analytical methods for vacuum simulations in high energy accelerators for future machines based on LHC performances</b>	<b>79</b>
<b>Paper 2:</b>	<b>Sets of Bounded Remainder for the Billiard on a Square</b>	<b>99</b>
<b>Paper 3:</b>	<b>On Quasi-energy-spectra, pair correlations of sequences and additive combinatorics</b>	<b>113</b>
<b>List of Figures</b>		<b>131</b>
<b>List of Tables</b>		<b>132</b>
<b>Bibliography</b>		<b>133</b>
<b>Curriculum</b>		<b>143</b>

---

## List and Summary of Accompanying Papers

---

During my doctoral student time, I submitted three papers [1–3] to peer-reviewed journals. The title, the abstract and the name of the journals are summarized below. The entire papers are attached in Part II of the present thesis in their original version.

**Paper 1** “Analytical methods for vacuum simulations in high energy accelerators for future machines based on LHC performances”,  
submitted to: Journal Physical Review Accelerator and Beams,  
by Ida Aichinger, Roberto Kersevan and Paolo Chiggiato

The Future Circular Collider (FCC), currently in the design phase, will address many outstanding questions in particle physics. The technology to succeed in this 100 km circumference collider goes beyond present limits. Ultra-high vacuum conditions in the beam pipe is one essential requirement to provide a smooth operation. Different physics phenomena as photon-, ion- and electron- induced desorption and thermal outgassing of the chamber walls challenge this requirement. This paper presents an analytical model and a computer code PyVasco that supports the design of a stable vacuum system by providing an overview of all the gas dynamics happening inside the beam pipes. A mass balance equation system describes the density distribution of the four dominating gas species H<sub>2</sub>, CH<sub>4</sub>, CO and CO<sub>2</sub>. An appropriate solving algorithm is discussed in detail and a validation of the model including a comparison of the output to the readings of LHC gauges is presented. This enables the evaluation of different designs for the FCC.

**Paper 2** “Sets of Bounded Remainder for the Billiard on a Square”  
submitted to: ”Journal of Uniform Distribution Theory“  
by Ida Aichinger, Gerhard Larcher

We study sets of bounded remainder for the billiard on the unit square. In particular, we note that every convex set S whose boundary is twice continuously differentiable with positive curvature at every point, is a bounded remainder set for almost all starting angles  $\alpha$  and every starting point  $x$ . We show that this assertion in general does not hold for all irrational starting angles  $\alpha$ .

**Paper 3** “On Quasi-energy-spectra, pair correlations of sequences and additive combinatorics” paper accepted to appear in a book that will be published with the title: ”80th birthday Festschrift for Ian H Sloan“

by Ida Aichinger, Christoph Aistleitner, Gerhard Larcher

The investigation of the pair correlation statistics of sequences was initially motivated by questions concerning quasi-energy-spectra of quantum systems. However, the subject has been developed far beyond its roots in mathematical physics, and many challenging number-theoretic questions on the distribution of the pair correlations of certain sequences are still open. We give a short introduction into the subject, recall some known results and open problems, and in particular explain the recently established connection between the distribution of pair correlations of sequences on the torus and certain concepts from additive combinatorics. Furthermore, we slightly improve a result recently given by Jean Bourgain.

**Part I.**

**Detailed and Supplementary**

**Presentation of Scientific Results**



# CHAPTER 1

---

## Introduction

---

### 1.1. Simulation techniques - theory and applications

The European Organization for Nuclear research (CERN) is currently the largest particle physics laboratory in the world. Particles are accelerated to extremely large energies (7 TeV) to later collide them among each other in one of the four main experiments (collision points) as illustrated in Fig. 1.1. The particle trajectories after the collisions are analysed and by doing so physicists can have an idea of what happened moments after the big bang and therefore provide a deeper understanding of the fundamentals of the universe. Despite the great success of the discovery of the last piece of the Standard Model, the Higgs boson, in 2012 at the Large Hadron Collider (LHC) there are still several important fundamental questions unanswered. Dark matter constitutes about 85% of the universe total mass and this mass is not described with the Standard Model. The theory of super-symmetry is an attempt to go beyond the Standard Model and to find out about the link between bosons and fermions in the field of space-time symmetry. This implies an upgrade of the LHC at CERN in terms of an energy increase up to 100 TeV or an e+e- collider in the range of 500-600 GeV. Both solutions can be achieved by using a larger accelerator referred as the Future Circular Colliders: FCC-hh and FCC-ee with 100 km in circumference [4]. A higher energy of the beam particles comes along with the demand of a five times better vacuum quality inside the beam pipes than in the LHC to guarantee the same beam life time of 100 hours. The vacuum system in the LHC represents already the largest in the world with a H<sub>2</sub>-equivalent density of 10<sup>15</sup> particles/m<sup>3</sup> compared to 10<sup>26</sup> particles in the atmosphere for the same volume. In addition, vacuum related beam-induced effects increase with a higher beam energy. Photons, electrons and ions will bombard the chamber wall with a higher and more intense rate and consequently generate molecular desorption that leads to an unwanted rise in the residual gas particle density [5–8]. To succeed in this very challenging task, good simulation programs are required, which combine all influencing factors and give a realistic estimation of the residual gas particle density as an output.

## 1.1. SIMULATION TECHNIQUES - THEORY AND APPLICATIONS

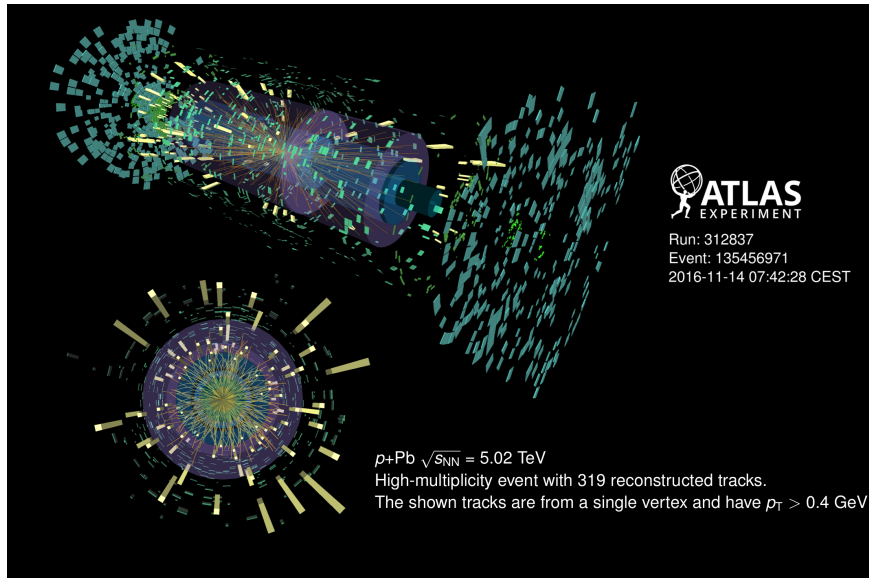


**Figure 1.1.:** Collision event in the ATLAS experiment.

Setting up a suitable simulation program addressed to large scale-accelerators is the content of the first paper [1]. Different scenarios for surface conditioning and beam energy increase can be analysed with it. The layout of the pumping system can be studied and the prevailing residual gas particle density can serve as a background noise indicator for particle physics analysis in the experimental zones. There exist several approaches to describe the simulation of residual gas particles. The most general one is the nonlinear integro-differential Boltzmann equation. However, the solution of the Boltzmann equation requires excessive computational effort due to the complicated structure of the collision integral. This is a formidable task in many cases. The present thesis and paper [1] suggest an analytic closed form solution by asymptotically approaching the model with a diffusion equation. Probabilistic Monte Carlo simulations present another good alternative to simulate the trajectories of each single particle. A realisation of this approach is given with the program Molflow+, developed as well at CERN.

In general, Monte Carlo simulation gained prominence in the field of numerical solution methods, especially due to the rapid development of computer power. An analytical solution of high dimensional integrals cannot be found in many mathematical applications and must be fast approximated by function evaluation at different points.

$$\int_{\mathbb{R}^s} f(\boldsymbol{x}) d\boldsymbol{x} \sim \frac{1}{N} \sum_{n=0}^{N-1} f(\boldsymbol{x}_n) \quad (1.1)$$

*Monte-Carlo integration* uses independent (pseudo-) random samples for the quadrature points  $\boldsymbol{x}_n$  in the numerical integration in (1.1). *Quasi-Monte Carlo integration* on the other hand describes a

## 1. INTRODUCTION

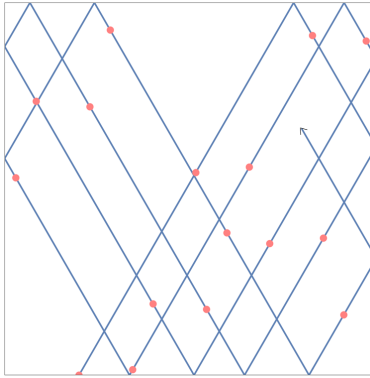


**Figure 1.2.:** Selecting a point set for QMC-simulation from a continuous motion in the unit square.

computing method for high-dimensional numerical integration, where deterministic most carefully chosen quadrature points  $x_n$  (that do not imitate randomness) are used (illustrated in Fig 1.2). The second paper [2] focuses on the establishment of this deterministic point sets, by following a motion in a unit square and extract points from it. It is very interesting to conclude that deriving a point set from a continuous motion may deliver under good conditions a very small error term in dimensions 2 and 3 compared to other well-verified methods [12]. The continuous motion is in this thesis represented by the trajectory of a typical billiard ball in a square.

Billiard path present in a completely different context another very important simulation tool to support the understanding on the quantum mechanics (QM) from integrable to chaotic systems [13]. The propagation of a particle in a box that follows a billiard motion is equivalent to the stationary wave equation (Helmholtz equation). In the context of this thesis, we study the discrete energy spectra of integrable quantum systems. It was stated once that these spectra are all obeying the Poissonian distribution law [14]. The spectrum of the quantum harmonic oscillator however is equi-distributed and thus is not coinciding with this assumption. The paper [3] analyses in a general framework when mathematical sequences obey the Poissonian property and this thesis extends the paper with concrete examples of quantum mechanic systems. One of these examples discusses also the energy spectra of the hydrogen atom. Ian Sloan, to whom the paper [3] is dedicated, analysed in his early research year how to derive information of the spectra of an ionized helium atom from the hydrogen atom [15].

## 1.2. Organization of the thesis

The present thesis is organized in a cumulative style consisting of three peer-reviewed papers [1–3], that are attached as Part 2 at the end of this document. The most fundamental scientific contributions are found in these papers. The time and work investigated in the paper has to be seen with a ratio of  $\frac{1}{2}$ ,  $\frac{1}{6}$  and  $\frac{1}{3}$  among the papers.

## 1.2. ORGANIZATION OF THE THESIS

In addition one chapter of this thesis is dedicated to each paper to introduce its content, give scientific background, extend the proofs with technical details and present further examples for a better understanding. Chapter 2 considers an analytic method, that describes the vacuum dynamics in the beam chamber of an accelerator. The mathematical model is more specifically described and the results of the paper are extended with simulations for the design of a new 100-km long accelerator. Chapter 3 deals with properties of quasi Monte Carlo methods. The methodology of this numerical method is introduced and a new concept that analyses uniformity of curves instead of point sets is discussed. Chapter 4 studies statistical properties of the distribution of energy levels in quantum systems. The framework of quantum mechanics is introduced.

## CHAPTER 2

---

### Vacuum simulations in high energy accelerators

---

The Future Circular Collider (FCC) study develops concepts for a 100 km circumference accelerator, which brings hadrons (FCC-hh), leptons (FCC-ee) or hadron-lepton (FCC-he) into collision [4]. High luminosity proton-proton collisions are the main focus of the study with an energy frontier up to 100 TeV in the centre of mass to address some of the most fundamental open issues in particle physics. The first conceptual design report has to be ready by the end of 2018. Up to this time, scientists and engineers from 32 different countries gather together to explore new challenges. This is also the time, in which new simulation codes are developed. My task was to provide a code to predict the performance and operation of the FCC’s vacuum system, taking several static and dynamic effects into account. The code also had to be flexible with respect to modifications of the input parameters and to provide results within a reasonable computation time. These demands are met in the PyVasco (VAcuum Stability Code written in Python) software that predicts the performance and operation of any accelerator’s vacuum system. The core of the code is founded on the idea of VASCO [16] and it presents a mathematical model of four coupled differential equations to describe the mass-balance of the four dominating gas species H<sub>2</sub>, CH<sub>4</sub>, CO and CO<sub>2</sub>. The theory and a preliminary design of the collision points was presented at the FCC week in 2016 and 2017, respectively [17, 18] and a compact over-all description of the model will be published in “Physical Review Accelerators and Beams” [1]. A comparison of the simulation outputs to similar models and in particular to gauge readings of the Large Hadron Collider (LHC) validates the implemented theory of PyVasco, that is as well described in detail in [1].

The following text, should give supplementary information to [1] on vacuum, the calculation methods used and the FCC-study. The latter is in particular extended with a PyVasco simulation of the Interaction Point of the FCC.

## 2.1. Ultra high vacuum

Ultra-high vacuum (UHV) in the beam pipes of particle accelerators is crucial to circulate particles at high energies and to minimize the nuclear scattering of the proton beam with the residual gas molecules. Low background noise enables high precision measurements of the particle collisions. Furthermore it is the basis to maintain the superconducting state in the cryogenic regions, it avoids activation of accelerator components and it minimizes radio-protection issues for the personnel. A lower residual gas particle density, or equivalently a lower prevailing pressure of the vacuum chamber, means a higher-quality vacuum. In addition to the gas composition, a lower atomic number of the gas species generate less nuclear scattering. Some characteristic data and a classification are summarized in the Table 2.1 below and derived from [19, 20].

**Table 2.1.:** A typical classification of vacuum [20], valid for a room temperature system. Pressure and density are related via the ideal gas law and the mean free path describes the average distance that a particle travels before it hits the wall.

vacuum quality	abbreviation	pressure [mbar]	particle density [ $1/m^3$ ]	mean free path [m]
atmospheric pressure		$10^{13}$	$2.7 \cdot 10^{25}$	$68 \cdot 10^{-9}$
high vacuum	HV	$10^{-3} - 10^{-7}$	$10^{19} - 10^{15}$	$10^{-2} - 10^3$
ultra high vacuum	UHV	$10^{-7} - 10^{-12}$	$10^{15} - 10^{10}$	$10^3 - 10^8$
extreme high vacuum	XHV	$< 10^{-12}$	$< 10^{10}$	$> 10^8$

### 2.1.1. Specification of beam chamber:

Temperature, geometry and the material specify the beam chamber characteristics. These parameters define the so called static-vacuum, where no beam circulates in the chambers [6, 21–25].

**Temperature:** The operating temperature in accelerators is mainly at room-temperature. Only high energy circular hadron accelerators as the LHC and the FCC-hh are kept partly at cryogenic conditions to allow the installation of superconducting magnets. Temperature influences the speed of the residual gas particles and the material properties in terms of desorption rates.

**Geometry:** Accelerators tend to comprise long narrow beam tubes, just large enough in diameter to accommodate the beam-stay-clear aperture. The counter rotating beams circulate mainly in separate beam pipes (LHC, FCC) that join into one common chamber in straight sections close to the beam-collision points. The geometry defines the conductance [26] of the vacuum chamber and the impact of material effects due to the size of the lateral surface.

## 2. VACUUM SIMULATIONS IN HIGH ENERGY ACCELERATORS

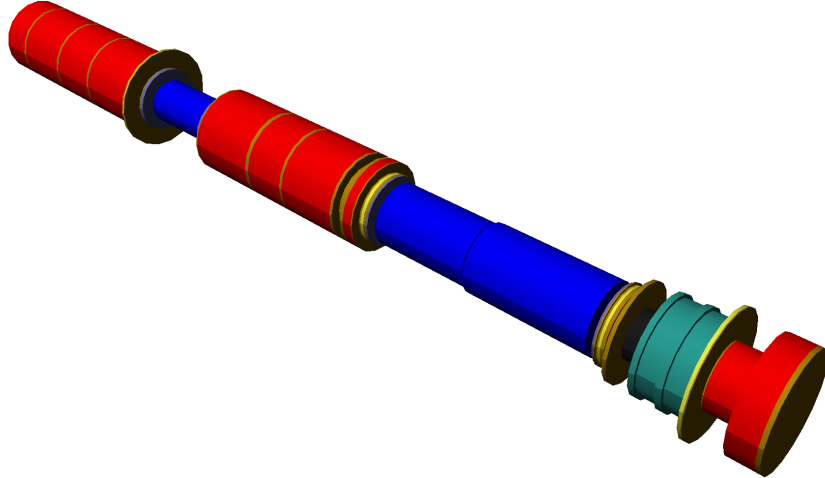


**Figure 2.1.:** Beam pipe of an accelerator, different colours correspond to different materials.

**Material:** The vacuum chambers are made out of a variety of materials illustrated for the LHC in Fig. 2.1. Most typically they are made out of copper due to its lower electrical resistivity, its superior opacity to high energy photons and related radio-protection issues. A beamscreen<sup>1</sup> made out of stainless steel with internal copper coating is implemented in the cryogenic areas to protect the cold bore (at 1.9 K) from beam-induced heating effects [27]. Additionally, a thin-film coating, or special material treatments may improve the materials characteristics in regards of its distributed pumping property.

### 2.1.2. Sinks and Sources

The ultimate goal in the vacuum systems design is to get enough pumping to cope with the gas load generated by desorption. Here are the most common sinks and sources reviewed:

**Thermal outgassing:** The material of the beam chamber randomly releases gas molecules. Thermal outgassing is the only source in absence of the beam.

**Desorption due to residual gas ionization:** The particle beam ionizes the molecules of the residual gas in the beam chamber producing free electron ion-pairs (ion induced desorption). The local ion production rate per unit volume in the beam chamber is given by [8, 28, 29]:

$$\frac{dn_{ion}}{dt} = \mathbf{H}_{ion} \cdot \dot{I}_{beam} \circ \mathbf{n}_{gas}, \quad (2.1)$$

---

<sup>1</sup>an additional perforated pipe inside the beam chamber

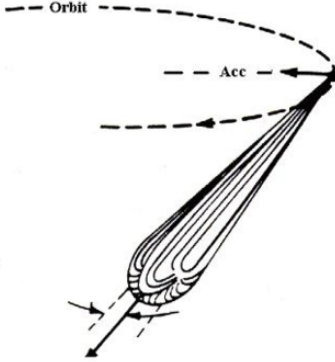


**Figure 2.2.:** The photons are generated in a sharp forward direction.

where  $\circ$  describes a component-wise multiplication and  $\mathbf{H}_{\text{ion}}$  is the ionization cross section matrix of the residual gases,

$$\mathbf{H}_{\text{ion}} = \begin{pmatrix} \eta_{\text{H}_2^+ \rightarrow \text{H}_2} & \eta_{\text{CH}_4^+ \rightarrow \text{H}_2} & \eta_{\text{CO}^+ \rightarrow \text{H}_2} & \eta_{\text{CO}_2^+ \rightarrow \text{H}_2} \\ \eta_{\text{H}_2^+ \rightarrow \text{CH}_4} & \eta_{\text{CH}_4^+ \rightarrow \text{CH}_4} & \eta_{\text{CO}^+ \rightarrow \text{CH}_4} & \eta_{\text{CO}_2^+ \rightarrow \text{CH}_4} \\ \eta_{\text{H}_2^+ \rightarrow \text{CO}} & \eta_{\text{CH}_4^+ \rightarrow \text{CO}} & \eta_{\text{CO}^+ \rightarrow \text{CO}} & \eta_{\text{CO}_2^+ \rightarrow \text{CO}} \\ \eta_{\text{H}_2^+ \rightarrow \text{CO}_2} & \eta_{\text{CH}_4^+ \rightarrow \text{CO}_2} & \eta_{\text{CO}^+ \rightarrow \text{CO}_2} & \eta_{\text{CO}_2^+ \rightarrow \text{CO}_2} \end{pmatrix},$$

where the entry  $\eta_{i+ \rightarrow j}$  describes the probability that an ion of species  $i$  desorbs a molecule of species  $j$ . The cross section differs for the different residual gases. The desorption of  $\text{H}_2$  is most probable, because  $\text{H}_2$  dissolves in the bulk of all metals as  $\text{H}^+$  and becomes available on the surface for recombination as  $\text{H}_2^+$  and desorption.

**Desorption due to photon bombardment:** Synchrotron radiation is the emission of photons that occurs when a particle beam undergoes a transverse acceleration [7,30–33], in particular in bending magnets and also in quadrupoles, when the beam circulates in an off-axis position. The photons are emitted in the direction tangent to the beam direction (see Fig. 2.2). Consequently, the generation of the photons and its impingement on the wall can spread over several meters.

The effect of the desorption depends on the amount (photon flux  $\dot{\Gamma}$ ) and on the energy (power  $P$ ) of the photons per time [34, 35]. The power and the flux can be calculated for a bending magnet and an ultra-relativistic beam by the following term:

$$P_{ph} = \frac{e}{6\pi\epsilon_0\rho^2} \cdot \left(\frac{E}{m_0}\right)^4 \cdot I \quad (2.2)$$

and

$$\dot{\Gamma}_{ph} = \frac{5\sqrt{3}}{24\pi\epsilon_0\hbar\rho c} \cdot \frac{E}{m_0} \cdot I \quad (2.3)$$

## 2. VACUUM SIMULATIONS IN HIGH ENERGY ACCELERATORS

Both sizes depend in particular on the rest-mass  $m_0$  and the energy  $E$  of the beam-particles, on the beam current  $I$  and on the bending radius  $\rho$  of the magnets. All other variables describe constants that are listed in Table 2.11. Particles with low-mass and high-energy produce the most radiation, hence circular electron machines are limited in their energy by the energy losses due to the emission of synchrotron radiation. That is why FCC-ee gets to only 175 GeV maximum energy, while the FCC-hh is designed for 50000 GeV. A part of the impinging photons is reflected, others are absorbed and therefore can cause a photon-induced desorption. These are photons that have an energy larger than the work function of the beam chamber's material<sup>2</sup>. The energy spectrum from the synchrotron radiation is characterized by the critical energy (see also Fig. 2.3),

$$E_c = \frac{3}{2} \frac{\hbar c}{\rho} \left( \frac{E}{m_0} \right)^3, \quad (2.4)$$

i.e. the median of the power distribution. The impinging photons, depending on their energy, have a probability of generating gas desorption. For a  $E_c \gg 4$  the following relation could be experimentally observed:

$$\eta_{ph} \sim E_c^\beta, \quad (2.5)$$

where  $\beta$  assumes values close to one ( $\beta = 1 \pm 0.2$ ) [36].

**Desorption due to the electron cloud phenomena:** (cited from [1]) The beam can generate some electrons from synchrotron radiation, impinging ionized gas molecules and spontaneous desorption induced by sufficiently high electromagnetic fields [39]. These primary electrons may be accelerated by the bunched charged beam that hit the chamber wall and may produce a cascade of secondary electrons (see Fig. 2.4). The electrons are accelerated towards the positively charged beam, they cross the chamber and hit the wall again on the opposite side - producing more electrons and lead eventually to beam instabilities and gas desorption. This phenomenon depends in a complex way on the beam and chamber parameters and also on the bunch filling pattern. A CERN proprietary software PyECloud [40] addresses this phenomenon. Based on observations, it can be concluded that the bigger the aperture of the vacuum chamber, the longer is the duration that an electron is accelerated, the bigger is the surface where desorption can take place and the higher is the electron induced desorption. In addition, it has been observed in the LHC that the reduction of the bunch spacing to 25ns causes a significantly increased electron cloud effect in comparison to 50ns or to 100ns [41].

**Distributed pumping:** The surface of the vacuum chamber may provide sticking probabilities for the residual gas particles. Special coating techniques and material treatments have been developed to increase this factor. For instance, room temperature areas are additionally coated with a mi-

---

<sup>2</sup>> 4 eV for copper, the most common material in accelerators

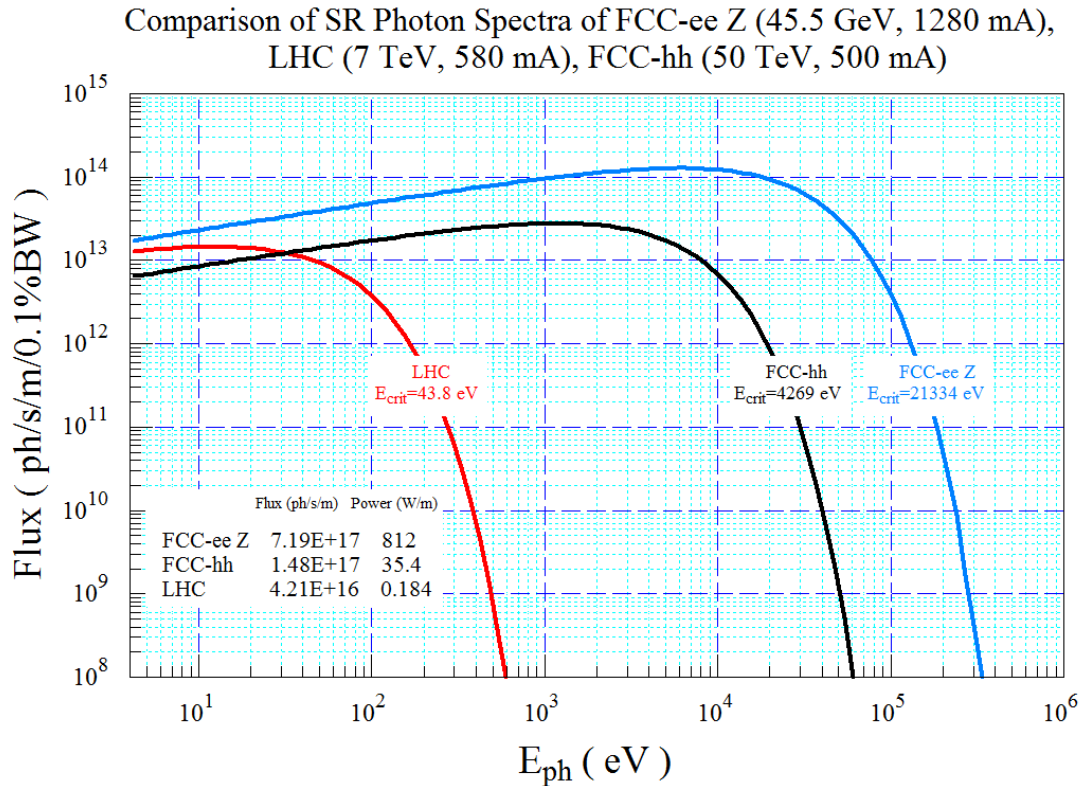


**Figure 2.3.:** Photon density of the synchrotron radiation as a function of the photon energy. This example presents the spectra of a dipole of the LHC and FCC obtained with Molflow [37, 38].

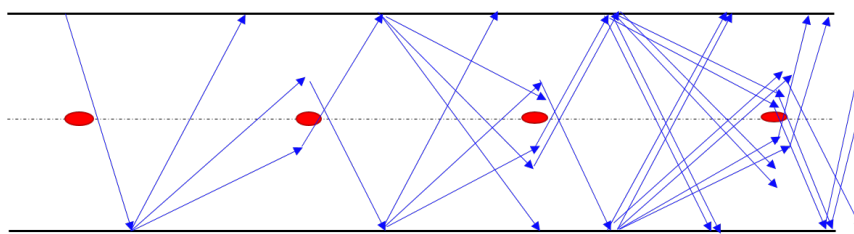


**Figure 2.4.:** Illustration of the electron cloud phenomenon (a similar plot can be found in [40]).

## 2. VACUUM SIMULATIONS IN HIGH ENERGY ACCELERATORS

crometric layer of Non-Evaporable-Getters (NEG) that traps the impinging residual gas particles, photons and electron and provide thus a distributed pumping and a reduction of the desorption [42–44]. Recently, there are several ongoing studies on further material treatment techniques aiming especially for the distributed pumping in the cryogenic areas (amorphous carbon coating, laser treatment "LESS"). So far, only the physisorption process is observed as a pumping in the cryogenic area. This means that particles stick on the wall due to the low temperatures, and drop off in one of the holes in the beam screen. The pumping through the holes is not depending on the lateral surface and is rather described with a linear distributed pumping (the LHC beam screen and a prototype of the FCC beam screen can be seen in Fig. 2.12).

**Locally concentrated pumping:** There exist many different vacuum pumps that are most efficient in different pressure ranges. Once ultra high vacuum is achieved, turbo-molecular pumps and ion-pumps are generally used to maintain its quality.

## 2.2. Mathematical model

Ficks's first and second laws of diffusion define the fundamental balance equation of the kinetics in a UHV system [21,45]. Considering additionally the flow in and out of the system, gives the following mass-balance equation for each species with the particle density  $\mathbf{n} = (n_{\text{H}_2}, n_{\text{CH}_4}, n_{\text{CO}}, n_{\text{CO}_2})$  as unknown:

$$\frac{\partial \mathbf{n}}{\partial t} = \mathbf{a} \circ \frac{\partial^2 \mathbf{n}}{\partial x^2} + \mathbf{r}(x, t) - \mathbf{s}(x, t), \quad (2.6)$$

wheras  $\mathbf{r} \in \mathbb{R}^4$  and  $\mathbf{s} \in \mathbb{R}^4$  describe the impact of sinks and sources and  $\mathbf{a} \in \mathbb{R}^4$  defines the specific conductance, given by

$$\begin{aligned} \mathbf{r}(x, t) &= \underbrace{\eta_{ph}(\Theta) \cdot \dot{\Gamma}_{ph}}_{\text{Desorption by photons}} + \underbrace{\eta_e(\Theta) \cdot \dot{N}_e}_{\text{by electrons}} + \boxed{\underbrace{\mathbf{H}_{ion}(\Theta) \cdot \dot{I}_{ion} \circ \mathbf{n}}_{\text{Ionization by beam and desorption by ions}}} + \underbrace{A \cdot \mathbf{q}_{th}}_{\text{thermal outgassing}} \\ &\quad \text{Multigasmodel} \\ \mathbf{s}(x, t) &= \underbrace{\alpha(\Theta) \circ \frac{A \cdot \bar{\mathbf{v}}}{4} \circ (\mathbf{n} - \chi_{\text{cryo}} \mathbf{n}_e)}_{\text{wall distributed pumping}} + \underbrace{\mathbf{p}_l \circ \mathbf{n}}_{\text{linear pumping}} \\ \mathbf{a}(x, t) &= \frac{d^3 \pi}{12} \cdot \bar{\mathbf{v}} \end{aligned}$$

The desorption ( $\eta$ ) and the sticking ( $\alpha$ ) coefficients strongly depend on the surface history ( $\Theta$ ) (dose, conditioning) and need to be considered for each domain of an accelerator separately. Further variables are defined in Table 2.9.

## 2.2. MATHEMATICAL MODEL

**Remark 2.1.** The symbol  $\circ$  indicates a component wise multiplication of two vectors, lower case bold symbols refer to vectors, upper-case bold letters to matrices and dotted variables to flux.

### 2.2.1. Assumptions

**Distinction in Segments** We divide the domain into a finite number of segments. Each segment is characterised by a constant set of parameters. Pumps and local gas sources can be set at the end or the beginning of each segment. Eq. (2.6) is solved for each segment and connected in a next step with intersection conditions to a global solution (see also Fig. 2.6).

**Model-reduction** Since most accelerators and components have one dimension which is much bigger than the others (length of the beam line vs. cross-section of the beam pipe), one-dimensional approximations in space produce good results. The characteristic parameters that are used for the calculations have to be transformed to values appropriate for a circular pipe-shape.

**Stationary flow** After a long pump-out process the vacuum system reaches an equilibrium status, so that the beam pipe vacuum varies rarely in time. We consider therefore time-invariant segment parameters. However this assumption is not true for all the parameters, e.g.:

- Induced gas desorption and photoelectron yields depend on the surface history (wall preconditioning, particle bombardment). For the cryogenic surfaces the parameters change with the amount of gas already condensed on the surface.
- NEG distributed pumping varies with the quantity of gas already pumped and the activation history.

With respect to these parameters the residual gas density estimation is relevant to a specific moment in time.

**Gas species** The dominant gas species, which are present in a vacuum system are hydrogen ( $H_2$ ), methane ( $CH_4$ ), carbon monoxide ( $CO$ ) and carbon dioxide ( $CO_2$ ) as seen in a mass spectrum of a UHV system, (see Fig. 2.5). Parameters are set according to the properties of these species. For example  $CH_4$  is a non-getterable gas, thus NEG pumping has no influence on its density.

**Maxwell-Boltzmann distribution for velocity of particles** The Maxwell-Boltzmann distribution describes particle velocities  $v$  for ideal gases, which have already reached thermodynamic equilibrium. The distribution function  $f(v)$  describes the probability that a particle has the velocity  $v$ . It depends on the temperature  $T$  of the system, the mass  $m$  of the particle and the Boltzmann constant  $k_B$ .  $v_p$  and  $\bar{v}$  describe the most probable velocity and the mean velocity respectively. For

## 2. VACUUM SIMULATIONS IN HIGH ENERGY ACCELERATORS

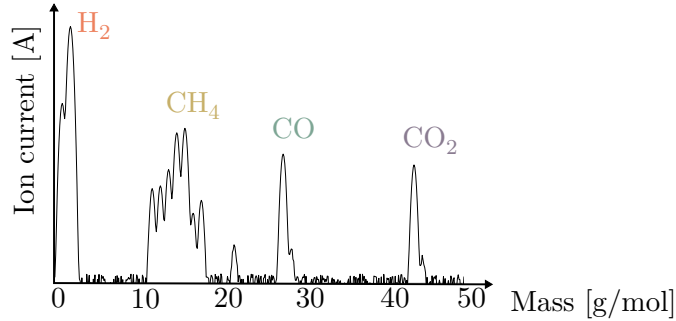


**Figure 2.5.:** Mass spectrum of a UHV system.

in the simulation we assume that all particles attain the mean velocity.

$$\begin{aligned} \text{probability distribution } f(v) &= 4\pi \left(\frac{m}{2\pi k_B T}\right)^{\frac{3}{2}} v^2 \exp\left(\frac{-mv^2}{2k_B T}\right) \\ \text{most probable velocity } v_p &= \sqrt{\frac{2k_B T}{m}} \\ \text{mean velocity } \bar{v} &= \frac{2}{\sqrt{\pi}} v_p \end{aligned}$$

For instance the mean velocity  $\bar{v}$  of the particles at room temperature 293 K ( $\approx 20^\circ\text{C}$ ) is the following:

$$(v_{\text{H}_2} \quad v_{\text{CH}_4} \quad v_{\text{CO}} \quad v_{\text{CO}_2}) = \left(1754.24 \quad 621.849 \quad 470.613 \quad 375.446\right) \frac{\text{m}}{\text{s}}$$

### 2.2.2. Schematic of the model

In the graphic of Fig. 2.6 a schematic of the domain is plotted. A detailed description of the variables is listed in Table 2.9.  $S$  are the pumps,  $x$  the spatial coordinates and  $n$  is the particle density. The index specifies the segment.

### 2.2.3. Single-gas model

The equation system (2.6) becomes decoupled, if the gas species do not interact with each other. This is the case, when the ion-induced desorption matrix  $\mathbf{H}_{ion}$  is diagonal or zero. Thus, we solve the equation system individually for each gas species, giving us the following 1-dimensional equation for the density  $n$  of one species:

$$0 = a \cdot n''(x) + b \cdot n(x) + c, \quad (2.7)$$

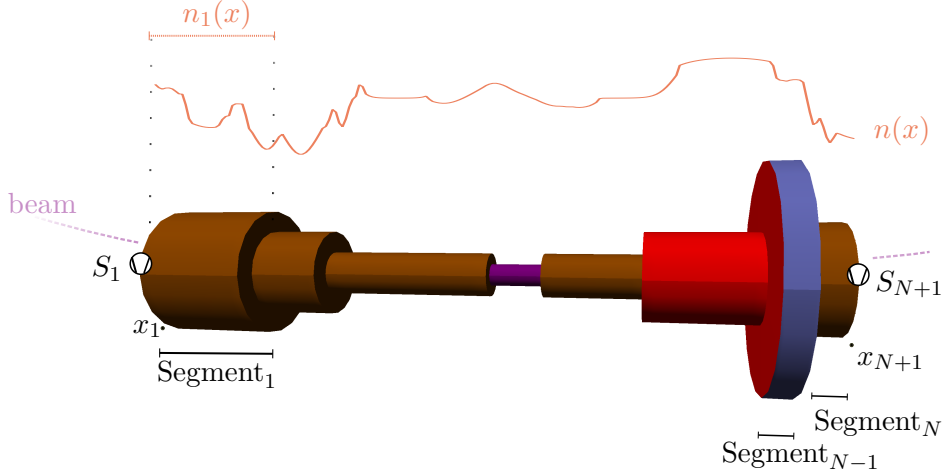


**Figure 2.6.:** Schematic of the PyVasco model.

where the coefficients  $a, b$  and  $c \in \mathbb{R}$  are expressed in terms of the physical properties of the medium, the diffusion rate, and the strength of the sinks and sources:

$$\begin{aligned} a &= c_{spec} \\ b &= -\eta_i(\Theta) \cdot \sigma \dot{I}_{ion} - \alpha(\Theta) \cdot \frac{\mathbf{A} \cdot \bar{\mathbf{v}}}{4} - p_l \\ c &= \eta_{ph}(\Theta) \cdot \dot{\Gamma}_{ph} + \eta_e(\Theta) \cdot \dot{N}_e + \chi_{cryo} \cdot \alpha(\Theta) \cdot \frac{\mathbf{A} \cdot \bar{\mathbf{v}}}{4} n_e + \mathbf{A} \cdot q_{th} \end{aligned}$$

**Solution for Eq. (2.6) for particle density** We find three solutions for  $n(x)$ , depending on the sign of the coefficient  $b$ , and considering that  $a$  is, from the context, always positive.  $C_1$  and  $C_2$  describe the integration constants, that are obtained later with the boundary conditions:

$$n(x) = \begin{cases} C_1 \cdot \exp\left(\sqrt{-\frac{b}{a}}x\right) + C_2 \cdot \exp\left(-\sqrt{-\frac{b}{a}}x\right) - \frac{c}{b} & \text{for } b < 0 \\ C_1 \cdot \cos\left(\sqrt{\frac{b}{a}}x\right) + C_2 \cdot \sin\left(\sqrt{\frac{b}{a}}x\right) - \frac{c}{b} & \text{for } b > 0 \\ C_1 + C_2 x - \frac{c}{2a} x^2 & \text{for } b = 0 \end{cases} \quad (2.8)$$

**Derivation of (2.8) for  $b < 0$**  The following approach is used:

$$n(x) = e^{\lambda x} \quad \lambda \in \mathbb{R}$$

## 2. VACUUM SIMULATIONS IN HIGH ENERGY ACCELERATORS

Plug in the approach of  $n(x)$  in the homogeneous differential equation of (2.7) , i.e.:  $c(x) = 0$  and normalize, so that the coefficient in front of the highest derivative is equal to one.

$$\begin{aligned} \lambda^2 e^{\lambda x} + \frac{b}{a} e^{\lambda x} &= 0 \\ (\lambda^2 + \frac{b}{a}) e^{\lambda x} &= 0 \\ \underbrace{(\lambda^2 + \frac{b}{a})}_{p(\lambda)} &= 0 \end{aligned}$$

This implies that we need to find a root of the characteristic polynomial  $p(\lambda)$ :

$$\lambda_{1,2} = \pm \sqrt{-\frac{b}{a}}$$

Given that  $-\frac{b}{a} > 0$ , we get two real solution for (2.7)

$$x \mapsto e^{\lambda_1 x}, \quad x \mapsto e^{\lambda_2 x}$$

Therefore we obtain the following homogeneous solution of (2.7) with arbitrary constants  $C_1$  and  $C_2$ .

$$n(x) = C_1 e^{\lambda_1 x} + C_2 e^{\lambda_2 x}$$

The inhomogeneous solution, i.e.  $c(x) \neq 0$ , can be found by adding a particular solution of (2.8) to the homogeneous one. The following approach is used:  $n_p(x) = c_0$  considering the form of  $c(x)$ . Plugging in  $n_p$  in (2.7):

$$\frac{b}{a} c_0 = -\frac{c}{a}$$

Therefore

$$c_0 = -\frac{c}{b}$$

And we obtain  $n(x)$  as in (2.8) for  $b < 0$ .

**Boundary and intersection conditions** For the **first and last segment**  $k = 1$  and  $k = N$  Robin boundary conditions describe the flux continuity acting only on half of the pumping speed and half

## 2.2. MATHEMATICAL MODEL

of the gas release. The other half is assumed to be taken by the neighbouring unknown segment.

$$a_1 n'_1(x_1) = \frac{S_1}{2} n_1(x_1) - \frac{g_1}{2} \quad (2.9)$$

$$-a_N n'_N(x_{N+1}) = \frac{S_{N+1}}{2} n_N(x_{N+1}) - \frac{g_{N+1}}{2} \quad (2.10)$$

Notice the change of sign in front of the term involving the derivative. That is because the normal points in the positive direction at the beginning of the segments, while at the end it points in the negative direction.

At the intersection points of two segments the continuity of the density function is imposed and the sum of the flux of molecules must equal the amount of molecules pumped or generated by a local source:

For the **intermediate segments**  $k = 2, \dots, N$  Dirichlet and Robin conditions are defined:

$$n_{k-1}(x_k) = n_k(x_k) \quad (2.11)$$

$$-a_{k-1} n'_{k-1}(x_k) + a_k n'_k(x_k) = S_k n_k(x_k) - g_k \quad (2.12)$$

Boundary and intersection conditions (2.9) - (2.12) for all segments  $k = 1, \dots, N$  can be summarized in the following sparse equation system with band structure, considering the Sol. (2.8) :

$$\underbrace{\begin{pmatrix} * & * & 0 & 0 & 0 & 0 & 0 & 0 & 0 & 0 \\ * & * & * & 0 & 0 & 0 & 0 & 0 & 0 & 0 \\ * & * & * & 0 & 0 & 0 & 0 & 0 & 0 & 0 \\ 0 & 0 & * & * & * & 0 & 0 & 0 & 0 & 0 \\ 0 & 0 & * & * & * & 0 & 0 & 0 & 0 & 0 \\ 0 & 0 & 0 & 0 & * & * & * & 0 & 0 & 0 \\ 0 & 0 & 0 & 0 & * & * & * & * & 0 & 0 \\ & & & & & \ddots & & & & \\ 0 & 0 & 0 & 0 & 0 & 0 & * & * & * & * \\ 0 & 0 & 0 & 0 & 0 & 0 & * & * & * & * \\ 0 & 0 & 0 & 0 & 0 & 0 & 0 & 0 & * & * \end{pmatrix}}_{\text{SM}} \cdot \begin{pmatrix} C_1 \\ C_2 \\ \vdots \\ C_{2N\text{Seg}} \end{pmatrix} = \underbrace{\begin{pmatrix} * \\ * \\ * \\ * \\ \vdots \\ * \\ * \\ * \\ * \end{pmatrix}}_w,$$

where:  $\text{SM} \in \mathbb{R}^{2N \times 2N}$ ,  $c \in \mathbb{R}^{2N}$ ,  $w \in \mathbb{R}^{2N}$

**Values for SM and w** For a better representation we save the terms in front of the coefficients  $C_1$  and  $C_2$  of Solution (2.8) in the variables  $\alpha, \beta$  and  $\gamma \in \mathbb{R}$  summarized in Table 2.2.

## 2. VACUUM SIMULATIONS IN HIGH ENERGY ACCELERATORS

**Table 2.2.:** Model parameters for physical description.

$\alpha(x) = \begin{cases} \exp(\sqrt{-\frac{b}{a}}x) & b < 0 \\ \cos(\sqrt{\frac{b}{a}}x) & b > 0 \\ 1 & b = 0 \end{cases}$	$\alpha'(x) = \begin{cases} \sqrt{-\frac{b}{a}} \exp(\sqrt{-\frac{b}{a}}x) & b < 0 \\ -\sqrt{\frac{b}{a}} \sin(\sqrt{\frac{b}{a}}x) & b > 0 \\ 0 & b = 0 \end{cases}$
$\beta(x) = \begin{cases} \exp(-\sqrt{-\frac{b}{a}}x) & b < 0 \\ \sin(\sqrt{\frac{b}{a}}x) & b > 0 \\ x & b = 0 \end{cases}$	$\beta'(x) = \begin{cases} -\sqrt{-\frac{b}{a}} \exp(-\sqrt{-\frac{b}{a}}x) & b < 0 \\ \sqrt{\frac{b}{a}} \cos(\sqrt{\frac{b}{a}}x) & b > 0 \\ 1 & b = 0 \end{cases}$
$\gamma(x) = \begin{cases} -\frac{c}{b} & b \neq 0 \\ -\frac{c}{2a}x^2 & b = 0 \end{cases}$	$\gamma'(x) = \begin{cases} 0 & b \neq 0 \\ -\frac{c}{a}x & b = 0 \end{cases}$

The matrix  $SM$  and the right-hand side  $w$  are assembled in the following way:

$$SM =$$

$$\left( \begin{array}{ccccccccc} BC & \left\{ \begin{array}{ccccccccc} \alpha \frac{S_1}{2} - a\alpha' & \frac{S_1}{2}\beta - a\beta' & 0 & & & & \dots & & 0 \\ \alpha & \beta & -\alpha & -\beta & 0 & & \dots & & 0 \\ -a\alpha' & -a\beta' & a\alpha' - S_2\alpha & a\beta' - S_2\beta & 0 & & \dots & & 0 \\ \vdots & & & & & \ddots & & & \\ IC & \left\{ \begin{array}{ccccccccc} 0 & \dots & 0 & \alpha & \beta & -\alpha & -\beta \\ 0 & \dots & 0 & -a\alpha' & -a\beta' & a\alpha' - S\alpha & a\beta' - S\beta \\ 0 & \dots & 0 & 0 & 0 & \alpha \frac{S_{N+1}}{2} + a\alpha' & \frac{S_{N+1}}{2}\beta + a\beta' \end{array} \right. \end{array} \right)$$

**Remark 2.2.** For readability reasons the segment-indices of the parameters  $a, \alpha, \dots$  were not included in the matrix  $SM$ . However, two columns always describe the properties of one segment, i.e. in the first and second column the parameter values of segment one are used. Pumps are always located at the beginning of each segment, i.e.  $S_1$  is located at the beginning of segment one.

$$w = \begin{pmatrix} -\frac{S_1}{2}\gamma_1 + g + a\gamma'_1 \\ -\gamma_1 + \gamma_2 \\ a_1\gamma'_1 - a_2\gamma'_2 + S\gamma - g_1 \\ \vdots \\ -\gamma_{N-1} + \gamma_N \\ a_{N-1}\gamma'_{N-1} - a_N\gamma'_N + S_N\gamma_N - g_N \\ -\frac{S_{N+1}}{2}\gamma_{N+1} + g - a\gamma'_{N+1} \end{pmatrix} \left. \begin{array}{l} \{\text{BC} \\ \{\text{IC} \\ \vdots \\ \{\text{IC} \\ \{\text{BC} \end{array} \right.$$

The solution of this linear equation system is obtained by using a Gauss-Jordan elimination algorithm (further iterative solvers are described here: [46, 47]). The exactitude of the implemented algorithm for small domains ( $N < 5$ ) was cross-checked with the command "Solve" in Mathematica. By default Mathematica uses inverse functions to calculate a solution.

The solution  $n$  describes the only satisfying values for the constants  $C_1, C_2$  (see Sol. (2.8)) that fulfills also the boundary conditions.

In the end it only remains to combine the local solutions  $n_k$  of each segment to a global solution  $n$ :

$$n(x) = \begin{cases} n_1(x) & x_1 \leq x \leq x_2 \\ n_2(x) & x_2 < x \leq x_3 \\ \vdots \\ n_N(x) & x_N < x \leq x_{N+1} \end{cases}$$

#### 2.2.4. Multi-gas model

The previous model is extended and interactions between the different gas species are also taken into account. More precisely this interaction occurs in the ion-induced desorption term. An incident ion can desorb gas of any species and thus  $\mathbf{H}_{ion}$  presents a fully occupied matrix. E.g., the column  $j$  of  $\mathbf{H}_{ion}$  describes the probability of the desorption rate when a particle of gas species  $j$  impinges on the wall.

$$\mathbf{H}_{ion} \in \mathbb{R}^{4 \times 4} = \begin{pmatrix} \eta_{H_2^+ \rightarrow H_2} & \eta_{CH_4^+ \rightarrow H_2} & \eta_{CO^+ \rightarrow H_2} & \eta_{CO_2^+ \rightarrow H_2} \\ \eta_{H_2^+ \rightarrow CH_4} & \eta_{CH_4^+ \rightarrow CH_4} & \eta_{CO^+ \rightarrow CH_4} & \eta_{CO_2^+ \rightarrow CH_4} \\ \eta_{H_2^+ \rightarrow CO} & \eta_{CH_4^+ \rightarrow CO} & \eta_{CO^+ \rightarrow CO} & \eta_{CO_2^+ \rightarrow CO} \\ \eta_{H_2^+ \rightarrow CO_2} & \eta_{CH_4^+ \rightarrow CO_2} & \eta_{CO^+ \rightarrow CO_2} & \eta_{CO_2^+ \rightarrow CO_2} \end{pmatrix}$$

## 2. VACUUM SIMULATIONS IN HIGH ENERGY ACCELERATORS

The balance equation (2.6) including interaction among the gas species can be written as follows:

$$\vec{0}_4 = \mathbf{A}(x) \frac{d\mathbf{n}^2}{dx^2} + \mathbf{B}(x)\mathbf{n} + \mathbf{c}(x) \quad (2.13)$$

with  $\mathbf{A}, \mathbf{B} \in \mathbb{R}^{4 \times 4}$  and  $\mathbf{c} \in \mathbb{R}^4$  being the matrix and vector assemblies of the parameters (4-dimensional analogy to  $a, b, c$  of the single gas problem) :

$$\begin{aligned} \mathbf{A} &= \mathbf{a} \cdot \mathbf{I}_4 \\ \mathbf{B} &= \mathbf{H}_{ion} \cdot \dot{I}_{ion} - \alpha \circ \frac{\mathbf{A} \cdot \bar{\mathbf{v}}}{4} - \mathbf{p}_l \\ \mathbf{c} &= -\chi_{cryo} \cdot \alpha \circ \frac{\mathbf{A} \cdot \bar{\mathbf{v}}}{4} \circ n_e + \eta_{ph} \cdot \dot{\Gamma}_{ph} + \eta_e \cdot \dot{N}_e + A \cdot \mathbf{q}_{th} \end{aligned}$$

**Remark 2.3.** Note, that all variables mentioned in this section are listed in detail in Table 2.10. The major challenge in solving this system lies therefore in the fully occupied matrix  $\mathbf{B}$ .

Two key ideas to solve the equation system:

1. The beam pipe usually provides constant coefficients over a specific domain. The domain is therefore split into a finite number of elements and the solution is computed on each element (as it was done for the single-gas model). The local solution functions are combined then with boundary conditions to a global solution. The following boundary conditions describe density and flux continuity:

Boundary and intersection conditions for segment  $k - 1$  and  $k$ :

$$\mathbf{n}_{k-1}(x_k) = \mathbf{n}_k(x_k) \quad (2.14)$$

$$-\mathbf{a}_{k-1} \circ \mathbf{n}'_{k-1}(x_k) + \mathbf{a}_k \circ \mathbf{n}'_k(x_k) = \mathbf{s}_k \circ \mathbf{n}_k(x_k) - \mathbf{g}_k \quad (2.15)$$

$$\mathbf{a}_1 \circ \mathbf{n}'_1(x_1) = \frac{\mathbf{s}_1}{2} \circ \mathbf{n}_1(x_1) - \frac{\mathbf{g}_1}{2} \quad (2.16)$$

$$-\mathbf{a}_N \circ \mathbf{n}'_N(x_{N+1}) = \frac{\mathbf{s}_{N+1}}{2} \circ \mathbf{n}_N(x_{N+1}) - \frac{\mathbf{g}_{N+1}}{2} \quad (2.17)$$

2. Transform the equation system to an equation system of first order, by using the transformation identity  $\mathbf{y} = \begin{pmatrix} \mathbf{n} \\ \mathbf{n}' \end{pmatrix}$  obtaining the following equilibrium equation (see also further description in [48–51]):

$$\frac{d\mathbf{y}}{dx}(x) = \mathbf{M}\mathbf{y}(x) + \mathbf{b} \quad (2.18)$$

## 2.2. MATHEMATICAL MODEL

with the corresponding modified boundary conditions:

$$\mathbf{H}_{k-1}\mathbf{y}_{k-1}(L) - (\mathbf{H}_k + \mathbf{S}_k)\mathbf{y}_k(0) = \bar{\mathbf{g}}_k \quad (2.19)$$

$$\mathbf{F}_1\mathbf{y}_1(0) = -\mathbf{g}_1 \quad (2.20)$$

$$\mathbf{F}_N\mathbf{y}_N(x_{N+1}) = \mathbf{g}_{N+1}, \quad (2.21)$$

where:

$$\begin{aligned} \mathbf{M} &:= \begin{pmatrix} \mathbf{0}_{4 \times 4} & \mathbf{I}_4 \\ -\mathbf{A}^{-1}\mathbf{B} & \mathbf{0}_{4 \times 4} \end{pmatrix}, \mathbf{b} := \begin{pmatrix} \mathbf{0}_{4 \times 4} \\ -\mathbf{A}^{-1}\mathbf{c} \end{pmatrix} \\ \mathbf{F}_1 &:= \left( -\frac{\mathbf{s}_1\mathbf{I}_4}{2} \quad \mathbf{A} \right), \quad \mathbf{F}_N := \left( -\frac{\mathbf{s}_{N+1}\mathbf{I}_4}{2} \quad -\mathbf{A} \right) \\ \mathbf{H}_k &:= \begin{pmatrix} \mathbf{I}_4 & \mathbf{0}_{4 \times 4} \\ \mathbf{0}_{4 \times 4} & -\mathbf{A}_k \end{pmatrix}, \quad \mathbf{S}_k := \begin{pmatrix} \mathbf{0}_{4 \times 4} & \mathbf{0}_{4 \times 4} \\ \mathbf{s}_k\mathbf{I}_4 & \mathbf{0}_{4 \times 4} \end{pmatrix} \text{ and } \bar{\mathbf{g}}_k := \begin{pmatrix} \vec{0}_4 \\ -\mathbf{g}_k \end{pmatrix} \end{aligned}$$

The fundamental Theorem of Picard Lindelöf gives a solution for each segment as of the form:

$$\boxed{\mathbf{y}(x) = \underbrace{e^{(x-x_k)\mathbf{M}}}_{\text{fundamental solution } \mathbf{P}(x)} \mathbf{u} + \underbrace{\int_{x_k}^x e^{(x-\tilde{x})\mathbf{M}} \mathbf{b} d\tilde{x}}_{\text{particular solution } \mathbf{z}(x)} .} \quad (2.22)$$

for  $x_k \leq x < x_{k+1}$ .  $\mathbf{M}$  and  $\mathbf{b}$  are determined by material, beam and geometry specifications and  $\mathbf{u}$  defines the integration constant, verified below with the boundary conditions.

The matrix  $\mathbf{SM} \in \mathbb{R}^{(2 \cdot N_{\text{gas}} \cdot N_{\text{segments}}) \times (2 \cdot N_{\text{gas}} \cdot N_{\text{segments}})}$  and a right-hand side  $\mathbf{w} \in \mathbb{R}^{(2 \cdot N_{\text{gas}} \cdot N_{\text{segments}})}$  compress all information of the boundary conditions in a system of  $(2 \cdot N_{\text{gas}} \cdot N_{\text{segments}})$ -equations (note: different structure to the paper [1], but describes the same algorithm, see also Fig. 2.7)

$$\underbrace{\begin{pmatrix} \mathbf{F}_1 & 0 & 0 & 0 & 0 \\ \mathbf{H}_1\mathbf{P}_1 & -\mathbf{S}_2 & 0 & 0 & 0 \\ 0 & \mathbf{H}_2\mathbf{P}_2 & -\mathbf{S}_3 & 0 & 0 \\ & & & \ddots & \\ 0 & 0 & 0 & \mathbf{H}_{N-1}\mathbf{P}_{N-1} & -\mathbf{S}_N \\ 0 & 0 & 0 & 0 & \mathbf{F}_N\mathbf{P}_N \end{pmatrix}}_{=: \mathbf{SM}} \begin{pmatrix} \mathbf{u}_1 \\ \mathbf{u}_2 \\ \vdots \\ \mathbf{u}_N \end{pmatrix} = \underbrace{\begin{pmatrix} -\mathbf{g}_1 \\ \bar{\mathbf{g}}_2 - \mathbf{H}_1\mathbf{z}_1 \\ \bar{\mathbf{g}}_3 - \mathbf{H}_2\mathbf{z}_2 \\ \vdots \\ \bar{\mathbf{g}}_N - \mathbf{H}_{N-1}\mathbf{z}_{N-1} \\ \mathbf{g}_{N+1} - \mathbf{F}_N\mathbf{z}_N \end{pmatrix}}_{=: \mathbf{w}} \quad (2.23)$$

This equation system is solved with the solution method of the "Gauss-Jordan"-algorithm. We take the sparse-occupied property of the matrix  $\mathbf{SM}$  into account, this allows us to save storage space and speed up the computation time (further described in Section 2.3).

## 2. VACUUM SIMULATIONS IN HIGH ENERGY ACCELERATORS

The global solution  $\mathbf{n}$  is obtained as a piecewise function of the local solutions  $\mathbf{n}_k$  for each segment, which we get with a backward transformation of  $\mathbf{y}$  and the substitution of  $\mathbf{u}$  from Eq. (2.23) into Sol. (2.22):

$$\mathbf{n}_k(x) = [y_k(x)]_{1:4} = \mathbf{P}_k(x)\mathbf{u}_k + \mathbf{z}_k(x)$$

and

$$\mathbf{n}(x) = \begin{cases} \mathbf{n}_1(x) & x_1 \leq x \leq x_2 \\ \mathbf{n}_2(x) & x_2 < x \leq x_3 \\ \vdots \\ \mathbf{n}_N(x) & x_N < x \leq x_{N+1} \end{cases}$$

### 2.2.5. Appendix to Multi-gas model

**Solving the integral from  $\mathbf{z}(x)$  :**

$$\begin{aligned} \mathbf{z}(x) &= \int_{x_k}^x e^{(x-t)\mathbf{M}} \mathbf{b} dt = -\mathbf{M}^{-1} e^{(x-t)\mathbf{M}} \mathbf{b} \Big|_{x_k}^x = \\ &= -\mathbf{M}^{-1} \underbrace{e^{0\cdot\mathbf{M}}}_{=\mathbf{I}} \mathbf{b} + \mathbf{M}^{-1} \underbrace{e^{(x-x_k)\mathbf{M}}}_{\mathbf{P}(x)} \mathbf{b} = (-\mathbf{I} + \mathbf{P}(x)) \mathbf{M}^{-1} \mathbf{b} \\ &= (\mathbf{P}(x) - \mathbf{I}) \mathbf{M}^{-1} \mathbf{b} \end{aligned}$$

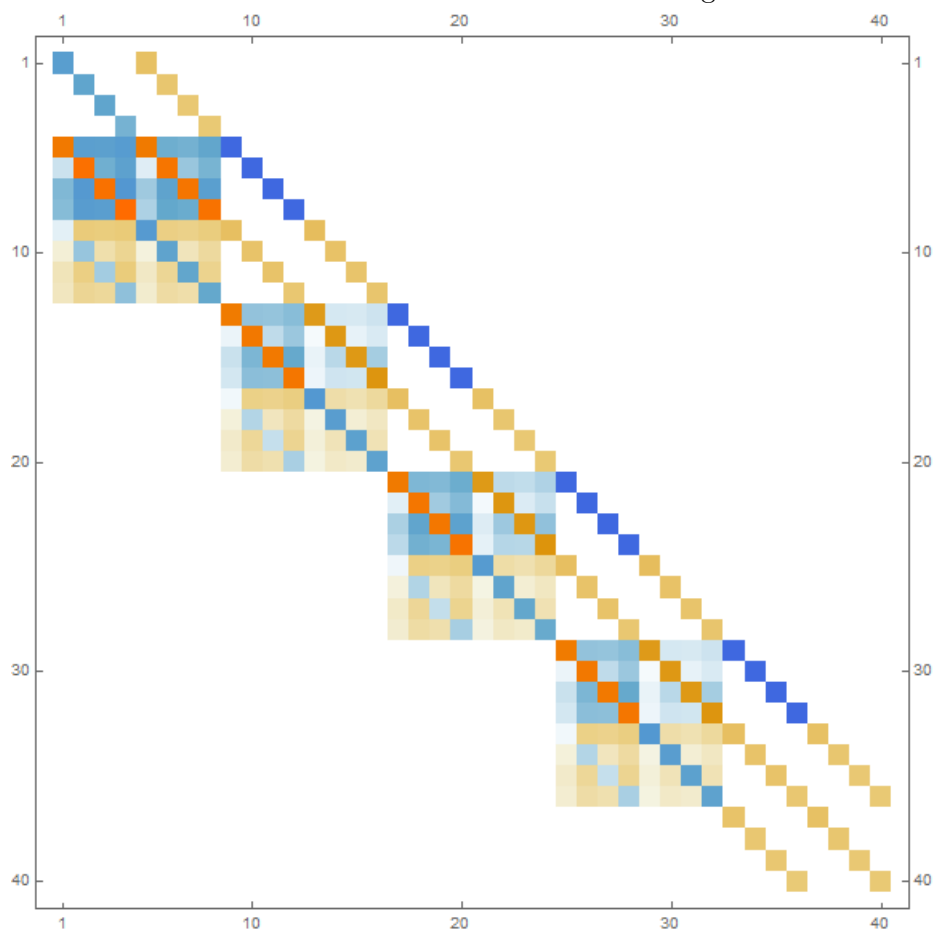
**Verify solution (2.22) of eq. (2.18) by differentiation**

$$\begin{aligned} \mathbf{y}(x) &= \mathbf{P}(x)\mathbf{u} + \mathbf{z}(x) \mathbf{b} dt = \text{ (Plug in definition of } \mathbf{P}(x) \text{ and } \mathbf{z}(x)) \\ &= e^{(x-x_k)\mathbf{M}} \mathbf{u} + (e^{(x-x_k)\mathbf{M}} - \mathbf{I}_8) \mathbf{M}^{-1} \mathbf{b} \\ &= e^{(x-x_k)\mathbf{M}} (\mathbf{u} + \mathbf{M}^{-1} \mathbf{b}) - \mathbf{M}^{-1} \mathbf{b} \end{aligned}$$

$$\mathbf{y}'(x) = \mathbf{M} e^{(x-x_k)\mathbf{M}} (\mathbf{u} + \mathbf{M}^{-1} \mathbf{b})$$

## 2.2. MATHEMATICAL MODEL

**Figure 2.7.:** Representation of the sparse matrix  $\mathbf{SM} \in \mathbb{R}^{40 \times 40}$  in the case that the domain is split into 5 segments; 320 of the 1600 entries are occupied. Note, that the simulation of the FCC consists of more than 600 segments.



## 2. VACUUM SIMULATIONS IN HIGH ENERGY ACCELERATORS

( Plug in  $\mathbf{y}(x)$  and  $\mathbf{y}'(x)$  in Eq.(2.18) ):

$$\begin{aligned}\mathbf{y}'(x) &= \mathbf{M}\mathbf{y}(x) + \mathbf{b} \\ \mathbf{M} e^{(x-x_k) \mathbf{M}} (\mathbf{u} + \mathbf{M}^{-1}\mathbf{b}) &= \mathbf{M} \cdot [e^{(x-x_k) \mathbf{M}} (\mathbf{u} + \mathbf{M}^{-1}\mathbf{b}) - \mathbf{M}^{-1}\mathbf{b}] + b \\ &= \mathbf{M} e^{(x-x_k) \mathbf{M}} (\mathbf{u} + \mathbf{M}^{-1}\mathbf{b}) - \underbrace{\mathbf{M}\mathbf{M}^{-1}}_{\mathbf{I}} \mathbf{b} + \mathbf{b}\end{aligned}$$

### Structure of the matrix exponential of $\mathbf{P}(x)$

**Definition 2.4** (Matrix exponential). *For a  $(n \times n)$  matrix  $\mathbf{A}$  is the matrix exponential given by :*

$$e^{\mathbf{A}} := \sum_{k=0}^{\infty} \frac{\mathbf{A}^k}{k!}, \quad (2.24)$$

where the matrix products of the first elements are defined as:  $\mathbf{A}^0 = \mathbf{I}_n, \mathbf{A}^1 = \mathbf{A}, \mathbf{A}^{k+1} = \mathbf{A}^k \mathbf{A}$

$$\mathbf{P}(x) = e^{x \cdot \mathbf{M}}, \quad \text{where we defined: } \mathbf{M} = \begin{pmatrix} \mathbf{0}_{4 \times 4} & \mathbf{I}_4 \\ \underbrace{-\mathbf{A}^{-1}\mathbf{B}}_{\mathbf{M}} & \mathbf{0}_{4 \times 4} \end{pmatrix}$$

Since the matrix-exponential is defined as the sum of its matrix products, it is important to know the structure of  $\mathbf{M}^n$ , where  $\mathbf{M} \in \mathbb{R}^{NGas \times NGas} = -\mathbf{A}^{-1}\mathbf{B}$  describes the submatrix of the left lower corner of  $\mathbf{M}$ .

$$\begin{aligned}\mathbf{M}^0 &= \frac{1}{0!} \begin{pmatrix} I & 0 \\ 0 & I \end{pmatrix} & \mathbf{M}^1 &= \frac{1}{1!} \begin{pmatrix} 0 & I \\ \mathbb{M} & 0 \end{pmatrix} & \mathbf{M}^2 &= \frac{1}{2!} \begin{pmatrix} \mathbb{M} & 0 \\ 0 & \mathbb{M} \end{pmatrix} & \mathbf{M}^3 &= \frac{1}{3!} \begin{pmatrix} 0 & \mathbb{M} \\ \mathbb{M}^2 & 0 \end{pmatrix} \\ \mathbf{M}^4 &= \frac{1}{4!} \begin{pmatrix} \mathbb{M}^2 & 0 \\ 0 & \mathbb{M}^2 \end{pmatrix} & \mathbf{M}^5 &= \frac{1}{5!} \begin{pmatrix} 0 & \mathbb{M}^2 \\ \mathbb{M}^3 & 0 \end{pmatrix} & \mathbf{M}^6 &= \frac{1}{6!} \begin{pmatrix} \mathbb{M}^3 & 0 \\ 0 & \mathbb{M}^3 \end{pmatrix}\end{aligned}$$

This development leads to the following general form for  $\mathbf{P}(x)$  (can be shown by induction):

$$\begin{aligned}\mathbf{P}(x) &= \\ &= \sum_{n=0}^{\infty} \begin{pmatrix} (x_{i+1} - t)^{2n+1} \mathbb{I}_{(4 \times 4)} & 0_{(4 \times 4)} \\ 0_{(4 \times 4)} & (x_{i+1} - t)^{2n} \mathbb{I}_{(4 \times 4)} \end{pmatrix} \begin{pmatrix} \frac{\mathbb{M}^n}{(2n)!} & \frac{\mathbb{M}^n}{(2n+1)!} \\ \frac{\mathbb{M}^{n+1}}{(2n+1)!} & \frac{\mathbb{M}^n}{(2n)!} \end{pmatrix} = \\ &= \begin{pmatrix} \frac{x e^{\sqrt{\mathbb{M}}x} + e^{-\sqrt{\mathbb{M}}x}}{2} & \frac{1}{\sqrt{\mathbb{M}}} \frac{e^{\sqrt{\mathbb{M}}x} - e^{-\sqrt{\mathbb{M}}x}}{2} \\ \frac{\sqrt{\mathbb{M}} e^{\sqrt{\mathbb{M}}x} - e^{-\sqrt{\mathbb{M}}x}}{x} & \frac{e^{\sqrt{\mathbb{M}}x} + e^{-\sqrt{\mathbb{M}}x}}{2} \end{pmatrix}\end{aligned}$$

$\mathbf{P}(x)$  is implemented in the form of the above expression in the programming code PyVasco.

### Base items and unit crosscheck of PyVasco

The equations of the analytical model have to be consistent with their units, and this is carefully checked in the following.  $i$  corresponds to the different gas species H<sub>2</sub>, CH<sub>4</sub>, CO and CO<sub>2</sub>.

#### Equilibrium Equation

$$\underbrace{\frac{m^4}{s}}_A \cdot \underbrace{\frac{1}{m^3}}_{n''} + \underbrace{\frac{m^2}{s}}_B \cdot \underbrace{\frac{1}{m^3}}_n + \underbrace{\frac{1}{m \cdot s}}_c = \underbrace{\frac{1}{m \cdot s}}_{V \cdot \dot{n}}$$

**Matrix A**  $A$  is a diagonal matrix with the specific conductance as entries:

$$a_{ii} = \frac{d^3}{3} \sqrt{\frac{\pi R_0 T}{2M_m}}$$

$$\frac{m^4}{s} = m^3 \cdot \sqrt{\frac{\frac{J}{K \cdot mol} \cdot K}{\frac{kg}{mol}}} = m^3 \cdot \sqrt{\frac{J}{kg}} = m^3 \cdot \frac{m}{s}$$

#### Matrix B

$$b_{ii} = (\eta_i + \eta'_i(\Theta) - 1) \cdot \sigma_{i-I} \frac{I}{e} - S_{wall}(\Theta) - S_{cryo} \quad (2.25)$$

$$\frac{m^2}{s} = \frac{A}{C} \cdot m^2 - m \cdot \frac{m}{s} - \frac{m^2}{s} = \frac{A}{A \cdot s} \cdot m^2 - \frac{m^2}{s} - \frac{m^2}{s} \quad (2.26)$$

#### Vector C

$$c_i = -S_{cryo} n_e(\Theta, T) + (\eta_{ph} + \eta'_{ph}(\Theta)) \dot{\Gamma}_{ph} + (\eta_e + \eta'_e(\Theta)) \dot{N}_e + a \cdot q$$

$$\frac{1}{m \cdot s} = m \cdot \frac{m}{s} \frac{1}{m^3} + \frac{1}{m \cdot s} + \frac{1}{m \cdot s} + m \cdot \frac{1}{m^2 \cdot s}$$

#### Thermal Desorption $q_{th}$

$$q_{th,i} = \frac{\text{Number of Particles}}{\text{Area} \cdot \text{Time}} = \underbrace{\frac{\text{Pressure} \cdot \text{Volume}}{k_B \cdot \text{Temperature}}}_{\text{Ideal Gas Law}} \cdot \frac{1}{\text{Area} \cdot \text{Time}}$$

$$\frac{\text{molecules}}{m^2 \cdot s} = \frac{Pa \cdot m^3}{k_B \cdot T} \cdot \frac{1}{m^2 \cdot s} = \frac{\frac{kg}{m \cdot s^2} \cdot m^3}{\frac{m^2 \cdot kg}{s^2 \cdot K} \cdot K} \cdot \frac{1}{m^2 \cdot s}$$

$$= \frac{10^3}{k_B \cdot K} \cdot \underbrace{\frac{\text{mbar} \cdot l}{cm^2 \cdot s}}_{\text{User-Input in PyVasco}}$$

## 2. VACUUM SIMULATIONS IN HIGH ENERGY ACCELERATORS

$$\underbrace{\frac{\text{Number of Particles}}{\text{Area} \cdot \text{Time}}}_{\text{Input } Simulation-Code} = \underbrace{\frac{\text{Pressure} \cdot \text{Volume}}{\text{Area} \cdot \text{Time}}}_{[\frac{\text{mbar} \cdot \text{l}}{\text{s} \cdot \text{cm}^2}], \text{User-Input PyVasco}} \cdot \underbrace{\frac{100}{\text{mbar} \rightarrow \text{Pa}} \cdot \frac{10^{-3}}{\text{l} \rightarrow \text{m}^3}}_{\text{Unit Conversion}} \cdot \underbrace{\frac{1}{\frac{10^{-4}}{\text{cm}^2 \rightarrow \frac{1}{\text{m}^2}}} \cdot \frac{1}{\frac{1}{k_B \cdot T}}}_{\text{Unit Conversion}}$$

**Localized Gas Source  $g$**

$$g_i = \frac{\text{Number of Particles}}{\text{Time}} = \frac{\text{Pressure} \cdot \text{Volume}}{\underbrace{k_B \cdot \text{Temperature}}_{\text{Ideal Gas Law}}} \cdot \frac{1}{\text{Time}}$$

$$\frac{1}{\text{s}} \stackrel{\text{similar to q}}{=} \frac{10^3}{k_B \cdot K} \cdot \underbrace{\frac{\text{mbar} \cdot \text{l}}{\text{s}}}_{\text{User-Input PyVasco}}$$

### 2.3. Computer implementation

PyVasco is a 1D code that calculates vacuum profiles in a particle accelerator based on analytical methods following the concept of Section 2.2. Its acronym stands for "VAcuum Stability COde implemented in Python" and is supported by a graphical user interface embedded in PyQt [52–55]. The evolution of the project is managed with the CERN internal version control software Git. Functions are occasionally tested with unit-testing.

**Handling of input data** Several effects, summarized in 54 input variables per segment, influence the vacuum model. However, a strong correlation among them can be observed. For instance the choice of the material defines the desorption yield of synchrotron radiation, electron cloud and ion induced desorption, as well as the thermal outgassing properties. It stands therefore to reason to implement a Python class "material". Following the same idea, we summarized the pumping speed and the gas release in a python class "Pump" and "Gas-source", respectively. The main program uses csv-files as input to set all configuration variables for the simulations. This allows the user to organize the input values and use them for several simulations. A sample of the configuration variables can be seen in Table 2.3-2.6.

**Implementation of the solving algorithm** An efficient implementation of the data structure is crucial for the codes' performance since the matrix dimensions grow rather fast. For the simulation of the FCC we had in total 676 segments, which yield a  $5408 \times 5408$  matrix. The concept of a sparse matrix implementation was therefore considered and instead of saving a  $8 \cdot N_{gas} \cdot N_{Seg} \times 8 \cdot N_{gas} \cdot N_{Seg}$  matrix, we stored the information in a  $8 \cdot N_{gas} \cdot N_{Seg} \times 17$  array. The memory storage was therefore reduced from  $\mathcal{O}(N^2)$  to  $\mathcal{O}(N)$ . Considering that  $N$  can reach large values ( $> 1000$ ), this step is of high importance (see also Fig. 2.8).

### 2.3. COMPUTER IMPLEMENTATION

**Table 2.3.:** Template for the input file of the simulation domain. The placeholder % indicates the user's input; an equivalent diameter indicates a cylindrical chamber having the same conductance; a material shortcut means e.g. NEG -NEG Coating, CM - ColdMass, Cu - baked copper.

Segment id/name	Segment 1	Segment 2	description
d [mm]	%	%	equivalent diameter
L [mm]	%	%	length
T [K]	%	%	temperature
Material	%	%	material shortcut (from material folder)
Pump	%	%	Pump shortcut (from Pumps folder)
Gassource	%	%	Gassource shortcut (from gas-sources folder)
Photon flux [photons/s]	%	%	Number of photons impinging the wall
Electron flux [electrons/s]	%	%	Number of electrons impinging the wall

**Table 2.4.:** Template for the input file for one pump. The place holder % indicates the users' input.

Pump id/name	Pump 1	Description
$S_{H_2}[l/s]$	%	Pumping speed for hydrogen
$S_{CH_4}[l/s]$	%	Pumping speed for methane
$S_{CO}[l/s]$	%	Pumping speed for carbon monoxide
$S_{CO_2}[l/s]$	%	Pumping speed for carbon dioxide

Special importance must also be paid to the implementation and robustness of the algorithm with respect to precision issues, which may arise when the matrix entries of the fundamental solution  $(\exp \mathbf{M} \cdot x)$  present very large values and thus causes in a next step an overflow error in Python. Since the matrix values  $M$  reflect units per unit length, we can only manipulate  $x$  in the solution. The idea is therefore to split the segments equally into smaller fractions and consider them as separate segments. Additional boundary conditions are implemented in between these two segments that present the density continuity  $n_{seg1} = n_{seg2}$  and a flux continuity of zero pumping and zero gas sources.

**Table 2.5.:** Template for the input file for one gas-source. The place holder % indicates the users' input.

Gassource id/name	Gassource 1	Description
$g_{H_2}[l/s]$	%	Gas release of hydrogen
$g_{CH_4}[l/s]$	%	Gas release of methane
$g_{CO}[l/s]$	%	Gas release of carbon monoxide
$g_{CO_2}[l/s]$	%	Gas release of carbon dioxide

## 2. VACUUM SIMULATIONS IN HIGH ENERGY ACCELERATORS

**Table 2.6:** Template for the input file for one material. The place holder % indicates the users' input.

Material id /name	Description
Sticking Probability	% CO <sub>2</sub>
$\eta_i$ (molecules/ion)	sticking coefficient ion induced desorption
% H <sub>2</sub>	% CO
% (H <sub>2</sub> by H <sub>2</sub> <sup>+</sup> )	% (H <sub>2</sub> by CO <sup>+</sup> )
% (CH <sub>4</sub> by H <sub>2</sub> <sup>+</sup> )	% (CH <sub>4</sub> by CO <sup>+</sup> )
% (CO by H <sub>2</sub> <sup>+</sup> )	% (CO by CO <sup>+</sup> )
% (CO <sub>2</sub> by H <sub>2</sub> <sup>+</sup> )	% (CO <sub>2</sub> by CO <sup>+</sup> )
$\eta_e$ (molecules/electron)	electron induced desorption
% H <sub>2</sub>	% (CO <sub>2</sub> )
% (H <sub>2</sub> )	% (CO <sub>2</sub> )
$\eta P_h$ (molecules/photon)	photon induced desorption
% H <sub>2</sub>	% (CO <sub>2</sub> )
% (H <sub>2</sub> )	% (CO <sub>2</sub> )
Linear pumping (l/s)	linear pumping speed
Out-gassing rate (mbar l/s cm <sup>2</sup> )	thermal desorption
% CH <sub>4</sub>	% (CO <sub>2</sub> )
% (H <sub>2</sub> by CH <sub>4</sub> <sup>+</sup> )	% (H <sub>2</sub> by CO <sup>+</sup> )
% (CH <sub>4</sub> by CH <sub>4</sub> <sup>+</sup> )	% (CH <sub>4</sub> by CO <sup>+</sup> )
% (CO by CH <sub>4</sub> <sup>+</sup> )	% (CO by CO <sup>+</sup> )
% (CO <sub>2</sub> by CH <sub>4</sub> <sup>+</sup> )	% (CO <sub>2</sub> by CO <sup>+</sup> )

## 2.4. SIMULATION RESULTS FOR THE FCC

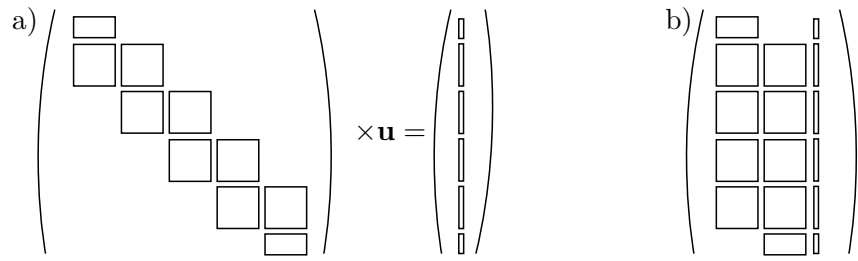


**Figure 2.8.:** Memory arrangement of final matrix equation in PyVasco.

Solution in programming code:

$$\begin{aligned}
 \mathbf{y}(x) &= \mathbf{P}(x)\mathbf{u} + (\mathbf{P}(x) - \mathbf{I}_8)\mathbf{M}^{-1}\mathbf{b} \\
 &= \mathbf{P}(x)\mathbf{u} + \mathbf{P}(x) \cdot \mathbf{M}^{-1}\mathbf{b} - \mathbf{M}^{-1}\mathbf{b} \\
 &= \mathbf{P}(x) \cdot \underbrace{(\mathbf{u} + \mathbf{M}^{-1}\mathbf{b})}_{=:Ps''} - \mathbf{M}^{-1}\mathbf{b}
 \end{aligned}$$

**VASCO in Python** The mathematical model was already implemented in a Matlab environment [16] in 2004. The passage from VASCO to PyVasco had a significant impact on the performances both in terms of memory storage and in computational efficiency. Furthermore, the new code has been designed in order to offer an increase usage flexibility, providing the user a better overview of the simulation domain in the input data and extend the possibility to include external data of the impinging synchrotron radiation and electron flux in the longitudinal direction of the accelerator from codes as PyECLLOUD [40] and SynRad+ [56]. Additionally, a graphical user interface built on PyQt4, SciPy and NumPy increases the user friendliness and enables a post-analysis of the data (see Fig. 2.9 and Fig. 2.10). The old Input-files of VASCO can be automatically transformed into the new object oriented format by using the optional button "Transform".

This Python project is structured into three subcategories:

- Data Loader: reads in all the data from a csv-file and stores them in a memory-friendly way.
- Core: Solves the mathematical problem from Eq. (2.6), strong use of libraries as SciPy and NumPy.
- Plotter: Gaphical realisation of the results, supported the scientific plotting library PyQt.
- It-Safety: unit tests.

## 2.4. Simulation results for the FCC

PyVasco was especially developed to predict the vacuum performance for the FCC. Many changes in its input parameters probably take place until the year of its construction and many more iterations

## 2. VACUUM SIMULATIONS IN HIGH ENERGY ACCELERATORS



**Figure 2.9.:** A screenshot of the graphical user interface PyVasco that shows the final residual gas density profile.

in its design, material choice and beam related parameters are still required. The simulations of PyVasco should provide an aid to choose among the different solution options and to identify the range of the key-input parameters to guarantee the needed vacuum quality.

The FCC describes a circular ring, that is divided into eight arcs with long straight sections (LSS) inbetween. Four LSS host beam collision points, the other four are dedicated to beam acceleration, longitudinal and transversal collimation and extraction, see a schematic of the layout in Fig. 2.11. The vacuum systems of the FCC-ee and -hh distinguish basically in all aspects, except of the circumference of the machine [57, 58]. We present two separate preliminary design examples for their vacuum systems. Both simulations focus on the interaction region of the machine. The choice of the material is crucial, and the conditioning time of the beam chamber surface should be as short as possible, so that the nominal luminosity with low background can be reached quickly. Beam instabilities and beam blow-up due to excessive electron clouds, synchrotron radiation and fast-ion instabilities should be avoided. Despite these high requirements we need easy-to manufacture vacuum chambers and efficient and cost-effective pumping systems. We initiated the design with using existing and proven technologies from the LHC and LEP<sup>3</sup> and improved further the design to the requirements for the FCC.

### 2.4.1. FCC-hh

The fundamental design of the hadron version of the FCC has been derived from the LHC <sup>4</sup> based on the the information from the LHC design report [36, 60]. However, the FCC-hh brings hadrons

<sup>3</sup>Large Electron-Positron Collider: predecessor of the LHC in the same tunnel.

<sup>4</sup>For the reference, a detailed simulation for the LHC has been carried out in the paper [1].

## 2.4. SIMULATION RESULTS FOR THE FCC

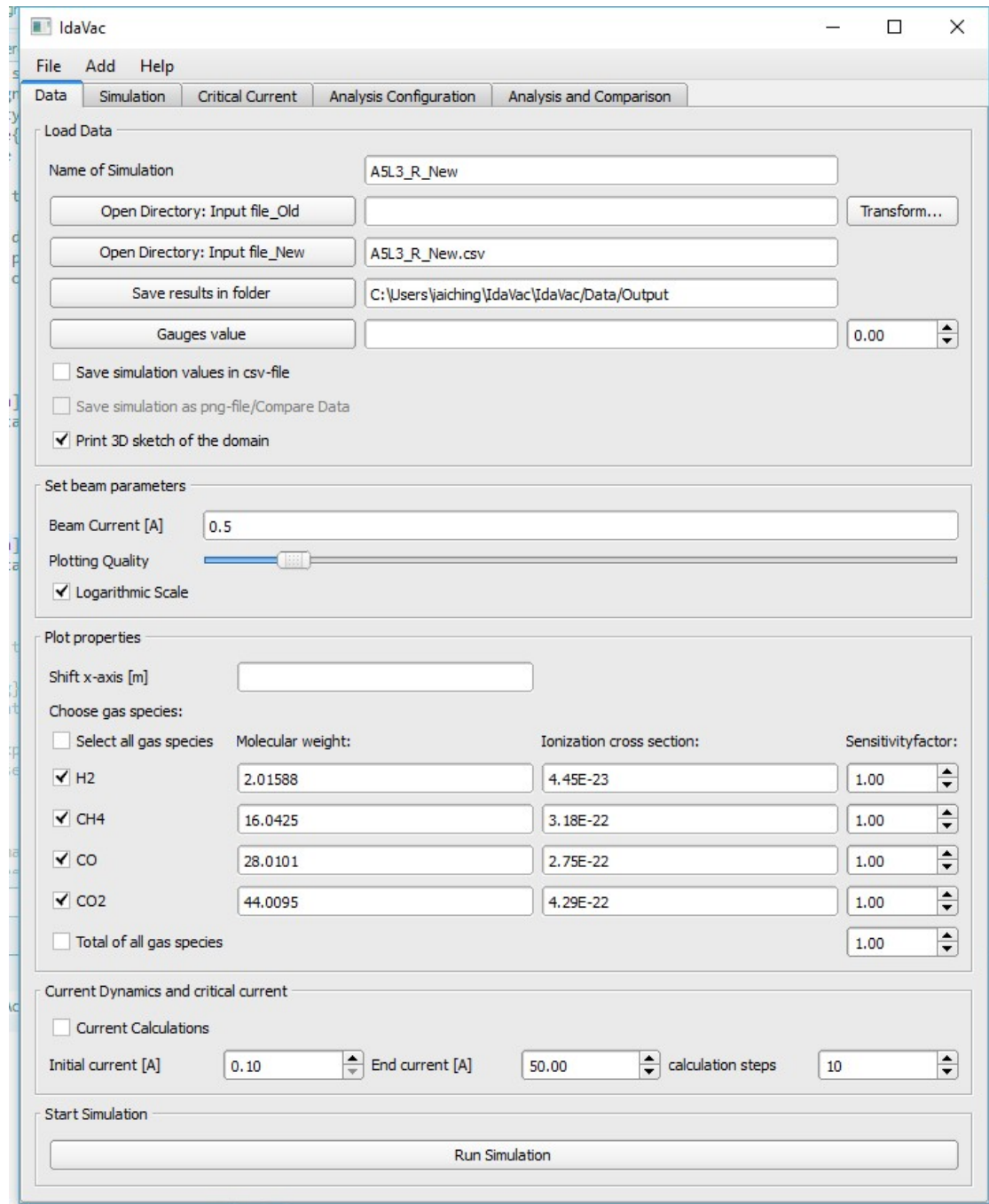


**Figure 2.10.:** A screenshot of the graphical user interface PyVasco that shows the configuration window of the input data.

## 2. VACUUM SIMULATIONS IN HIGH ENERGY ACCELERATORS

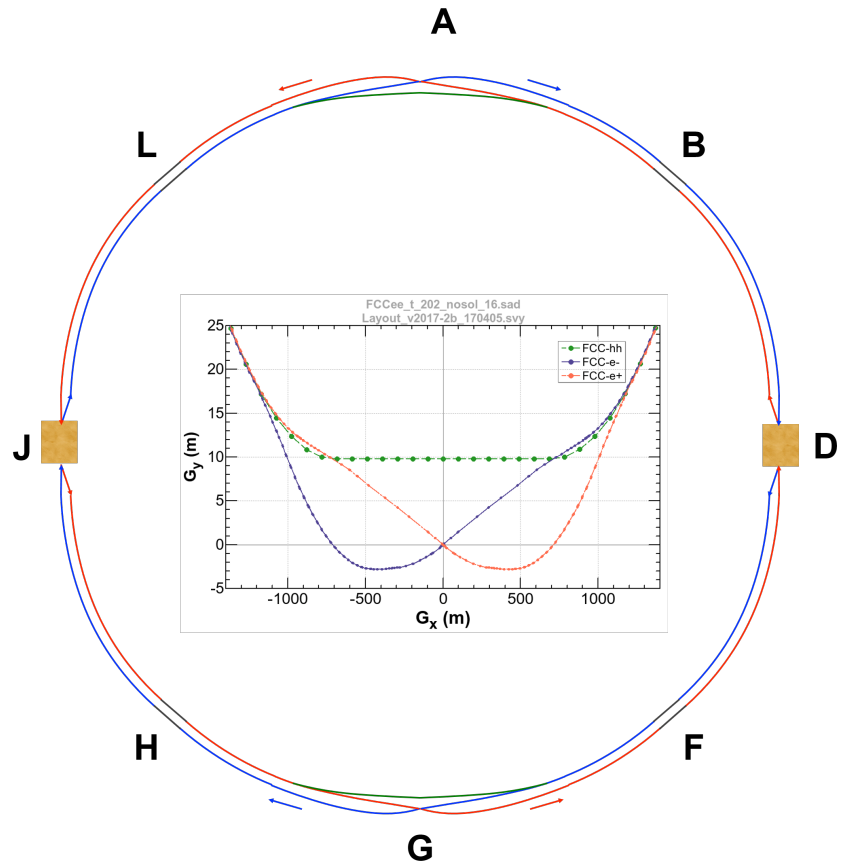


**Figure 2.11.:** Layout of the FCC: FCC-hh (green line), FCC-ee (red and blue line) with a zoom on the asymmetric layout of the FCC-ee in the figure in the middle. The LSS are marked with letters. A and G describe the two main collision points, D and J the specific experiments and the other letters describe the injection, extraction, collimation and acceleration LSS, similar graphic found in [59].

## 2.4. SIMULATION RESULTS FOR THE FCC

into collision at 100 TeV in the centre of mass that rises a number of issues which need to be analysed and optimised. The required average pressure in the machine is determined by the beam lifetime of 100 h. This implies a five times better vacuum quality compared to the LHC, which corresponds to a total density of

$$n = 2 \cdot 10^{14} \text{ particles/m}^3$$

In Fig. 2.13 we can see a simulation example of the LSS of the FCC-hh with a collision point in the middle. For this simulation the following main changes have been made in comparison to the LHC:

The main parameter, that causes all further changes is the increase of the beam energy from 7 TeV to 50 TeV. Hence the impact of the beam-induced parameters on the vacuum quality increases, in particular the synchrotron radiation. Its flux and its critical energy present a challenge. The formula for the generated synchrotron radiation from the bending dipoles calculated with Eq (2.2)-(2.3), yields (see also spectra in Fig. 2.3) a photon flux of

$$\dot{\Gamma} = 1.9 \cdot 10^{17} \text{ photons / (m s)}$$

and a critical energy of

$$E_c = 4269 \text{ eV},$$

with a bending radius of  $\rho = 10500$  m, a beam current of 0.5 A and a beam energy of 50 TeV.

The higher photon flux and the much higher critical energy with respect to the LHC lead to an improved design of the beam screen in the cryogenic area. A slot opening on both sides of the screen should extract the generated photons and reduce interactions between the beam and the photons. Moreover, the operation temperature in the cryogenic area will be 50 K instead of 10 K, because the heat deposition due to the synchrotron radiation is significant higher. The aperture of the beam screen is much smaller, just approximately 34 mm in diameter compared to 48 mm at the LHC. Fig. 2.12 shows a photography of the first prototype of the beam screen.

The length of the magnetic region is four times longer in the FCC and the magnets are stronger, for instance the bending dipoles provide a magnetic strength of 16 T instead of 8 T. The separation and recombination dipoles installed in the chamber, where the two beam pipes join, will be kept at cryogenic temperature (in contrast to the LHC).

New coating and material treatments are under research to reduce the desorption yield of photon-electron or ion bombardment (e.g. amorphous carbon coating, LESS). The goal actually would be to suppress the build-up of electron clouds completely with sophisticated surface material treatments.

Summing up, the development of the beam screen, has influenced the simulations in the size of

## 2. VACUUM SIMULATIONS IN HIGH ENERGY ACCELERATORS



**Figure 2.12.:** Right-hand side: LHC beam screen [61] and left-hand side: Prototype of a FCC-hh beam screen; the generated photons can escape through the slot on the side [62].

the diameter, the operating temperature, and thus the conductance (see Eq. (2.6)), as well as the value of the photon flux due to the additional pumping from the slots and the higher magnetic field. A concrete value for the latter is still under discussion and results are awaited from a similar experimental setup<sup>5</sup>. I set therefore the value, that is calculated above. The room temperature system in the long straight sections will mainly consist of NEG coated vacuum chambers, as it was done for the LHC. Additionally, also machine equipment such as collimators and beam instruments should be coated with NEG. However, the latter still provide a higher outgassing compared to normal copper NEG coated chambers. The cryogenic system relies on the physisorption on the beam screen. Due to the higher temperature, H<sub>2</sub> is not pumped efficiently anymore. The new developed material has to compensate that and I assumed therefore an additional sticking factor for H<sub>2</sub>.

Table 2.7 summarizes the main mentioned differences in the accelerator parameters of the LHC and the FCC and adds some further interesting characteristics as bunch intensity, synchrotron power, or the peak luminosity, that influence vacuum indirectly in for example the electron cloud-parameter.

---

<sup>5</sup>Synchrotron radiation flux spectrum at 50 TeV is comparable to that of the 3<sup>rd</sup> generation light source in ANKA [63].

## 2.4. SIMULATION RESULTS FOR THE FCC

**Table 2.7.:** Characteristic parameters for the FCC-hh from [64] and Eq. (2.2)-(2.3)

parameter	FCC-hh	LHC
residual gas particle density [1/m]	$2 \cdot 10^{14}$	$10^{15}$
circumference [km]	97.75	26.7
bending radius [m]	10500	2963
collision energy [TeV]	100	14
beam energy [TeV]	50	7
dipole field [T]	16	8.33
beam current [A]	0.5	0.58
bunch intensity [ $10^{11}$ ]	1	1.15
bunch spacing [ns]	25	25
photon flux [photons/(m s)]	$1.9 \cdot 10^{17}$	$9 \cdot 10^{16}$
synchrotron radiation power [W/m]	40	0.2
critical photon energy [eV]	4270	41.5
peak luminosity [ $10^{34} \text{cm}^{-2}\text{s}^{-1}$ ]	5	1
temperature of beamscreen [K]	50	5-20
aperture of beamscreen [cm <sup>2</sup> ]	$30 \times 24$	$46 \times 30$

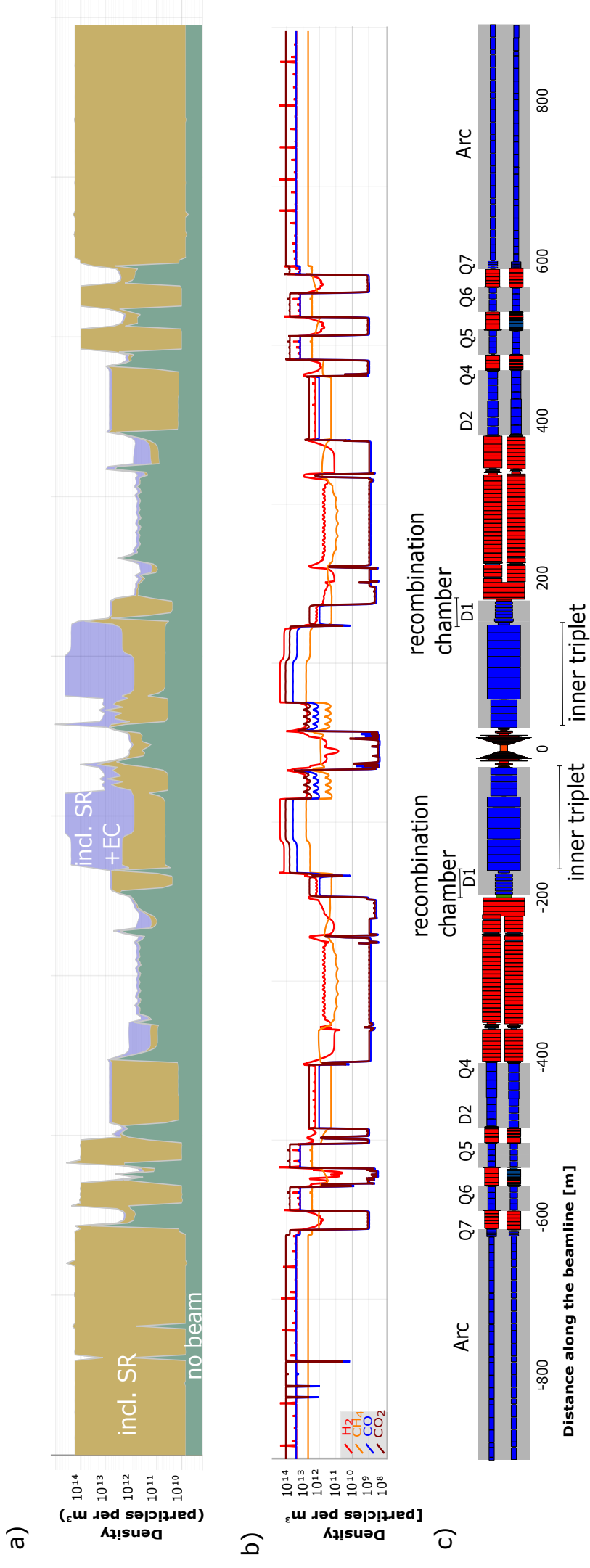


**Figure 2.13:** Simulation example of the LSS from the FCC-hh with an experiment in the middle. Plot a) presents a parameter variation of the total density in the case of no-beam (green), with synchrotron radiation (yellow) and with synchrotron radiation and electron clouds (blue). Plot b) presents the density profile of the four gas species H<sub>2</sub>, CH<sub>4</sub>, CO and CO<sub>2</sub> in the presence of electron clouds and synchrotron radiation. Plot c) shows a schematic of the beam chamber, where the acronyms D and Q stand for dipoles and quadrupoles.

### 2.4.2. FCC-ee

The Fcc-ee is an  $e^+e^-$  circular collider designed to accommodate four different operations modes in a beam collision energy range from 91 GeV to 350 GeV in the centre of mass to obtain unprecedented precision in Z, W, Higgs and top measurements (summarized in Table 2.8). One of the most critical aspects of this machine is again the very high and powerful synchrotron radiation production, which challenges the maintenance of a stable ultra high vacuum system. The most challenging operation mode for vacuum, will be the 91 GeV machine (also referred to Z-pole machine) with a current of almost 1.4 A. The photon flux and the synchrotron radiation power respectively yields from Eq (2.2)-(2.3) (synchrotron radiation in LEP is summarized here: [65]),

$$\dot{\Gamma} = 7.7 \cdot 10^{17} \text{ photons / (m s)}$$

$$E_c = 20000 \text{ eV}$$

So far, it was decided to keep the beam pipes at room temperature as in the case of KEKB, SuperKEKB and other lepton colliders. The cross-section of the vacuum chamber is a circle made of copper and without NEG coating, due to resistive-wall instability reasons. Therefore two small winglets in the plane of the orbit are implemented that provide space for a small distributed pumping surface to cope with the synchrotron radiation induced desorption, see Fig. 2.14. Otherwise, the pumping system consist only of lumped pumps. The experimental area close to the collision point is asymmetric to prolong the straight section of the incoming beam and to reduce the photon bombardment on the detectors. Additionally, absorbers close to the collision point are considered in the simulation, to shield the synchrotron radiation. The simulation in Fig. 2.15 shows an example of its vacuum system with a photon flux of  $\mathcal{O}(10^{15})$  and zero electron flux. Their concrete values for the four energy ranges still need to be defined. Optimally, they are close to zero since the chamber does not provide a significant surface pumping. The interaction region of the simulation is very short, in total less than 2 m and typically made out of beryllium with a diameter of 40 mm. The diameter increases in the recombination chamber to 70 mm, decreases to 24 mm, where the focusing quadrupoles are located and increases again in the arcs to 70 mm. Roughly 85 % of the 100 km circumference is made up by the arcs.

## 2.5. Validation and error estimation

The model has been tested for validation by a cross-check to similar simulation programs as LTSpice, Molflow+ [38, 56] and a parameter sensitivity analysis. In the second step the simulation outputs of PyVasco were validated with a comparison to LHC gauge readings (real-time values of

## 2. VACUUM SIMULATIONS IN HIGH ENERGY ACCELERATORS

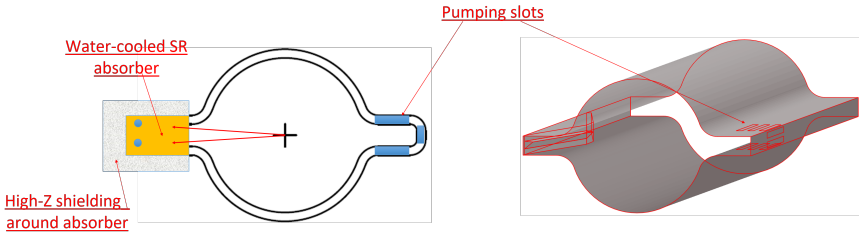


**Figure 2.14.:** Circular cross-section of the FCC-ee with winglets on the side to cope with the impinging synchrotron radiation [66].

**Table 2.8.:** Characteristic parameters for the FCC-ee from [67] and Eq. (2.2)-(2.3)

parameter	Z	W	H	tt
beam energy [GeV]	45.6	80	120	175
bending radius of arc dipole [km]	11			11
beam current [A]	1.45	0.152	0.03	0.0066
bunches / beam	30180	5260	780	81
particles per bunch[10 <sup>11</sup> ]	1.0	0.6	0.8	1.7
bunch spacing [ns]	7.5	50	400	4000
synchr. rad. power [W]	728	724	723	720
luminosity / IP [10 <sup>34</sup> cm <sup>-2</sup> s <sup>-1</sup> ]	207	19.1	5.1	1.3
critical photon energy $E_c$ (keV)	20	104	349	1080
photon flux [10 <sup>17</sup> ]	7.7	1.4	0.42	0.14
power/beam [MW]	50	50	50	50

gauges and beam chamber layout from the official databases [68–70]). The crosscheck of Molflow and the LHC is published and described in [1].

## 2.6. Physics at the FCC

In 2012, two experiments, CMS and Atlas at the LHC confirmed the discovery of the Higgs, the final missing puzzle piece of the Standard Model to describe all of the known fundamental particles. This was a remarkable scientific achievement, that lifted particle physics into a new era. A new

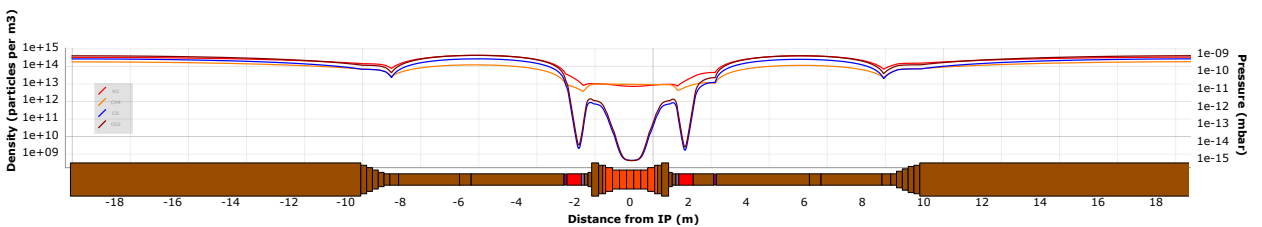


**Figure 2.15.:** Simulation example of the vacuum system for the FCC-ee.

## 2.7. SUMMARIZED PARAMETER AND VARIABLE ACRONYMS

larger, more powerful accelerator is now needed to address new frontier of fundamental questions. Firstly, the motivation lies in the further understanding of the Higgs that should dictate some clear physics targets. Today, there exist many parallel theories beyond the Standard Model. To understand better which one to follow, every aspect of the Higgs must be understood. Moreover, the Higgs boson is uncharged and carries no spin, so it can interact readily with uncharged dark matter. The FCC-ee machine would provide high-accuracy measurements to analyse the quantum mechanics of the Higgs boson, whereas FCC-hh would produce Higgs bosons with a high production rate, which allows to explore the structure of the Higgs potential and observe related extremely rare decays. The potential indicates more than one minima and any modification of its form would imply huge consequences on the physics-theory.

Secondly, dark matter constitutes about 85% of the matter in nature and despite overwhelming evidence for its existence, the particle nature of dark matter is unknown and not included in the Standard Model. The theory of super-symmetry is one attempt among several to further understand the inequality between matter and anti-matter.

Thirdly, the motivation for the FCC lies in the understanding of the neutrino masses. The standard model cannot explain this and it is already a long-outstanding question in fundamental physics. Lastly, there is a strong motivation for the existence and discovery of new particles and new weak forces in the multi TeV-range.

The design study of the FCC, indirectly implies development in technology to meet the construction requirements.

## 2.7. Summarized parameter and variable acronyms

Table 2.9-2.11 summarize all variables, parameters and constants of the physical and mathematical description.

## 2. VACUUM SIMULATIONS IN HIGH ENERGY ACCELERATORS

**Table 2.9.:** Model parameters for physical description.

Symbol	Dim	Unit	Description
$P$	$\mathbb{R}$	eV	Power of photons
$E$	$\mathbb{R}$	eV	beam energy
$\rho$	$\mathbb{R}$	m	bending radius of a dipole
$E_c$	$\mathbb{R}$	eV	critical energy; median of synchrotron radiation spectrum
$\mathbf{n}$	$\mathbb{R}^4$	Particles/m <sup>3</sup>	vector-valued particle density function of H <sub>2</sub> , CH <sub>4</sub> , CO and CO <sub>2</sub>
$\Theta$	$\mathbb{R}^4$	Particles/m <sup>2</sup>	density on lateral surface of beam chamber
$\mathbf{a}$	$\mathbb{R}^4$	m <sup>4</sup> /s	Specific conductance
$\mathbf{r}$			Sinks of a UHV-system
$\mathbf{q}$			Sources of a UHV-system
$\eta_{ph}$	$\mathbb{R}^4$	1	Photon induced desorption yield ( $\eta \geq 0$ ) describes the number of molecules desorbed per photon
$\dot{\Gamma}_{ph}$	$\mathbb{R}$	photons/(s · m)	Emitted photon flux by the bended beam in the magnetic areas
$\eta_e$	$\mathbb{R}^4$	1	Electron induced desorption yield ( $\eta \geq 0$ ) describes the number of molecules desorbed per electron
$\dot{N}_e$	$\mathbb{R}$	electrons/(s · m)	Electron flux impinging on the chamber wall due to the electron cloud phenomena
$\sigma$		ion/proton · m <sup>2</sup>	Ionisation cross section of residual gas molecules by high energy protons
$\mathbf{H}_{ion}$	$\mathbb{R}^{4 \times 4}$	1	Ion induced desorption yield, probability that ion of species $i$ desorbs molecule of species $j$ for $i, j \in \{\text{H}_2, \text{CH}_4, \text{CO}, \text{CO}_2\}$
$\dot{I}_{ion}$	$\mathbb{R}$	ion/(s · m)	Ion flux, it is proportional to n
$\frac{I}{e}$		$\frac{1}{s}$	Number of high energy protons passing per second
$A$	$\mathbb{R}$	m	Lateral surface per unit-length of beam chamber
$\mathbf{q}_{th}$	$\mathbb{R}^4$	1/(m <sup>2</sup> s)	Thermal outgassing rate; the unit of $[\tilde{\mathbf{q}}] = [\frac{\text{mbar}^{-1}}{\text{s} \cdot \text{cm}^2}]$ is more common.
$\alpha$	$\mathbb{R}^4$	1	Sticking coefficient
$\bar{v}$	$\mathbb{R}^4$	m/s	Average Maxwell-Boltzmann velocity of the four gas species
$\chi_{\text{cryo}}$	$\mathbb{N}$		$\chi = 1$ for cryogenic areas and 0 for room temperature areas
$\mathbf{n}_e$	$\mathbb{R}^4$	1/m <sup>3</sup>	Background density without beam (static density)
$p_l$	$\mathbb{R}^4$	m <sup>2</sup> /s	Linear pumping per unit-length
$N$	$\mathbb{R}$	1	Number of segments
$d$	$\mathbb{R}$	m	Diameter
$L$	$\mathbb{R}$	m	Length of segment
$T$	$\mathbb{R}$	K	Absolute temperature of segment; [K] = [°C] + 273.15
$s_k$	$\mathbb{R}^4$	m <sup>3</sup> /s	Pumping speed of pump located at the beginning of segment $k$
$x$	$\mathbb{R}$	m	Spatial coordinate along beam line
$x_k$	$\mathbb{R}$	m	Intersection point of segment $k - 1$ and $k$
$\mathbf{g}$	$\mathbb{R}^4$	1/s	Local punctual gas source (e.g. gas leak)
$p$	$\mathbb{R}$	Pa	Total pressure
$\mathbf{p}$	$\mathbb{R}^4$	Pa	Equivalent pressure for particle density $\mathbf{n}$ using ideal gas equation

## 2.7. SUMMARIZED PARAMETER AND VARIABLE ACRONYMS

**Table 2.10.: Variables used in the mathematical model.**

Symbol	Dim	Description
$n(x)$	$\mathbb{R}$	Particle density for one gas species (Single-gas framework)
$a, b, c$	$\mathbb{R}$	Coefficients of balance equation for one gas species (Single-gas framework)
$C_1, C_2$	$\mathbb{R}$	Integration constants of balance equation
$\alpha, \beta, \gamma$	$\mathbb{R}$	Coefficients in front of integration constants $C_1, C_2$
$S_k, g_k$	$\mathbb{R}$	Pumping speed and gas release for one gas species at the beginning of segment $k$
$SM$	$\mathbb{R}^{(2\cdot N) \times (2\cdot N)}$	Matrix containing information of the boundary conditions (single-gas framework)
$w$	$\mathbb{R}^{(8\cdot N)}$	Vector containing information of the boundary conditions (single-gas framework)
$\mathbf{y}$	$\mathbb{R}^8$	vector-valued function describing the residual gas particle density and its derivative
$\mathbf{I}_4$	$\mathbb{R}^{4 \times 4}$	Identity matrix
$\mathbf{0}_{4 \times 4}$	$\mathbb{R}^{4 \times 4}$	Zero matrix
$\vec{0}_4$	$\mathbb{R}^4$	zero vector
$x$	$\mathbb{R}$	Spatial coordinate along beam line
$x_k$	$\mathbb{R}$	Intersection point of segment $k - 1$ and $k$
$\mathbf{A}, \mathbf{B}$	$\mathbb{R}^{4 \times 4}$	Coefficients of balance equation , e.g. $A_{11} = a$ from the single-gas framework
$\mathbf{c}$	$\mathbb{R}^4$	Coefficients of balance equation
$\mathbf{M}$	$\mathbb{R}^{8 \times 8}$	Coefficients of transformed balance equation
$\mathbb{M}$	$\mathbb{R}^{4 \times 4}$	Is equal to $-\mathbf{A}^{-1}\mathbf{B}$
$\mathbf{b}$	$\mathbb{R}^8$	Coefficients of transformed balance equation
$\mathbf{P}(\mathbf{x})$	$\mathbb{R}^{8 \times 8}$	Fundamental system of transformed balance equation
$\mathbf{z}(\mathbf{x})$	$\mathbb{R}^8$	Particular solution of transformed balance equation
$\mathbf{u}$	$\mathbb{R}^8$	Integration constants of balance equation
$\bar{\mathbf{u}}$	$\mathbb{R}^8$	Integration constants of balance equation with an artificial extra vector entry at the end.
$\mathbf{F}_1, \mathbf{F}_N$	$\mathbb{R}^{4 \times 8}$	Coefficients of boundary conditions
$\mathbf{H}, \mathbf{S}$	$\mathbb{R}^{8 \times 8}$	Coefficients of intersection conditions
$\mathbf{H}_{\text{ion}}$	$\mathbb{R}^{4 \times 4}$	Ion- induced desorption matrix
$\mathbf{g}$	$\mathbb{R}^4$	Local lumped gas source (e.g. leak)
$s_k$	$\mathbb{R}^4$	Pumping speed of lumped pump located at the beginning of segment $k$
$\bar{\mathbf{g}}$	$\mathbb{R}^8$	Coefficients of intersection conditions
$\mathbf{SM}$	$\mathbb{R}^{(8\cdot N) \times (8\cdot N)}$	Matrix that contains information of the boundary conditions

## 2. VACUUM SIMULATIONS IN HIGH ENERGY ACCELERATORS

**Table 2.11.:** Values for most common physical constants.

Symbol	Description	unit	Value
$\hbar$	reduced Planck's constant	$eV \cdot s$	$6.58 \cdot 10^{-16}$
c	velocity of light	m/s	$2.998 \cdot 10^8$
e	elementary electric charge	C	$1.6 \cdot 10^{-19}$
m	proton rest energy	MeV	938
m	electron rest energy	MeV	0.511
$\epsilon_0$	vacuum dielectric constant	F/m	$8.854 \cdot 10^{-12}$
$k_B$	Boltzmann constant	J/K	$1.3806488 \cdot 10^{-23}$
eV	electronvolt	J	$1.6 \cdot 10^{-19}$
TeV	tera-electronvolt	eV	$10^{12}$
GeV	giga-electronvolt	eV	$10^9$
MeV	mega-electronvolt	eV	$10^6$
mbar	millibar	Pa	0.01
Torr	torr	Pa	133.3



# CHAPTER 3

---

## Sets of Bounded Remainder for the Billiard on a Square

---

A *billiard path* describes the trajectory of a billiard ball, that moves in a straight line until it hits a boundary of the unit square. The reflection off the edge is elastic, meaning that it rebounces, such that the incident angle is equal to the angle of reflection. After the reflection it continues its linear curve with the new direction and the same total velocity until it hits the boundary again, and so forth. A starting point  $\underline{x}$  and an initial slope  $\alpha$  uniquely determine an infinite piecewise linear billiard path  $X(t) = (x(t), y(t))$ ,  $0 < t < \infty$  in the unit square (see Figure 3.1).

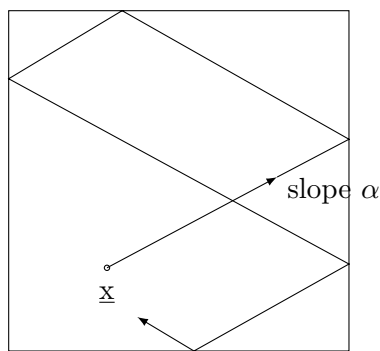


**Figure 3.1.:** Billiard path wit starting point  $\underline{x}$  and slope  $\alpha$ .

This simple continuous and piecewise linear path presents a powerful tool in challenging topics of quantum mechanics (simulation of particle in a box, see this thesis in the next Chapter 4.4) and in Quasi-Monte Carlo (QMC) methods. The latter is investigated in this chapter and the corresponding paper [2]. Specific properties of the billiard path are analysed in favour of selecting a point set that is appropriate for QMC-methods.

### 3.1. Monte-Carlo vs. Quasi Monte Carlo methods

Monte Carlo (MC) and QMC describe a numerical method to approximate integrals of the general form

$$\int_{\mathbb{R}^d} f(\mathbf{x}) d\mathbf{x}, \quad (3.1)$$

commonly found in various applications of physics, economy, industry, medicine and biology that can not be calculated analytically. These methods aim to reduce the integrals complexity and approximate its value by function evaluation to any prescribed level of accuracy. Definitions and basic principles are revised from [9–11, 71]. The general idea is first to restrict the integral to a bounded region and to transform it into standardized form:

$$\int_0^1 \cdots \int_0^1 f(x_1, \dots, x_d) dx_1 \cdots dx_d = \int_{[0,1]^d} f(\mathbf{x}) d\mathbf{x} \quad (3.2)$$

The next step uses the strong law of large numbers from probabilistic theory. This law guarantees for integrable functions  $f$  and independent and identically distributed random variables  $\mathbf{x}_0, \dots, \mathbf{x}_{N-1}$  that the term

$$\frac{1}{N} \sum_{n=0}^{N-1} f(\mathbf{x}_n). \quad (3.3)$$

converges to the integral in (3.2) almost surely as  $N \rightarrow \infty$ .

We call this method *MC integration*, if the quadrature points  $\mathbf{x}_n$  used in (3.3) are independent random sample points. The generation of random samples is a fundamental difficulty, which is in practice overcome by the use of pseudo-random numbers, i.e. a deterministic sequence of numbers characterized by statistical properties, that mimic randomness.

A computing method for numerical integration is the so-called *QMC integration*, where deterministic very carefully constructed quadrature points  $\mathbf{x}_n$  (that do not imitate randomness) are chosen to improve the convergence rate of the approximation. Measures for the quality of point sets  $\mathbf{x}_0, \dots, \mathbf{x}_{N-1}$  are the extreme discrepancy  $D_N$  and the star discrepancy  $D_N^*$ .

*Notation.* The expression  $\{x\}$  denotes the fractional part of  $x \Leftrightarrow \{x\} = x - \lfloor x \rfloor$  and  $\|x\|$  denotes the distance of a real number  $x$  from the nearest integer:  $\Leftrightarrow \|x\| = \min(\{x\}, 1 - \{x\})$ .  $I^2$  is commonly used to describe the unit square  $[0, 1] \times [0, 1]$ ;  $\chi$  is the characteristic function and  $\lambda$  describes the Lebesgue measure.

We will refer to these abbreviations in the following text.

**Definition 3.1** (Discrepancy). *Let  $\mathbf{x}_0, \dots, \mathbf{x}_{N-1}$  be a finite  $N$ -element point set in  $[0, 1]^d$  and let  $J$  be an interval in  $[0, 1]^d$ , then  $A(N, J) := \#\{n \in \mathbb{N}_0 : 0 \leq n \leq N - 1 \text{ and } \mathbf{x}_n \in J\}$  describes the number of indices  $n \in \{0, \dots, N - 1\}$  for which  $x_n \in J$ .*

### 3. SETS OF BOUNDED REMAINDER FOR THE BILLIARD ON A SQUARE

The extreme discrepancy of the point set  $\mathbf{x}_0, \dots, \mathbf{x}_{N-1}$  is defined as

$$D_N = D_N(\mathbf{x}_0, \dots, \mathbf{x}_{N-1}) := \sup_{J_1 \in [0,1]^d} \left| \frac{A(N, J_1)}{N} - \lambda_d(J_1) \right| \quad (3.4)$$

with  $J_1 = [\mathbf{a}, \mathbf{b}] = \prod_{i=1}^d [a_i, b_i] \subset [0, 1]^d$ .

The star discrepancy considers a slightly simplified notion of  $D_N$  and is defined as

$$D_N^* = D_N^*(\mathbf{x}_0, \dots, \mathbf{x}_{N-1}) := \sup_{J_2 \in [0,1]^d} \left| \frac{A(N, J_2)}{N} - \lambda_s(J_2) \right| \quad (3.5)$$

with  $J_2 = \prod_{i=1}^d [0, \alpha_i] \subset [0, 1]^d$ .

The distribution error  $\Delta_N$  of the point set  $\mathbf{x}_0, \dots, \mathbf{x}_{N-1}$  for an arbitrary Lebesgue measurable subset  $J_3 \in [0, 1]^d$  is defined by:

$$\Delta_N(J_3) = A(N, J_3) - N \cdot \lambda_d(J_3)$$

For an infinite sequence  $(\mathbf{x}_n)_{n \geq 0}$  the discrepancy  $D_N$  is the discrepancy of the first  $N$  elements of the sequence. The same holds for the star discrepancy  $D_N^*$ .

When using numerical integration one is usually interested in the *integration error*,

$$\text{error} = \left| \int_{[0,1]^d} f(\mathbf{x}) d\mathbf{x} - \frac{1}{N} \sum_{n=0}^{N-1} f(\mathbf{x}_n) \right| \quad (3.6)$$

made by this approximation. We obtain the following error bounds [11] for MC

$$\mathbb{E}(\text{error}) = \mathcal{O}\left(\frac{1}{\sqrt{N}}\right) \quad (3.7)$$

and for QMC, if  $x_0, \dots, x_{N-1}$  presents a good point set ( $D_N \rightarrow 0$ , see Th. 3.2)

$$\text{error} \leq \frac{\log(N)^{d-1}}{N}, \quad (3.8)$$

where  $d$  defines the dimension of the integral.

This concludes that for large  $N$  and small  $d$ , we obtain clearly the following relation of the error bounds (see also Fig. 3.2):

$$\frac{\log(N)^{d-1}}{N} \ll \frac{1}{\sqrt{N}}, \quad (3.9)$$

which motivates the investigation of QMC methods and of the corresponding problem to find

### 3.1. MONTE-CARLO VS. QUASI MONTE CARLO METHODS

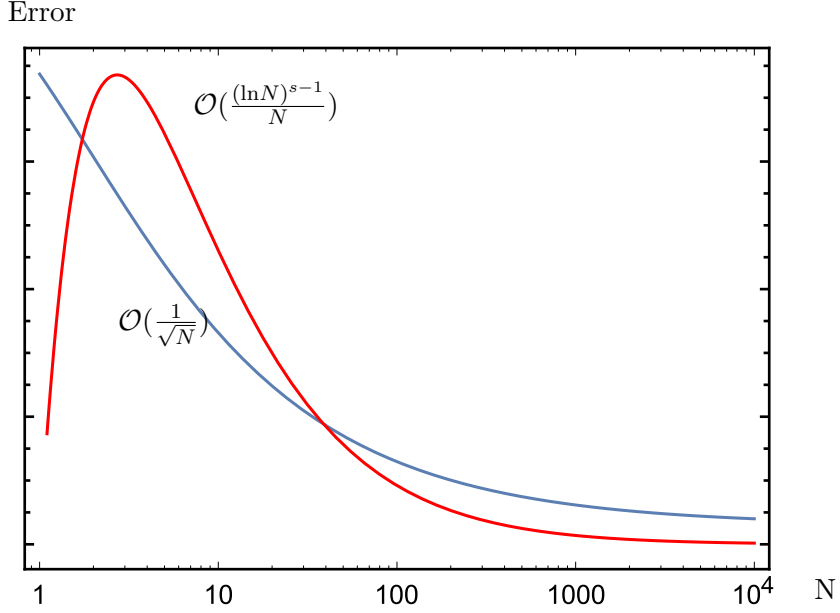


**Figure 3.2.:** Error bounds of numerical integration for MC (blue) and QMC (red) in a loglinear scale.

appropriate point sets  $x_0, \dots, x_{N-1}$ .

The relation between the integration error of a QMC method and the discrepancy of the chosen point set is described in following theorem, also known as the *Koksma-Hlawka inequality*:

**Theorem 3.2** (Koksma-Hlawka inequality). *Let  $f : [0, 1]^d \rightarrow \mathbb{R}$  be a function with bounded variation<sup>1</sup>  $V(f)$  on  $[0, 1]^d$  in the sense of Hardy and Krause, then for any point set  $\mathbf{x}_0, \dots, \mathbf{x}_{N-1} \in [0, 1]^d$ , we have*

$$\text{error} \leq V(f) D_N^*. \quad (3.10)$$

The nodes  $\mathbf{x}_n$  for a QMC method should come therefore from a low-discrepancy sequence that is described within the theory of Uniform Distribution Modulo One.

**Definition 3.3** (Uniform distributed point-sets). *An infinite sequence  $(\mathbf{x}_n)_{n \geq 0}$  in the  $d$ -dimensional unit-cube  $[0, 1]^d$  is said to be uniformly distributed modulo one, if for every interval  $[\mathbf{a}, \mathbf{b}] \subset [0, 1]^d$  we have*

$$\lim_{N \rightarrow \infty} \frac{A(N, [\mathbf{a}, \mathbf{b}])}{N} = \lambda_d([\mathbf{a}, \mathbf{b}]). \quad (3.11)$$

It can be proven (see, e.g., [72]) that a sequence  $(\mathbf{x}_n)_{n \geq 0} \in [0, 1]^d$  is uniformly distributed modulo one if and only if  $\lim_{N \rightarrow \infty} D_N(\mathbf{x}_0, \dots, \mathbf{x}_{N-1}) = 0$  (or equivalently,  $\lim_{N \rightarrow \infty} D_N^*(\mathbf{x}_0, \dots, \mathbf{x}_{N-1}) = 0$ ).

---

<sup>1</sup>Variation of a function describes its arc length.

### 3. SETS OF BOUNDED REMAINDER FOR THE BILLIARD ON A SQUARE

**Theorem 3.4.** *A sequence  $(\mathbf{x}_n)_{n \in \mathbb{N}_0}$  in  $[0, 1]^d$  is uniformly distributed modulo one if and only if for every Riemann integrable function  $f : [0, 1]^d \rightarrow \mathbb{R}$  we have*

$$\lim_{n \rightarrow \infty} \frac{1}{N} \sum_{n=0}^{N-1} f(\mathbf{x}_n) = \int_{[0,1]^d} f(\mathbf{x}) d\mathbf{x} \quad (3.12)$$

The proof is given for instance in [11].

The 1-dimensional *Kronecker sequence* turned out to be a good choice for a very large class of functions (continuous, Riemann, Lebesgue integrable) to create a uniformly distributed point set in the unit interval, if  $\alpha \in \mathbb{R} \setminus \mathbb{Q}$ , shown by Kesten in [73]:

**Definition 3.5.** *The discrete Kronecker sequence in the unit interval is defined as*

$$\left( \{n\alpha + \beta\} \right)_{n \geq 1} \quad (3.13)$$

where  $\alpha \in \mathbb{R}$  describes the spacing in-between the nodes and  $\beta \in \mathbb{R}$  defines a starting point.

**Theorem 3.6** (discrete Kronecker-Weyl Theorem). *For every Lebesgue measurable set  $S \subset [0, 1]$  and for every irrational  $\alpha$  and almost every  $\beta$  defining a Kronecker sequence, we have that,*

$$\lim_{N \rightarrow \infty} \frac{1}{N} A(N, S) = \lambda_1(S), \quad (3.14)$$

where  $A(N, S)$  is defined as in Definition 3.1.

The proof is given for instance in [11].

#### 3.1.1. Uniformly distributed curves

Instead of putting the focus on uniformly-distributed point-sets, we explore in this thesis the properties of well-distributed curves, in particular of the billiard path and the continuous rotation. First we review the framework of the distribution error in the continuous case:

The distribution error of a curve  $X(t)$  in the unit square is defined by the time that the curve spends in a given subset  $S$  in comparison to the size of  $S$ :

**Definition 3.7.** *Let  $T$  be a given finite time of the curve  $X(t) \in I^2$ . Then the **distribution error**  $\Delta_T$  for a subset  $S \subseteq I^2$  is defined by:*

$$\Delta_T(X(t), S) := \left| \int_0^T \chi_S(X(t)) dt - T \cdot \lambda_2(S) \right| \quad (3.15)$$

**Definition 3.8.** *A continuous curve  $X(t), t \geq 0$  in  $I^2$  is said to be **uniformly distributed modulo one** if and only if*

$$\limsup_{T \rightarrow \infty, S} \frac{1}{T} \Delta_T(S, X(t)) = 0. \quad (3.16)$$

### 3.1. MONTE-CARLO VS. QUASI MONTE CARLO METHODS

for any Lebesgue measurable subset of the unit square.

**Remark 3.9.** Regarding Definition 3.7: The time that the curve spends in the set  $S$  tends to infinity, when the time  $T$  goes to infinity. The second expression of the distribution error will also converge to infinity in this case. So the distribution error is only bounded, when these terms converge with the same speed.

We want to study now, when the distribution error  $\Delta_T$  is bounded:

**Definition 3.10.** For a curve  $X(t) \in [0, 1] \times [0, 1]$ , we define the **set of bounded remainders**  $\bar{S}$ . It contains all sets  $S$  that provide a bounded distribution error:

$$\bar{S}(X(t)) := \left\{ S \subseteq [0, 1] \times [0, 1] \mid \limsup_{T \rightarrow \infty} \Delta_T(X(t), S) < \infty \right\} \quad (3.17)$$

The discrete Kronecker sequence (Def. 3.5) has a continuous analogue defined as the *continuous rotation on the torus*. It describes a linear curve, but in contrast to the billiard path, when the curve hits the boundary, it comes back on the opposite of the boundary. The continuous rotation and the billiard path are mathematically described as:

**Definition 3.11.** Let  $s = (s_1, s_2)$  be a start point and let  $d = (d_1, d_2)$  be a unit vector, that describes the initial direction. The initial angle  $\alpha$  is given by:  $\alpha = \arctan(\frac{d_2}{d_1})$  [rad]. Then we can define two curves:  $\mathbb{R}^+ \rightarrow I^2$

- The **continuous rotation on the torus**  $R(t)$ :

$$R(t) := (\{s_1 + d_1 \cdot t\}, \{s_2 + d_2 \cdot t\}) \quad 0 \leq t < \infty \quad (3.18)$$

If the initial angle is irrational, then we refer to it as the **continuous irrational rotation**.

- The **billiard path**  $X(t)$ :

$$X(t) := (x(t), y(t)) \quad 0 \leq t < \infty \quad \text{with the } j^{\text{th}} \text{ coordinate equal to: } 2 \left\| \frac{s_j + t \cdot d_j}{2} \right\| \quad (3.19)$$

Similar to the discrete case (Theorem 3.6), the torus line and the billiard path describe a uniformly distributed curve in the unit square for irrational slopes  $\alpha$ . The similarity of the discrete and the continuous case is illustrated in Fig. 3.3:

**Theorem 3.12** (continuous Kronecker-Weyl Theorem). The time that the continuous rotation  $R(t)$  spends in any axes-parallel box  $S = I_1 \times \cdots \times I_d \subset [0, 1]^d$  is in the limit equal to the Lebesgue measure of  $S$  for any irrational  $\alpha$ :

$$\lim_{T \rightarrow \infty} \frac{1}{T} \int_0^T \chi_S(R(t)) dt = \lambda_d(S). \quad (3.20)$$

### 3. SETS OF BOUNDED REMAINDER FOR THE BILLIARD ON A SQUARE

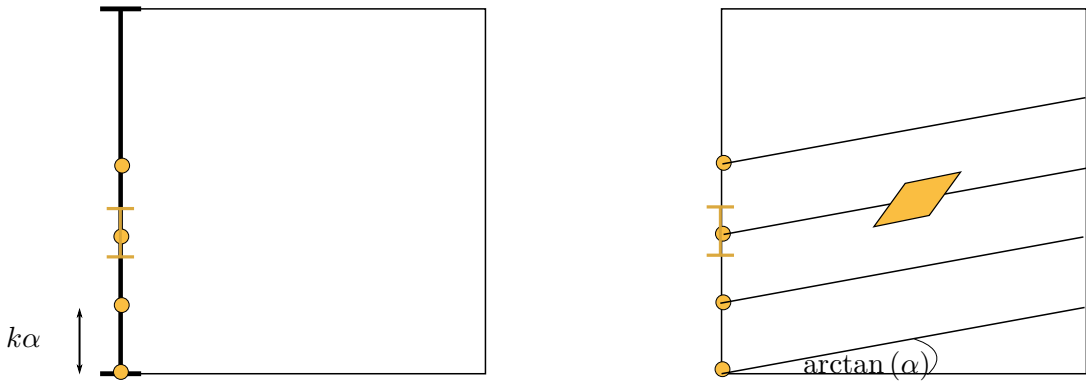


**Figure 3.3.:** Similarity of the Kronecker sequence and the torus line.

Observe that the discrete and the continuous Kronecker-Weyl Theorem have the same equidistribution properties from a qualitative point of view. Despite of this similarity, the speed of the convergence rates are different. The billiard path, which is via unfolding just a general continuous rotation (technique described in Subsection 3.2)- estimates the area of an arbitrary but fixed (measurable) subset  $A \subset [0, 1]^2$  with error  $\mathcal{O}(\sqrt{\ln T})$ , where  $T$  is the length of the time interval (shown by Beck in [12]). This result is based on the slightly weaker Theorem, also shown by Beck:

**Theorem 3.13** (Beck, [12]). *Let  $S$  be an arbitrary Lebesgue measurable set in the unit square  $[0, 1]^2$  with positive measure. Then for every  $\epsilon > 0$  and almost all  $\alpha$  and every starting point  $x = (x_1, x_2) \in I^2$ , we have*

$$\Delta_T < \mathcal{O}((\ln T)^{3+\epsilon})$$

Hence, comparing the error estimates for a billiard curve and a typical random sampling of a Monte Carlo method presents a big difference between the sizes of “distribution-errors”

$$\sqrt{\ln T} \text{ and } \sqrt{N} \tag{3.21}$$

for large  $T$  and  $N$ . Beck refers to this continuous property as the “super-uniformity”. We are investigating therefore the idea to replace the point sample by a ”curve“ sample, where the curve sample describes a billiard path. We are especially exploiting the statement of Beck posed in Theorem 3.13 about the logarithm error term and whether it is possible to improve it.

## 3.2. Summary of paper and an expanded detailed proof description

In the following, we were investigating, if certain regularity conditions on the test set  $S$  implies an even better convergence rate of the error, and indeed, we could show that polygons (with no slope  $\alpha$ ) or more general convex sets, with a twice differentiable boundary and with positive curvature everywhere, represent bounded remainder sets. This statement implies immediatly the weaker

### 3.2. SUMMARY OF PAPER AND AN EXPANDED DETAILED PROOF DESCRIPTION

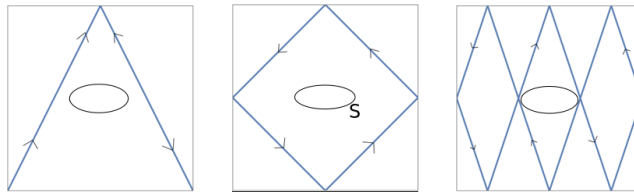


**Figure 3.4.:** Billiard path that repeats itself after a short time.

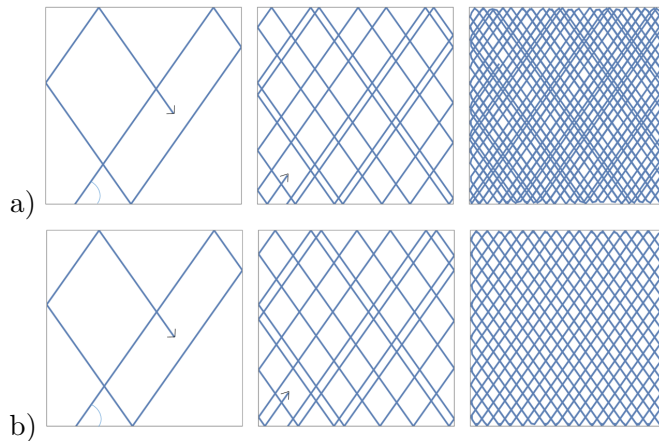


**Figure 3.5.:** Time evolution of a billiard ball with a) irrational and b) rational slope  $\alpha$ .

statement that the distribution error for the mentioned sets is zero.

In addition, we will show, that the condition on the slope cannot simply be omitted.

These theorems are true for almost all  $\alpha$  and we will show, that it cannot be generalized *for all*. In both cases we will explicitly present test-sets  $S$  that are not bounded remainders although the initial slope is irrational.

Fig. 3.4 illustrates three examples of a billiard path with rational initial slope. The curve spends no time in the subset  $S$  and hence the distribution error tends to infinity, if the time  $T$  goes to infinity. In the next example (Fig. 3.5), we show the evolution of two billiard paths, that distinguish only in a slightly different initial angle: The first one is irrational, the second one is rational.

At the beginning the plots seem to be equal, however, after some time the first differences can be identified .

#### Unfolding technique

A billiard path inside a unit-square can be unfolded to a straight line in the entire plane (see Fig. 3.6). The concept is simple: each time when the trajectory of the billiard path hits a boundary, the square itself is reflected to the corresponding side, so that the piecewise continuous billiard path becomes a straight line. In other words, the problem of the distribution of a billiard path in the unit square is equivalent to the distribution of the respective continuous rotation in the

### 3. SETS OF BOUNDED REMAINDER FOR THE BILLIARD ON A SQUARE

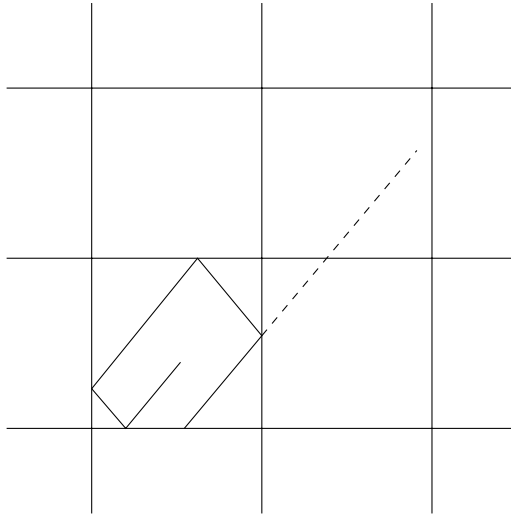


**Figure 3.6.:** Unfolding technique transforms the billiard path to a continuous rotation.

$2 \times 2$ -square.

A paper by D. König and Szüs from 1913 introduces first this geometric trick of the unfolding technique and it was reviewed recently again in [74].

The unfolding procedure is described in more detail here:

We define a new domain  $Q = [0, 2] \times [0, 2]$  that consists of four unit squares:  $Q_1, Q_2, Q_3, Q_4 \in [0, 1] \times [0, 1]$ .  $Q_1$  describes the original square, where we observe the billiard path.  $Q_2, Q_3, Q_4$  describes its reflections, s.t.:

$$Q_2 = \begin{pmatrix} -1 & 0 \\ 0 & 1 \end{pmatrix} \cdot Q_1, \quad Q_3 = \begin{pmatrix} -1 & 0 \\ 0 & -1 \end{pmatrix} \cdot Q_1, \quad Q_4 = \begin{pmatrix} 1 & 0 \\ 0 & -1 \end{pmatrix} \cdot Q_1$$

We arrange these squares  $Q_i$  now in the following order:  $Q = \begin{pmatrix} Q_4 & Q_3 \\ Q_1 & Q_2 \end{pmatrix}$

Summing up, all these squares describe the same billiard path in different views. We will follow the curve now in one of these squares - depending on its slope in the original square  $Q_1$ .

$(x, y)$  describe the x and y coordinate of the billiard path  $X(t)$ .

$R(t)$  describes a new curve:

$$R(t) := \begin{cases} X(t) \text{ in } Q_1 & \text{for } \frac{dx}{dt} > 0 \wedge \frac{dy}{dt} > 0 \\ X(t) \text{ in } Q_2 & \text{for } \frac{dx}{dt} < 0 \wedge \frac{dy}{dt} > 0 \\ X(t) \text{ in } Q_3 & \text{for } \frac{dx}{dt} < 0 \wedge \frac{dy}{dt} < 0 \\ X(t) \text{ in } Q_4 & \text{for } \frac{dx}{dt} > 0 \wedge \frac{dy}{dt} < 0 \end{cases} \quad \text{for } 0 \leq t \leq T$$

$R(t)$  describes a continuous rotation on the  $[0, 2] \times [0, 2]$  square, since:

1. The **direction vector** of the curve  $R(t)$  is always pointing to the right side and up. In other words, it is equal to the one, which is characterized by the initial angle.

Let us concretely validate this statement for  $Q_2$ :

### 3.2. SUMMARY OF PAPER AND AN EXPANDED DETAILED PROOF DESCRIPTION

$$R(t) = \begin{pmatrix} -1 & 0 \\ 0 & 1 \end{pmatrix} \cdot \underbrace{\begin{pmatrix} 1 - \{x\} \\ \{y\} \end{pmatrix}}_{X(t) \text{ in } Q_1} = \begin{pmatrix} -1 + \{x\} \\ \{y\} \end{pmatrix} \Leftrightarrow \begin{pmatrix} \{x\} \\ \{y\} \end{pmatrix}$$

It can be shown in the same way, that the slope of  $R(t)$  in  $Q_3$  and  $Q_4$  is equal to  $\begin{pmatrix} \{x\} \\ \{y\} \end{pmatrix}$

2. The **discontinuity points** of  $R(t)$  represent the jumps from a continuous rotation. It only remains to show, that the reflection is always in the right square: When  $R(t)$  hits the boundary  $\partial Q$ , then this results in a change of the sign of a derivative, e.g.: When  $R(t)$  hits the right boundary then the sign of the x-derivative of the billiard path  $X(t)$  changes from negative to positive. The slope of  $X(t)$  in the vertical direction remains the same. This means that the curve  $R(t)$  in  $Q_2$  will be continued in  $Q_1$  and  $Q_3$  in  $Q_4$ . The same considerations can be done for the upper boundary, which implies a change in the y-derivative. A bounce at the upper boundary of  $Q_1$  and  $Q_2$  results in the continuation of the curve in  $Q_4$  and  $Q_2$  respectively.

The next step is to shrink the domain  $Q$  to a unit square. This is observed by  $Q \mapsto \delta Q = \{\delta x : x \in Q\}$ , where  $\delta = \frac{1}{2}$ . It is easily feasible since the Lebesgue measure is linear and invariant to reflection.

( $n = 2$  describes the dimension of the domain)

$$\lambda(S) = \lambda(\bigcup S_i) = \lambda(S_1) + \lambda(S_2) + \lambda(S_3) + \lambda(S_4) = 4 \cdot \lambda(S_1) \quad (3.22)$$

$$\lambda\left(\frac{1}{\delta}S\right) = \left|\frac{1}{\delta}\right|^n \cdot 4 \cdot \lambda(S_1) = \lambda(S_1) \quad (3.23)$$

Moreover it holds that, the time that the curve  $\delta R(t)$  remains in the set  $S$  is the same as for  $X(t)$  in  $S_1$ , since we are only reflecting the original domain:

$$\forall t \in [0, T] : \delta R(t) \in \delta S \Leftrightarrow X(t) \in S_1 \quad (3.24)$$

When the distribution error  $\Delta_T$  of the continuous irrational rotation  $R(t)$  is bounded then the same holds for the billiard since the finite sum of finite elements is finite:

$$\Delta_T(X(t), S_1) = \left| \int_0^T \chi_{S_1}(X(t)) dt - T \cdot \lambda(S_1) \right| = \left| \int_0^T \chi_{\delta S}(\delta R(t)) dt - T \cdot \lambda(\delta S) \right| \quad (3.25)$$

$$= \Delta_T(\delta R(t), \delta S) \quad (3.26)$$

#### Continued fraction

The sometimes tiny difference between rational and irrational numbers can have a great impact on the results, as we have seen in Fig. 3.5. The billiard path for example is periodic only if the initial slope is rational. In the field of uniform distribution, irrational numbers are preferred, however

### 3. SETS OF BOUNDED REMAINDER FOR THE BILLIARD ON A SQUARE

diamonds on the other hand are thanks to their symmetric periodic structure of their fractals so beautiful.

Continued fractions present an interesting and powerful tool to approximate irrational numbers by rational numbers, that will appear as a main technique in the following proofs. The principal is briefly reviewed here [75]:

**Definition 3.14** (Continued fraction). *Let  $\alpha \in \mathbb{R}$ , then there exist a unique set of numbers  $a_i \in \mathbb{N} = [a_0; a_1, a_2, a_3, \dots]$ , where  $a_0 \in \mathbb{Z}$  and  $a_i \in \mathbb{N}$  for  $i > 0$ , such that*

$$\alpha = a_0 + \frac{1}{a_1 + \frac{1}{a_2 + \frac{1}{a_3 + \dots}}} \quad (3.27)$$

The  $a_i$  are calculated by the Euclidean Algorithm.

**Proposition 3.15.** *If  $\alpha$  is rational, then the continued fraction expansion of Eq. (3.27) is finite.*

**Definition 3.16** (Diophantine approximation). *The truncated continued fraction  $\frac{p_n}{q_n}$*

$$\alpha = a_0 + \overbrace{\frac{1}{a_1 + \dots + \frac{1}{\underbrace{a_n}_{:= \frac{p_n}{q_n}}}}}^{+ \dots} \quad (3.28)$$

is as close as possible to  $\alpha$ , meaning that there exist no better approximation  $\frac{p'}{q'}$  with  $0 \leq q' \leq q_n$ .

**Proposition 3.17.** *An estimate for the approximation error is given by:*

$$|\alpha - \frac{p_n}{q_n}| < \frac{1}{q_n^2 \cdot a_{n+1}} \quad (3.29)$$

The truncation index  $n$  indicates the degree of accuracy. The larger  $n$ , the closer is  $\alpha$  to  $\frac{p_n}{q_n}$ . It holds, that convergents with odd indices are larger than  $\alpha$  and those with even indices are smaller.

**Example 1.** For  $\alpha$  being rational:

$$\alpha = \frac{5}{7} = \frac{1}{1 + \frac{1}{2 + \frac{1}{2}}} \quad (3.30)$$

The continued fraction expansion can be periodic for irrational numbers:

$$\begin{aligned} \alpha &= \sqrt{2} = [1; 2, 2, 2, 2, \dots] \\ \alpha &= \sqrt{42} = [6; 2, 12, 2, 12, \dots] \end{aligned}$$

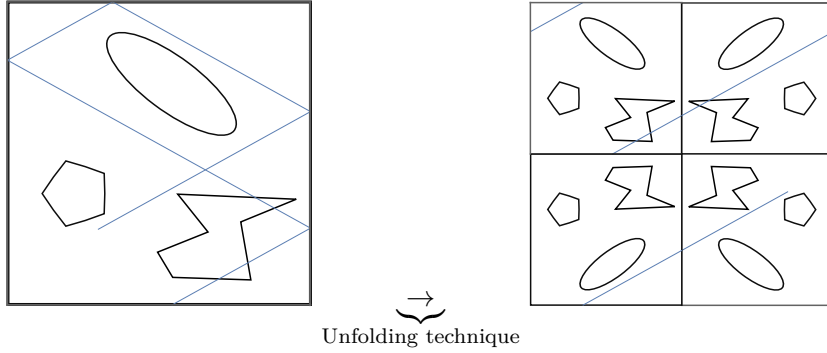


**Figure 3.7.:** Polygons and convex sets present BRS for the billiard path with irrational slope.

### 3.2.1. BRS for the billiard in a square

The first achievement of the paper is to improve the convergence rate on the distribution error for a specific class of sets (every polygon, every convex set) for almost all billiard paths with an irrational slope . The theorem is revised here:

**Theorem 3.18.**

1. *For almost all  $\alpha > 0$  and every  $\mathbf{x} \in I^2$ , every polygon  $S \subset I^2$  with no edge of slope  $\alpha$  or  $-\alpha$  is a bounded remainder set for the two-dimensional billiard with starting slope  $\alpha$  and starting point  $\mathbf{x}$ .*
2. *For almost all  $\alpha > 0$  and every  $\mathbf{x} = (x_1, x_2) \in I^2$ , every convex set  $S \subset I^2$  whose boundary  $\partial S$  is a twice continuously differentiable curve with positive curvature at every point is a bounded remainder set for the two-dimensional billiard with starting slope  $\alpha$  and starting point  $\mathbf{x}$ .*

To prove that  $S$  is a set of bounded remainder, we have to show that the distribution error is bounded:

$$S \in \bar{S} \Leftrightarrow \limsup_{T \rightarrow \infty} \Delta_T < \infty \quad (3.31)$$

In a related paper [76], it was shown that exactly these sets are of bounded remainder for the continuous rotation. The derivation of the same statement to hold for the billiard path can be observed and verified with the unfolding of the billiard path to the continuous rotation (Fig. 3.7).

### 3.2.2. Exceptions: Not BRS for the billiard in a square

The statement of Theorem 3.18 is only true for almost all  $\alpha$ . We were wondering therefore, if it could be extended firstly for all polygons and secondly to hold for all irrational slopes  $\alpha$ , instead of almost all. However, we found out, that by an explicit construction of  $\alpha$  the distribution error diverges in the sense that there exist polygons with slope  $\alpha$  and disks that are not bounded remainder sets for the billiard path, despite of its irrational initial direction. Consequently the

### 3. SETS OF BOUNDED REMAINDER FOR THE BILLIARD ON A SQUARE

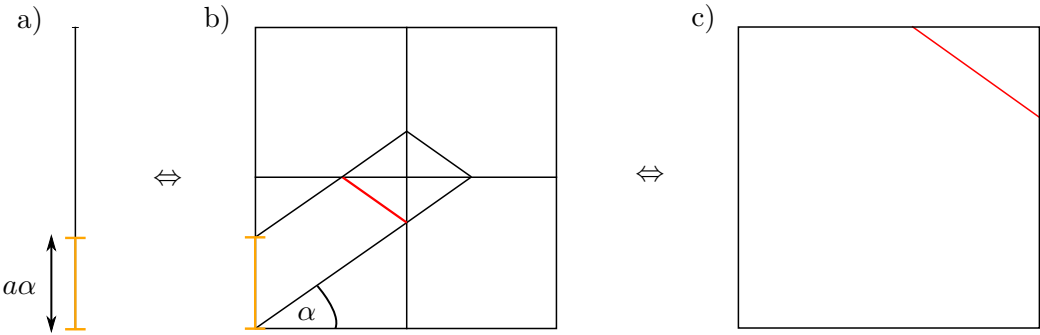


**Figure 3.8.:** Analogy of the distribution characteristics in the framework of a) a point set, b) the torus line and c) the billiard path.

Theorem 3.18 can not be improved to be valid for all directions, only for almost all. The theorem containing this negative result, states:

**Theorem 3.19.**

1. *For every  $\alpha > 0$  there is a polygon  $S$  with an edge of slope  $\alpha$  or  $-\alpha$  such that  $S$  is not a bounded remainder set for the billiard with starting-slope  $\alpha$  and for any starting point  $x$ .*
2. *For every  $m \in [0, 1]^2$  there are uncountably many radii  $r$ , dense in an interval of positive length, such that there is a slope  $\alpha$  and a starting point  $x$  such that the disk with midpoint  $m$  and radius  $r$  is not a set of bounded remainder with respect to the billiard with starting slope  $\alpha$  and starting point  $x$ .*

The proof of the first part of this Theorem goes back to a proof shown by Kesten [73] for a one-dimensional sequence. He showed, that the distribution error of the Kronecker sequence with an irrational  $\alpha$  and an interval of length  $a\alpha \neq \{k\alpha\}$  is unbounded, and analogously this negative result holds for the billiard path (compare Fig. 3.8).

To prove the second part of the Theorem requires a bit more work. Again we derive the statement by adopting the proof of the continuous rotation of the equivalent Theorem in [76]. The idea in [76] is to approximate  $\alpha$  with a continued fraction  $\frac{p}{q}$ . We know already that the distribution error converges for rational slopes. The idea is therefore to approximate  $\alpha$  up to a carefully chosen error to  $|\alpha - \frac{p}{q}|$  (compare size of the squares in Fig. 3.10), for which the distribution error (with support of further error bounds, and techniques of number theory) finally diverges.

The summarized constraints on  $\alpha$  for the torus line are the following:

- $\alpha \in [\frac{1}{4}, \frac{1}{2}]$ .
- Every irrational  $\alpha$  can be approximated by a rational  $\frac{p_l}{q_l}$  determined by its continued fraction expansion of  $\alpha = [0; a_1, a_2, a_3, \dots, a_l, a_{l+1}, \dots]$ , we demand  $a_{l+1} > q_l^{100}$ .
- The index  $l$  is odd, this means that  $\frac{p_l}{q_l} > \alpha$ .

### 3.2. SUMMARY OF PAPER AND AN EXPANDED DETAILED PROOF DESCRIPTION

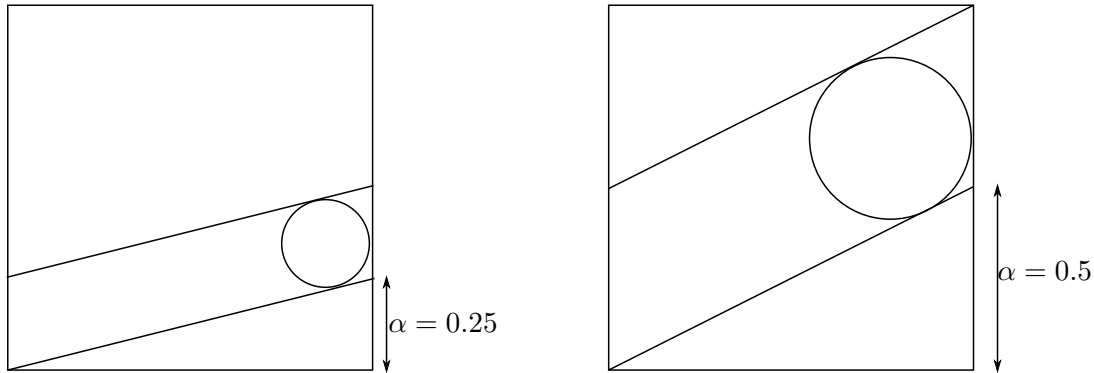


**Figure 3.9.:** Size of the disks for the irrational rotation.

- The numerator  $p_l = 2m$  is even ( $m \in \mathbb{N}$ ).

One can show that there are uncountably many  $\alpha$ , that fulfil these requirements.

The diameter of the disk is defined by a term depending on  $\alpha$ . The possible size of the disk is illustrated in Fig. 3.9. The same negative statement to hold for the billiard path, can not straightforwardly be derived due to two reasons:

- There exist disks for the torus line that can not be transformed to equivalent sets for the billiard path.
- The transformation to the billiard path reveals four disks. It has to be guaranteed that at least one of them has the size and the position of the disk for the torus line. In addition, it has to be proven that the distribution errors of the four equivalent sets do not cancel themselves out.

The mapping from the torus line to the billiard path requires some stricter error estimates (shown in several Lemma and Propositions of the related paper [2]), that are mainly related to the two considerations from above.

Fig. 3.10 illustrates the construction of the intervals of positive measure that finally defines those sets that are not of bounded remainder. The paper [2] describes the full proof.

### 3. SETS OF BOUNDED REMAINDER FOR THE BILLIARD ON A SQUARE

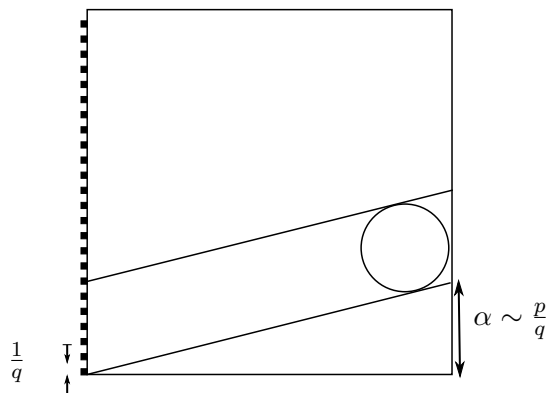


**Figure 3.10.:** Ray of the disks has to start in one of the black squares.



# CHAPTER 4

---

## Distribution Properties of Quasi Energy Spectra in Quantum Mechanics

---

Random matrix theory is of particular interest to classify quantum systems according to physical properties [13, 77, 78]. The underlying paper [3] of this chapter analyses mathematical sequences  $(\theta_n)_{n \geq 1}$  that are used to describe the energy levels of integrable quantum systems. The behaviour of these sequences provide then an indication of the type of motion of the quantum system. We start with a short introduction to quantum mechanics, that hence introduce straightforwardly the importance of the energy levels of a quantum system and continue with a mathematical analysis of the required properties of a sequence  $(\theta_n)_{n \geq 1}$ .

### 4.1. Introduction to Quantum Mechanics

*“At first I found particle physics very cold. But then when you look at it from the mathematical perspective and you realize the incredible connection there is between mathematics and the structure of the universe, well that gave it an incredible appeal.”*

Michelangelo Mangano (theoretical physicist at CERN) [79]

Quantum mechanics (QM) exists now for more than 70 years and has probably become the best tested physical theory ever concieved. It describes the behaviour of particles on the atomic scale, and the behaviour that light causes when it hits these particles. Completely different laws are valid in this domain. For example energy, momentum and other quantities are often restricted to discrete values (quantization). Objects have characteristics of both particles and waves (wave-particle duality) and there are limits to the precision with which quantities can be known (uncertainty principle). In the classical limit <sup>1</sup>, the correspondence principle states that QM continuously develops into classical mechanics.

---

<sup>1</sup>Planck’s constant  $\hbar = 1.0545718 \times 10^{-34} m^2 kg/s$  vanishes.

#### 4.1. INTRODUCTION TO QUANTUM MECHANICS

QM is formulated in special developed mathematical formalism based on fundamental axioms and equilibrium equations. Only by studying theoretical implications and using mathematical transformations, particle physicist are able to derive astonishing results about the behaviour of particles. The theoretical existence of a Higgs boson for instance was already announced in the 1960s. Fifty years later, on the 4th of July of 2012 the two experiments ATLAS and CMS, the two main experiments at CERN in the LHC, could for the first time confirm its experimental observation.

The most relevant equation in QM is the energy conservation in the form of Schrödinger's equation:

$$i\hbar \frac{\partial \psi}{\partial t} = \mathcal{H}\psi, \quad (4.1)$$

where  $\mathcal{H}$  is the Hamiltonian operator that describes the total energy (kinetic+potential), and  $\psi$  is a wave function, that provides information about the probability amplitude of position, momentum and other physical properties of a particle. If  $\mathcal{H}$  does not explicitly depend on time, then we can use a separation approach of time and space to solve Eq. (4.1). The energy of the system describes in this case a constant of motion, that can only assume certain discrete values  $E_n$ , presented by the eigenvalues of  $\mathcal{H}$ .

$$\mathcal{H}\psi_n = E_n\psi_n \quad (4.2)$$

with this specific form of the wave function:

$$\psi_n(x, t) = \psi_n(x) \exp\left(\frac{i}{\hbar}E_n t\right) \quad (4.3)$$

In words the equation (4.2) states:

When the Hamiltonian operator acts on a certain wave function  $\psi$ , and the result is proportional to the same wave function  $\psi$ , then  $\psi$  is a stationary state, and the proportionality constant,  $E_n$ , is the eigenenergy of the state  $\psi$ .

A transformation of Schrödinger's equation to a matrix representation, by expressing the eigenfunctions  $\psi_n(x)$  to

$$\psi_n(x) = \sum_m a_{nm} \Phi_m(x), \quad (4.4)$$

where  $\Phi_m(x)$  are arbitrary, but orthogonal and leads to the matrix representation of the stationary Schrödinger equation

$$\sum_m H_{nm} a_m = E_n a_n \quad (4.5)$$

The Hamiltonian of many quantum systems is not known and very difficult to set up. An ensemble

#### 4. DISTRIBUTION PROPERTIES OF QUASI ENERGY SPECTRA IN QUANTUM MECHANICS

of random matrices assuming certain statistical properties (e.g. Poissonian property) is instead frequently used to describe the Hamiltonian. Examples of frequently discussed quantum systems are:

- harmonic oscillator
- particle in a box
- excitation of a hydrogen atom

further described in Section 4.4.

### 4.2. Distribution of eigen-energy levels in integrable quantum systems

Berry and Tabor showed in a frequently cited paper of the Proceedings of the Royal Society of London A [14], that the energy levels  $E_n$  are uncorrelated and Poisson distributed for nearly all integrable systems.

**Definition 4.1** (Poisson distribution). *A Poisson distribution is a discrete probability distribution that expresses the probability of finding a given number of  $k$  events in a fixed interval of space. These events occur with a known average rate  $\lambda$  and independently of the time since the last event occurred [80]. The probability of observing  $k$  events in an interval is given by:*

$$\mathcal{P}(k \text{ events in interval}) = e^{-\lambda} \lambda^k / k! \quad (4.6)$$

for  $k \in \{0, 1, 2, \dots\}$  and  $\lambda \in \mathbb{R}$  is the average number of events per interval. An event describes in this context the locating of an energy level in the interval.

The spacing  $p(s)$  in between Poisson distributed eigenvalues is exponential distributed.  $p(s)$  is called the nearest neighbour spacing function, and the probability of the distance  $s$  of adjacent eigenvalues is expressed in the following equation:

$$p(s) = \exp(-s), \quad (4.7)$$

where  $s$  describes the distance between the energy levels (see also Fig. 4.1).

Figure 4.2 shows experimental results of the nearest neighbour spacing distribution of a particle in a box, studied by Casati [81] and it looks fairly close to the Poisson distribution of the corresponding energy levels.

Concluding, this experimental result (Fig. 4.2) confesses, that the energy level distribution, and consequently the nearest neighbour spacing levels for a particle in a box behave more or less like a sequence of random numbers. The harmonic oscillator on the other hand, presents an exception. The eigenvalues of the harmonic oscillator form an equidistant sequence, which obviously does not

### 4.3. MATHEMATICAL ASPECTS OF THE NEAREST NEIGHBOUR SPACING PROBLEM

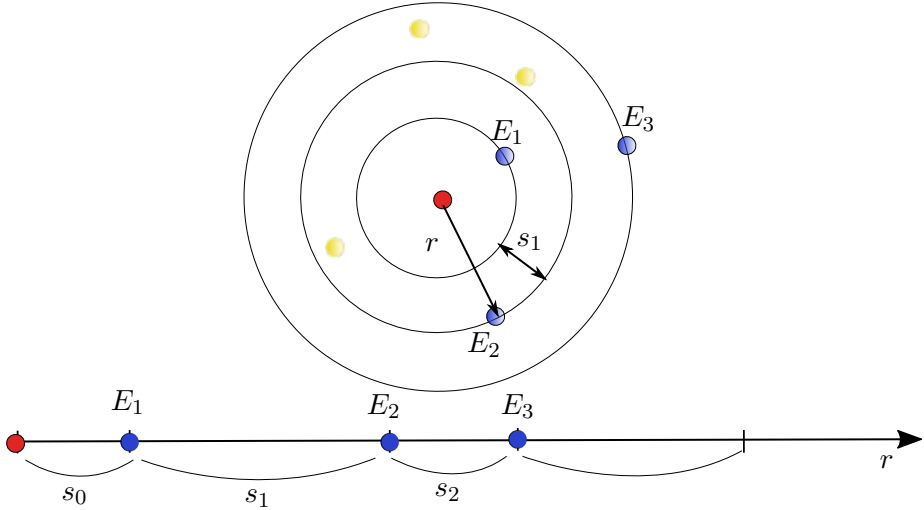


**Figure 4.1.:** Nuclear scattering of a hydrogen atom: The probability of finding  $k$  energy levels in a distance of radius  $r$  from the origin is expressed by a Poisson distribution. The spacings in between follow an exponential distribution. The yellow dots describe instable and hence not measurable energy states.

obey a Poisson level spacing distribution. Soon further exceptions to the behaviour predicted by Berry and Tabor for integrable systems were found. A lot of attention is therefore focused on the analysis of sequences that describe integrable quantum systems on whether or not they obey the Poissonian property. We were investigating this issue in the paper [3] to formulate a general statement, when a mathematical sequence obeys the Poissonian property and when not.

### 4.3. Mathematical aspects of the nearest neighbour spacing problem

We revise the distribution of the nearest neighbour spacing of quantum system with studying the pair correlation of sequences. The pair correlation function  $R_2(s)$  of a sequence, describes how the density of its elements vary as a function of distance between the elements.

**Definition 4.2** (Pair correlations). *Let  $[-s, s]$  be an interval in  $[0, 1)$ , let  $(\theta_n)_{n \geq 1}$  be a sequence modulo one and let  $N$  be a truncation index of the sequence:*

$$R_2([-s, s], (\theta_n)_{n \geq 1}, N) = \frac{1}{N} \# \left\{ 1 \leq j \neq k \leq N : \|\theta_j - \theta_k\| \leq \frac{s}{N} \right\}.$$

Note, the index of  $R_2$  only gives an additional hint, that we are analysing properties between two elements of a sequence.

$\rho = \frac{s}{N}$  is the average number density of particles, in the interval  $[0, s]$ .

**Definition 4.3.** *We say that the distribution of the pair correlations of a certain sequence is*

#### 4. DISTRIBUTION PROPERTIES OF QUASI ENERGY SPECTRA IN QUANTUM MECHANICS

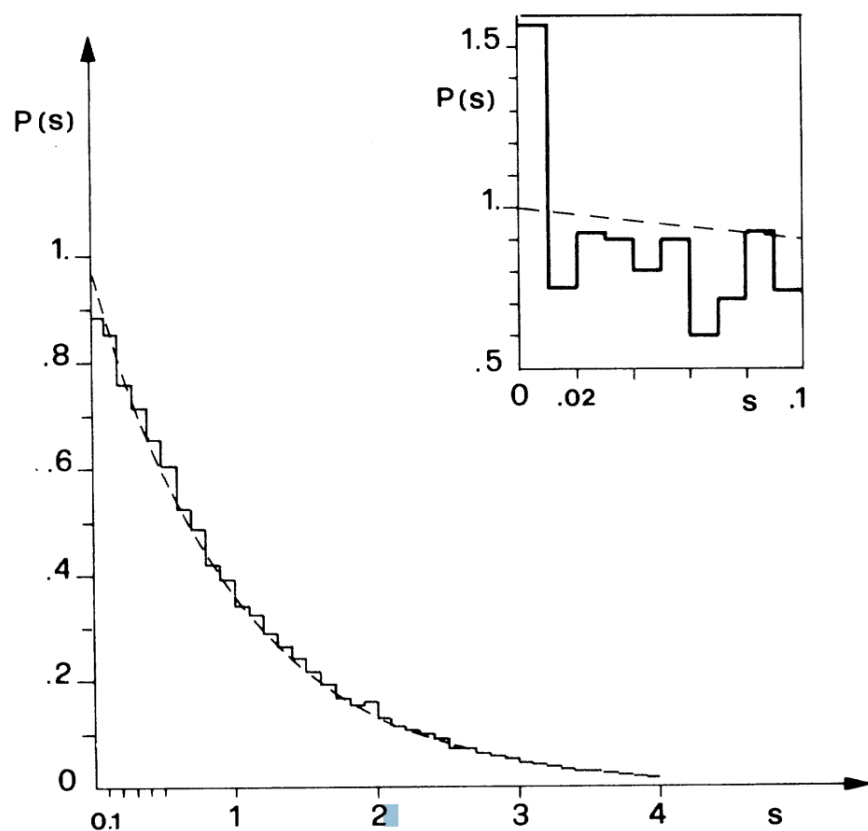


**Figure 4.2.:** Level-spacing distribution, comparison of experimental analysis and the Poisson distribution (dashed line), for the insert see the text to the source: [81].

*asymptotically Poissonian, when*

$$R_2([-s, s], (\theta_n)_{n \geq 1}, N) \rightarrow 2s. \quad (4.8)$$

**Proposition 4.4.** *Any random distribution fulfils this property with  $\mathbb{P} = 1$ .*

**Example 2** (to make heuristically clear Prop. 4.4). We assume a uniformly distributed random sequence  $(\theta_n)_{n \geq 1}$  in the unit interval (see Fig. 4.3), that is truncated after  $N$  elements. The total number of pair correlations is described with the number of possible combinations of  $N$  elements, subtracting the identical tuples, which yields  $N^2 - N \sim \mathcal{O}(N^2)$  spacings. Consider now for instance an interval  $[-s, s] = [-\frac{1}{4}, \frac{1}{4}]$ . The number of elements  $\theta_i$ , that find a  $\theta_j$  within a distance of  $\frac{1}{2}$ , has to be approximately half of all possible combinations for a uniformly distributed sequence. For the general interval  $[-s, s]$  we assume therefore  $2s \cdot N^2$ .

When we now normalize the upper bound of the spacing by  $\frac{s}{N}$  and divide the result by  $N$ , then we end up with the definition of the pair correlation and its expected value of  $2s$  in the limit.

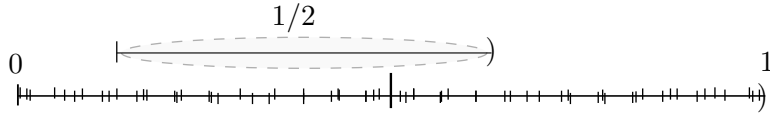


**Figure 4.3.:** Distribution of a sequence  $\theta$  in the unit interval; interval for pair correlations found in  $[-\frac{1}{4}, \frac{1}{4}]$ .

**Remark 4.5.** *Informally speaking, a sequence that obeys the Poissonian property may be seen as a sequence showing random behaviour. The investigation of sequences that have this property is equivalent to studying the pseudo-randomness properties of sequences. This provides a strong link to the current SFB-project at the JKU of "Quasi-Monte Carlo Methods: Theory and Applications" [82].*

With regard to the classification of quantum systems, we analyse first the energy spectrum of the harmonic oscillator and then the particle in a box.

### 4.3.1. Pair correlation statistics for certain sequences

In the following, we analyse the pair correlation statistics of certain sequences. We will see, that the energy spectrum for the harmonic oscillator does not obey the asymptotically Poissonian property whereas it does for the particle in the box. The energy level distribution in case of the harmonic oscillator (see Eq. 4.18 later) is equivalently described with the Kronecker sequence.

**Definition 4.6** (Kronecker sequence).

$$\begin{aligned} (\theta_n)_{n \geq 1} &= (\{n\alpha\})_{n \geq 1} \text{ with } \alpha \in \mathbb{R} \setminus \mathbb{Q}, \\ \text{or equivalently: } \theta_n &= \{(n-1) \cdot \alpha + \theta_1\} \end{aligned}$$

#### 4. DISTRIBUTION PROPERTIES OF QUASI ENERGY SPECTRA IN QUANTUM MECHANICS

If  $\alpha$  describes a rational number, then the sequence is periodic and obviously does not obey the Poissonian property. In the case that  $\alpha$  is irrational, Weyl showed already in 1916 that the Kronecker sequence is uniformly distributed; a proof is for example written in [11, 72]. Hence we are interested if uniform-distribution is already a sufficient statistical property for a sequence to obey the Poissonian property. Fig. 4.4 illustrates the Kronecker sequence on the unit circle. For  $\alpha \in \mathbb{R} \setminus \mathbb{Q}$  and for  $N$  large, the elements of the sequence  $\theta$  cover the whole unit ring. Hence, first consideration, may let us guess, that this sequence is asymptotically Poissonian distributed.

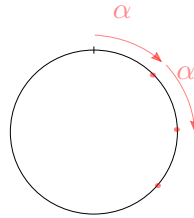


**Figure 4.4.:** Kronecker sequence on the unit circle.

**Theorem 4.7.** *The energy levels of the harmonic oscillator and hence the Kronecker sequence do not obey the asymptotically Poissonian property for any value of  $\alpha$ .*

*Sketch of proof.* The idea is to approach  $\alpha$  with the continued fraction  $\frac{p}{q}$  (see also Section 3.2) with an error approximation of

$$|\alpha - \frac{p}{q}| < \frac{1}{q^2}$$

Without loss of generality, we set the truncation index  $N = q$ .

It holds, that:

$$\left( \left\{ \frac{n \cdot p}{q} \right\} \right)_{n=1,\dots,q} = \left( \frac{n \cdot p(\text{mod } q)}{q} \right)_{n=1,\dots,q}$$

Following, it is true that:

$$(\{n\alpha\})_{n=1,\dots,q} \approx \left( \frac{1}{q}, \frac{2}{q}, \dots, \frac{q-1}{q} \right)$$

Hence, we can choose an interval  $[-s, s]$  with length:  $\frac{1}{q} - \frac{2}{q^2}$  (see Fig. 4.5), so that:

$$R_2 = 0 \neq 2s.$$

An extended remark to the proof can be found in [83] with a hint to the well-known *Three-Distance Theorem*.  $\square$

The other way round is true. A sequence that has the asymptotically Poissonian property is also uniformly distributed. This statement was shown recently by Grepstadt and Larcher in [84].

### 4.3. MATHEMATICAL ASPECTS OF THE NEAREST NEIGHBOUR SPACING PROBLEM

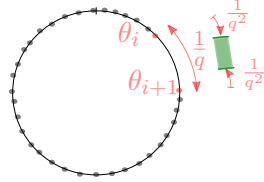


**Figure 4.5.:** Specific selection of interval  $[-s, s]$  on the unit circle for the sequence.

Therefore, we can conclude:

**Lemma 4.8.** *A uniform distributed sequence in general does not imply to have the asymptotically Poissonian property, whereas an asymptotically Poissonian sequence  $(\theta_n)_{n \geq 1}$  obeys the uniform distribution:*

$$\text{Uniform} \quad \not\Rightarrow \quad \text{Poissonian} \quad (4.9)$$

$$\text{Poissonian} \quad \underbrace{\Rightarrow}_{\text{Grepstad+Larcher, 2017}} \quad \text{Uniform} \quad (4.10)$$

Further sequences have already been studied whether or not they have the Poissonian property. The following table should give a brief overview of the current state of the art.

**Table 4.1.:** Survey of studied sequences in literature wrt the Poissonian property.

Sequence $(\theta_n)_{n \geq 1}$	Comments	Poissonian property	References
$(\{n\alpha\})_{n \geq 1}$	harmonic oscillator	No	[83]
$(\{n^2\alpha\})_{n \geq 1}$	particle in a box	for almost all $\alpha$	[83]
$(\{n^d\alpha\})_{n \geq 1}$	for $d \geq 2$	for almost all $\alpha$	[85–88]
$(\{a(n)\alpha\})_{n \geq 1}$	$a(x) \in \mathbb{Z}[x]$ and $\deg(a(x)) \geq 2$	for almost all $\alpha$	[89]
$(\{a(n)\alpha\})_{n \geq 1}$	$a(n)$ is a lacunary sequence	for almost all $\alpha$	[90–92]

**Example 3** (Lacunary sequence). A Lacunary sequence is a sequence of numbers  $(\theta_n)_{n \geq 1}$  such that

$$\forall n > n_0 \exists \delta > 0 : \frac{a(n+1)}{a(n)} \geq 1 + \delta.$$

The sequence  $a(n) = 2^n$  is a lacunary sequence and hence

$$(\{2^n\alpha\})_{n \geq 1}$$

is Poissonian for almost all  $\alpha$ .

## 4. DISTRIBUTION PROPERTIES OF QUASI ENERGY SPECTRA IN QUANTUM MECHANICS

### 4.3.2. Conditions for a sequence to have the asymptotical Poissonian property

This subsection investigates under which conditions a sequence in the general form  $(\{a(n)\alpha\})_{n \geq 1}$  obeys the Poissonian property. Table 4.1 introduced already two subclasses ( $a(n)$  being integer polynomials, or a lacunary sequence) for which the assertion is true.

The concept of the additive energy of the coefficients  $(a(n))_{n \geq 1}$  will be introduced and it will provide in Theorem (4.10) a link between

- distribution of pair correlations of  $(\{a(n)\alpha\})_{n \geq 1}$  and
- the additive energy of the truncations of the integer sequence  $(a(n))_{n \geq 1}$ .

The additive energy, see for example the book about additive combinatorics in [93], is defined as :

**Definition 4.9** (additive energy).

$$E(A) := \sum_{a+b=c+d} 1,$$

with  $(a, b, c, d) \in A$

The lower and upper limits of the additive energy of the truncated sequence  $A_n$  are given by

$$|A|^2 \leq E(A) \leq |A|^3$$

since for the lower bound, we can always

$$\left. \begin{array}{l} \text{choose } a_i \text{ and set } a_k = a_i \\ \text{choose } a_j \text{ and set } a_l = a_j \end{array} \right\} \Rightarrow \text{at least } N^2$$

This implies at least  $N^2$  possible combinations of the sequence elements.

For the upper bound, we can:

$$\text{choose } a_i, a_j, a_k \text{ and set } a_l = -a_i - a_j - a_k \Rightarrow \text{at most } N^3.$$

The above defined  $a_l$  may not exist, hence we observe maximal  $N^3$  possible tuples.

**Example 4** (Additive energy). A sequence with a "high" energy is

$$(n)_{n \geq 1} = 1, 2, 3, \dots, N$$

There are approximately  $c \cdot N^3$  tuples that satisfy:

$$a_i + a_j = a_k + a_l \Leftrightarrow i + j = k + l$$

### 4.3. MATHEMATICAL ASPECTS OF THE NEAREST NEIGHBOUR SPACING PROBLEM

The following theorem provides a condition, when the sequence obeys the Poissonian property. It states that if the additive energy of the coefficient-sequence  $(a(n))_{n \geq 1}$  satisfies  $E(A_N) \ll N^{3-\varepsilon}$  for some  $\varepsilon > 0$ , then the sequence has asymptotical Poissonian pair correlations:

**Theorem 4.10.** *Let  $(a(n))_{n \geq 1}$  be a sequence of distinct integers, and suppose that there exists a fixed constant  $\varepsilon > 0$  such that*

$$E(A_N) \ll N^{3-\varepsilon} \quad \text{as } N \rightarrow \infty. \quad (4.11)$$

*Then for almost all  $\alpha$  one has*

$$R_2(s, \alpha, N) \rightarrow 2s \quad \text{as } N \rightarrow \infty \quad (4.12)$$

*for all  $s \geq 0$ .*

This theorem has been shown in [94].

Informally speaking, this result implies that nearly all sequences have asymptotically Poissonian pair correlations, since the condition (4.11) is very close to the trivial upper bound of the additive energy. We are therefore especially interested in which cases the sequence does not obey this property (as for instance harmonic oscillator). The following negative result has already been worked out by Bourgain in [94]. He states that if the additive energy is "high", then there always exists a set of  $\alpha$  of positive measure so that the sequence does not obey the Poissonian property. The classification of high energy has to be understood in the sense of the *Hardy-Littlewood* [95] definition.

**Definition 4.11.** *The asymptotic notation  $\Omega(g)$ , in the sense of Hardy-Littlewood, characterizes functions according to the growth rate of the function  $f(x)$  compared to  $g(x)$  when the argument tends towards infinity. We say that:*

$$f(x) = \Omega(g(x)) \quad \text{with } (x \rightarrow \infty) \Leftrightarrow \limsup_{x \rightarrow \infty} \left| \frac{f(x)}{g(x)} \right| > 0$$

The negative result of Bourgain states that:

**Theorem 4.12** (Bourgain). *If*

$$E(A_N) = \Omega(N^3), \quad (4.13)$$

*then there exists a subset of  $[0, 1]$  of positive measure such that for every  $\alpha$  from this set the pair correlations of the sequence  $(\{a(n)\alpha\})_{n \geq 1}$  are **not** asymptotically Poissonian.*

We investigated in this result and we will show a partial proof of the following much stronger conjecture:

#### 4. DISTRIBUTION PROPERTIES OF QUASI ENERGY SPECTRA IN QUANTUM MECHANICS

**Conjecture 4.13.** *If  $E(A_N) = \Omega(N^3)$  then the pair correlations of the sequence  $(\{a(n)\alpha\})_{n \geq 1}$  do **not** have the Poissonian property for almost all  $\alpha$ .*

The condition (4.13) implies a strong linear substructure of the sequence. The definition of a quasi-arithmetic sequence is revising all of those implied properties of a sequence and we use them to proof partially the concerning conjecture in the case of quasi-arithmetic sequences in dimension 1. The definition of a quasi-arithmetic sequence will also include a d-dimensional arithmetic progression, that we first introduce here:

**Definition 4.14** (d-dimensional arithmetic progression). *We call a sequence of integers a **d-dimensional arithmetic progression**, if it is constructed as an arithmetic progression, but allowing several possible differences:*

$$P_i := \left\{ b_i + \sum_{j=1}^d r_j k_j^{(i)} \middle| 0 \leq r_j < s_j^{(i)} \right\},$$

**Definition 4.15** (Quasi-arithmetic sequence of degree d). *A sequence  $(a(n))_{n \geq 1}$  is quasi arithmetic of degree  $d \in \mathbb{N}$ , if:*

- $(a(n))_{n \geq 1}$  is a strictly increasing integer sequence ↑
- $\exists (N_i)_{n \geq 1}$  strictly increasing sequence of truncation indices of positive integers
- $\exists C, K > 0$  constants
- $\forall N_i \exists$  sub-sequence  $A^{(i)} \subset (a(n))_{1 \leq n \leq N_i}$  with:
  - $|A^{(i)}| \geq CN_i$  (Condition that subsequence is not too small.)
  - $A^{(i)}$  is contained in a d-dimensional arithmetic progression  $P^{(i)}$
  - $|P^{(i)}| \leq KN_i$  (Condition that arithmetic progression is not arbitrary big.)

**Example 5** (Example of a quasi-arithmetic sequence of degree 1). Consider a strictly increasing sequence  $(a_i)_{i > 1}$ :

$$a(1) < a(2) < a(3) < \dots < a(N-1) < a(N)$$

then we look for a constant  $K$  and for indefinitely many truncation indices  $N$ , so that the following holds:

$$\frac{a(N)}{N} \leq K \tag{4.14}$$

For instance, only each truncated sequence of the following fulfils the requirement (4.14), starting with the first one:

- 1, 2, 3,  $\left| \dots \right.$  (yes)

- 1, 2, 3, 10.000,  $\left| \dots \right.$  (no)
- 1, 2, 3, 10.000, 10.001, 10.002,  $\dots$ , 20.000,  $\left| \dots \right.$  (yes)
- 1, 2, 3, 10.000, 10.001, 10.002,  $\dots$ , 20.000, 200 Mio., 200 Mio.+ 1,  $\dots$ ,  
 $\dots$ , 200Mio. + 300Mio.,  $\left| \dots \right.$  (no)

Two theorems, namely the statements of the "Balog–Szemerédi–Gowers-Theorem" and the "Theorem of Freiman" (can be looked up in [93]) imply that:

**Lemma 4.16.** *A sequence  $(a(n))_{n \geq 1}$  is quasi arithmetic of degree  $d$ , iff*

$$E(A_N) = \Omega(N^3).$$

We can therefore reformulate our statement to the following conjecture that we show for the case  $d = 1$ :

**Conjecture 4.17.** *The pair correlations of  $(\{a(n)\alpha\})_{x \geq 1}$  is **not Poissonian** for almost all  $\alpha$ , if  $(a(n))_{n \geq 1}$  is a quasi-arithmetic sequence.*

More precisely, we can formulate the following Theorem:

**Theorem 4.18.** *If the sequence of integers  $(a(n))_{n \geq 1}$  is quasi-arithmetic of degree 1, then the set of  $\alpha$ 's for which the distribution of the pair correlations of  $(\{a(n)\alpha\})_{n \geq 1}$  is not asymptotically Poissonian has full measure.*

The proof of this theorem is the main content of the paper [3]. Generally speaking, we can say that the proof is very technical. It uses a stronger version of a theorem of Cassels about diophantine approximations. However we refer the reader to study the whole proof in the context of the paper [3], that is listed in Part II of this thesis.

## 4.4. Examples of integrable quantum systems

We revise here three typical examples of quantum mechanics and derive to each of them the wave function and the corresponding energy spectra. For further details see any introductory book on quantum mechanics, as for example: [13, 96].

## 4. DISTRIBUTION PROPERTIES OF QUASI ENERGY SPECTRA IN QUANTUM MECHANICS

### 4.4.1. 1-dimensional harmonic oscillator

As an application of the Schrödinger equation, we now calculate the states of the particle in an oscillating potential.

The behaviour of many quantum systems near their equilibrium can be described by the harmonic oscillator. This assumption is motivated by the idea to expand a potential  $V(x)$  in a Taylor series. In the following we shall consider the one-dimensional case

$$V(x) = V(a + (x - a)) \quad (4.15)$$

$$= V(a) + V'(a)(x - a) + \frac{1}{2}V''(a)(x - a)^2 + \dots \quad (4.16)$$

If a stable equilibrium exists for  $x = a$ ,  $V(x)$  has a minimum at  $x = a$ , i.e.  $V'(a) = 0$  and  $V''(a) > 0$ . We can choose then  $a$  as the origin of the coordinate system and set  $V(a) = 0$ ; then an oscillator potential is indeed a first approximation in the vicinity of the equilibrium point.

The classical Hamiltonian function of a particle with mass  $m$  oscillating with frequency  $\omega$  takes the form:

$$H = \frac{p_x^2}{2m} + \frac{m}{2}\omega^2 x^2$$

and the corresponding quantum mechanical Hamiltonian reads

$$\hat{H} = \frac{\hbar^2}{2m} \frac{d^2}{dx^2} + \frac{m}{2}\omega^2 x^2.$$

Since the potential is constant in time, the time-independent (stationary) Schrödinger's equation determines the stationary solutions  $\psi_n$  and the corresponding eigenvalues (energies)  $E_n$ . The stationary Schrödinger equation takes the form:

$$\frac{\hbar^2}{2m} \frac{d^2}{dx^2} \psi(x) + \frac{m}{2}\omega^2 x^2 \psi(x) = E_n \psi(x). \quad (4.17)$$

A solution of (4.17) can be looked up in any introductory book of QM (see for example in [96]). Hint: Transform  $\psi$  to a hypergeometric function, by using the approach of  $\psi(\lambda x^2) = \exp(\frac{\lambda x^2}{2})\phi(\lambda x^2)$  with  $\lambda = \frac{m\omega}{\hbar}$  and further by expanding  $\phi$  into terms of a power series.

Finally, conditions for the break off of the hypergeometric series lead then to the *quantization of energy*.

$$E_n = \hbar\omega(n + \frac{1}{2}) = (2n + 1)\frac{\hbar}{2}\omega \text{ for } n = 0, 1, 2, \dots \quad (4.18)$$

As we see, the energy spectrum of the harmonic oscillator is equidistant with the spacing  $\hbar\omega$  and has finite value in the ground state ( $n = 0$ ), the *zero-point energy*  $\frac{1}{2}\hbar\omega$  (see Fig. 4.6). The zero-point energy is a direct consequence of the uncertainty relation. And eigenfunctions can be expressed

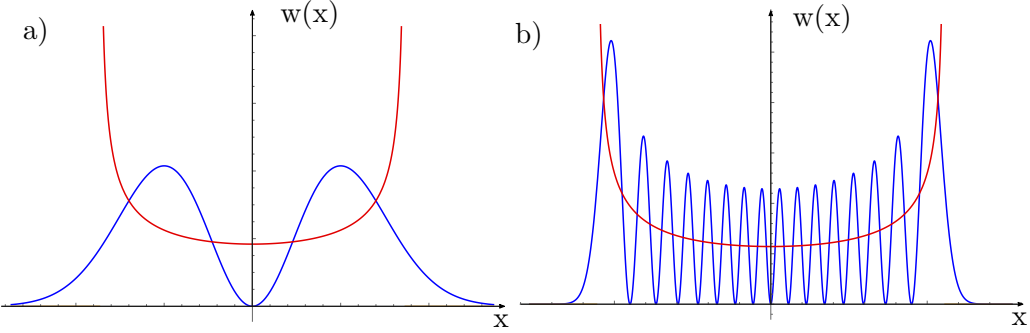


**Figure 4.6.:** Comparison of the probability density for finding a particle moving in an oscillator, classically (red line) and quantum-mechanically (blue line) with the energy corresponding to a)  $n = 1$  and in b)  $n = 15$ .

with the following:

$$\psi_n(x) = \frac{1}{\sqrt{2^n n!}} \cdot \frac{m\omega^{\frac{1}{4}}}{\pi\hbar} \cdot e^{-\frac{mwx^2}{2\hbar}} \cdot H_n(\sqrt{\frac{mw}{\hbar}}x)$$

with  $n = 0, 1, 2, \dots$  and  $H_n$  describes Hermite polynomials.

In Fig. 4.6, some of the  $\psi_n$  are plotted together with an energy diagram. The energy eigenvalues are represented as horizontal lines. For each of the lines there is a corresponding eigenfunction  $\psi_n(x)$  drawn on an arbitrary scale. In addition, the figure contains the function of the potential energy

$$V(x) = \frac{1}{2}m\omega^2x^2.$$

The agreement between classical and quantum probabilities improves with increasing  $n$  (quantum numbers), see Fig. 4.6. The mean value of the quantum distribution approximates the classical limit.

#### 4.4.2. Particle in a box

The wave-particle duality can be illustrated with the propagation of a point-like particle in a box with indefinitely high walls. These systems are called billiards. We give the example for a 1-dimensional box of length  $2a$ .

The potential  $V(x)$  assumes either the value  $-V_0$  inside the box, or zero outside out of the box. Schrödinger's equation in stationary state is given by:

$$-\frac{\hbar^2}{2m} \frac{d^2\phi}{dx^2} + V(x)\phi(x) = E\phi(x).$$

We see that the free field Schrödinger equation is the same as the Helmholtz equation, which represents a time-independent form of the wave equation:

$$(\nabla^2 + k^2)\psi = 0 \quad \text{with } k^2 = \frac{1}{\hbar^2} 2m(E + V_0)$$

## 4. DISTRIBUTION PROPERTIES OF QUASI ENERGY SPECTRA IN QUANTUM MECHANICS

The solution of this equation implies the following energy spectrum:

$$E_n = \frac{\hbar^2}{2m} \left( \frac{n\pi^2}{2a} - V_0 \right)$$

Enlarging the box or the mass of the particle causes a decrease between two neighbouring energy eigenvalues. Equivalent to the previous example, we observe a zero-point energy in the ground state  $n = 0$ .

### 4.4.3. The hydrogen atom

The example of the hydrogen atom discusses the motion of a single-particle system in a potential field. The following description chooses the proton to be the centre of the coordinate system and the use of spherical coordinates. The stationary Schrödinger equation is then:

$$\hat{H}\psi = E\psi = \left( \frac{\hat{p}^2}{2m} - \frac{e^2}{r} \right) \psi,$$

with  $\hat{p}$  being the momentum operator,  $m$  the reduced mass of the electron,  $e$  the elementary charge and  $r$  the coordinate of relative motion.

The momentum operator  $\hat{p}$  depends on a radial and angular motion of the electron. For the solution of the already stationary Schrödinger equation, we assume a separation approach of these two sizes. For the energy spectra, it is already sufficient to deal only with the radial part (also consider that the problem is radially symmetric, the energy can only depend on the radial part of  $\psi$ ). The solution of energy levels and the wave function of the hydrogen atom can be obtained by making again use of hyper-geometric functions, in particular of the solution of the Kummer differential equation (a derivation of the solution can be looked up in [96, 97]):

$$E_n = -\frac{me^4}{2\hbar^2} \frac{1}{n^2} \equiv -\frac{1}{2} \frac{e^2}{a_0 n^2},$$

where  $a_0 = \frac{\hbar^2}{me^2}$  is called the Bohr radius.

The binding energy of the hydrogen atom in the ground state is

$$E_0 = -\frac{1}{2} \frac{e^2}{2a_0} = -13.6 \text{ eV.}$$

The wave function  $\psi_{nlm}$  depends on three quantum numbers, where  $n$  corresponds to the eigen-energy,  $l$  with  $0 \leq l \leq (n - 1)$  indicates the magnitude of the angular momentum and  $m$  with  $-l \leq m \leq l$  describes the magnetic quantum number, that gives the size of the z component of the angular momentum.

The solution for the wave function for the first quantum numbers can be seen in Fig. 4.7.

The paper [3] of this chapter was dedicated to Ian Sloan, a famous mathematician, who was

#### 4.4. EXAMPLES OF INTEGRABLE QUANTUM SYSTEMS

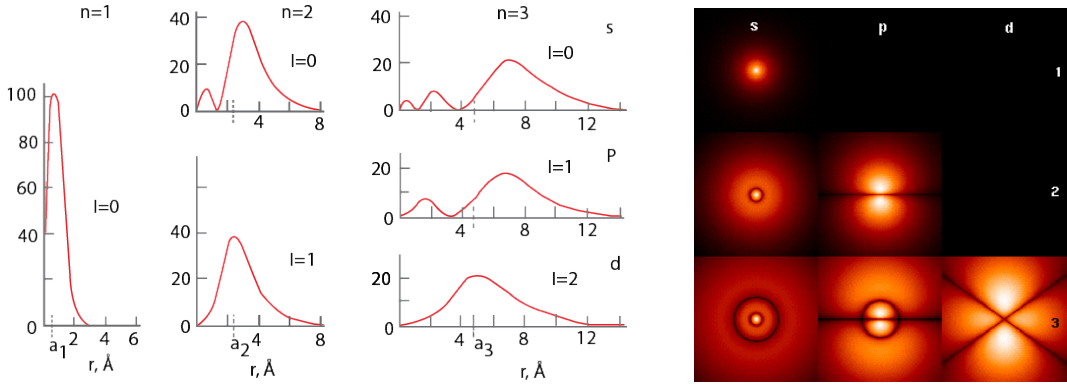


**Figure 4.7.:** Probability density of the hydrogen atom for quantum numbers  $n = 1, 2$ , and  $3$  (left-hand side) [98] and a section through the density distribution, source: [99].

active in particle physics during his early career, particularly in the field of calculating the energy spectra of atoms. On his very first research paper, in 1964, he studied in the proceedings of the Royal Society (London) the wave like behaviour of an ionized helium atom [15]. In his studies, he bombarded the atom with an electron and the goal was to measure the scattering cross-section in particular instead of measuring the atoms' wave function, he wanted to determine the scattered electrons wave function and to derive results for the helium atom. Schrödinger's equation for the atoms' electron is in this case very difficult to compute since the electron will also interact with the scattered electron. Thus, the potential cannot simply be assumed to be  $\frac{1}{r}$ , as it was the case for the above described hydrogen atom. Instead he came up with a few possible "ansatz" with limiting conditions, that he assembled together to obtain in the end a particular solution of Schrödinger's equation.

**Part II.**

**Papers**



---

## **Paper 1: Analytical methods for vacuum simulations in high energy accelerators for future machines based on LHC performances**

---

submitted to "Journal Physical Review Accelerator and Beams".

# Analytical methods for vacuum simulations in high energy accelerators for future machines based on the LHC performance

Ida Aichinger,\* Roberto Kersevan, and Paolo Chiggiato

*CERN, The European Organization for Nuclear Research, CH - 1211 Geneva, Switzerland*

(Dated: June, 2017)

The Future Circular Collider (FCC), currently in the design phase, will address many outstanding questions in particle physics. The technology to succeed in this 100 km circumference collider goes beyond present limits. Ultra-high vacuum conditions in the beam pipe is one essential requirement to provide a smooth operation. Different physics phenomena as photon-, ion- and electron- induced desorption and thermal outgassing of the chamber walls challenge this requirement. This paper presents an analytical model and a computer code PyVASCO that supports the design of a stable vacuum system by providing an overview of all the gas dynamics happening inside the beam pipes. A mass balance equation system describes the density distribution of the four dominating gas species H<sub>2</sub>, CH<sub>4</sub>, CO and CO<sub>2</sub>. An appropriate solving algorithm is discussed in detail and a validation of the model including a comparison of the output to the readings of LHC gauges is presented. This enables the evaluation of different designs for the FCC.

PACS numbers: 02.70.-c, 47.45.-n, 02.30.Hq, 29.20.db

## I. INTRODUCTION

The computation of residual gas particle (RGP) density profiles in particle accelerators is an essential task to optimize beam pipes and vacuum system design. In the last two decades, some software have been developed [1, 2]. They have been used for most of the high-energy accelerators presently in activity, including the Large Hadron Collider (LHC) at CERN.

There exists several approaches to evaluate gas density profiles [3–5]. The most general one would be to tackle directly the nonlinear integro-differential Boltzmann equation[6]. However, the solution of the Boltzmann equation requires an important computational effort due to the complicated structure of the collision integral. To reduce the complexity of the computation, gas density profile calculations have been performed by probabilistic Monte Carlo simulations, either by Direct Simulation Monte Carlo method (DSMC) [3] or, in a simpler way, by the test particle simulation Monte Carlo method (TPMC) [7]. Among the latter methods, MolFlow+ [1] is largely spread in the vacuum technology community. However, although such methods have found applications beyond particle accelerators [8], their extensions to time-dependent behaviours and multiple gas species phenomena are difficult, in particular for long vacuum sectors.

Analytical models can overcome such obstacles if the evaluation of one-dimension gas-density profiles is sufficient, preferably in simple geometries with cylindrical symmetry. A typical example is VASCO [2, 9], which was developed at CERN in 2004 for the interaction regions of the LHC. Recently, the preliminary design-study of the Future Circular Colliders (FCC) [10] with unprecedented high energy and vacuum requirements offers to extend the application of analytical methods. As an exam-

ple, the hadron-hadron version of the FCC with around 100 km circumference and 100 TeV centre of mass energy, requires a gas density in the arcs that is five times lower than the one in the LHC. In this paper, we revise and update the previous models, present the underlying theory and introduce a new elaborated software PyVASCO. In this new analytical method, we combined multiple effects due to material outgassing, beam induced desorption, conductance limitations, and different pumping mechanisms. A coupled differential equation system describes the mathematical framework of the model. Each equation represents the mass balance of one of the four dominant gas species H<sub>2</sub>, CH<sub>4</sub>, CO and CO<sub>2</sub>. These equations are coupled due to interaction of the different gas species among each other. For example, CO<sub>2</sub><sup>+</sup>–after ionization by the beam–may desorb H<sub>2</sub> from the beam pipe materials. Mathematically, the problem translates into a large sparse matrix equation system of first order, as in [2]. We developed a new optimized solving algorithm and implemented the model in a Python environment. This resulted in a significantly improved performance in speed and memory storage allowing to simulate 100 times longer vacuum systems than those achievable by the previous work [2] in less than 30 seconds. We benchmarked the simulation output with MolFlow+ and cross checked it to the readings of pressure gauges installed in accelerators. The latter verification is presented for the Long Straight Section (LSS) 4 and 5 of the LHC with a total length of over 1000 m along the beam line.

The focus of the simulation in this paper lies on circular hadron accelerators, since LHC’s gauge reading are available for verification and additionally the FCC-hh presents the ultimate goal of the design study. Nevertheless, the code PyVASCO is applicable to any other type of particle accelerators, like lepton machines, linacs and heavy-ion accelerators.

---

\* [ida.aichinger@cern.ch](mailto:id.aichinger@cern.ch)

## II. SETTING UP THE PHYSICAL VACUUM MODEL

This section provides an introduction to the physical quantities and laws that form the equation system of the vacuum dynamics with the particle density  $\mathbf{n}$  as unknown. The variables introduced here are summarized at the end of this section in TABLE I.

Mathematically,  $\mathbf{n}$  represents the vector-valued density function of the four dominating gas species  $\text{H}_2$ ,  $\text{CH}_4$ ,  $\text{CO}$  and  $\text{CO}_2$  as observed in a mass spectrum for a ultra-high vacuum (UHV) system (see Fig. 1).

$$\mathbf{n} = (n_{\text{H}_2}, n_{\text{CH}_4}, n_{\text{CO}}, n_{\text{CO}_2})^T \quad (1)$$

The framework of the Frenet-Serret coordinate system [11] is an appropriate choice for circular colliders, and the Cartesian coordinate system for straight linear colliders. In any case, we will refer to the vector pointing in the direction of the beam as  $x$ . The horizontal and vertical coordinates are noted by  $y$  and  $z$ , the time is noted by  $t$ . UHV systems are characterized by a high Knudsen number  $Kn > 10$  with:

$$Kn = \frac{k_B T}{\sqrt{2\pi\delta^2 pd}}, \quad (2)$$

where  $k_B$  is the Boltzmann constant,  $T$  the temperature,  $d$  the beam pipe diameter,  $\delta$  is the particle hard shell diameter and  $p$  the total pressure.

The pressure  $\mathbf{p}$  of the gas and the particle density  $\mathbf{n}$  in a UHV-system are correlated via the ideal gas law:

$$\mathbf{p} = \mathbf{n} \cdot k_B \cdot T \quad (3)$$

For clarification, the total pressure is the sum of the partial pressure values of each gas specie  $i$ :

$$p = \sum_{i=1}^4 p_i$$

The Maxwell Boltzmann distribution describes the particle speed  $v$  for ideal gases [7, 12]. The corresponding

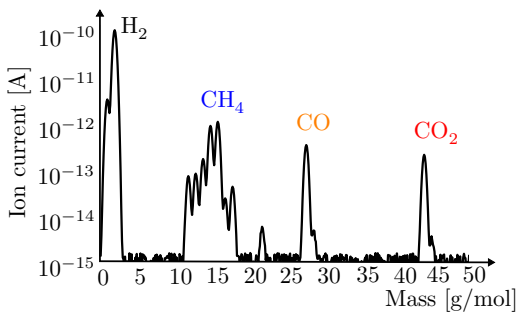


FIG. 1. Mass spectrum in a UHV system. The four peaks correspond to the presence of  $\text{H}_2$ ,  $\text{CH}_4$ ,  $\text{CO}$  and  $\text{CO}_2$  gas particles. The measured ion-current can be converted to the gas density with appropriate calibration coefficients.

mean velocity is given by

$$\bar{v} = \sqrt{\frac{8k_B T}{m\pi}} \quad (4)$$

depending on the molecular mass  $m$  and  $T$ . Fick's first and second laws of diffusion [3, 13] define the fundamental balance equation of the gas kinetics in a UHV-system. We get the following equation for an isotropic medium with a constant diffusion coefficient  $\mathbf{a}$ :

$$\frac{\partial \mathbf{n}}{\partial t} = \mathbf{a} \frac{\partial^2 \mathbf{n}}{\partial x^2} \quad (5)$$

if diffusion is one-dimensional. This assumption is appropriate since most of the time the length of the vacuum chamber is much bigger than its cross section, thus diffusion occurs mainly along the beam line. Furthermore, experimental data from the laboratory is also one-dimensional since they measure the gradient of gas concentration along the  $x$ -axis.

The diffusion coefficient  $\mathbf{a}$  depends on the particle's speed, its mass, and on the beam pipe geometry. Under molecular flow conditions,  $\mathbf{a}$  is given for cylindrical vacuum chambers by the specific conductance based on the calculations of Knudsen [7, 14]:

$$\mathbf{a} = \left(\frac{d}{2}\right)^2 \pi \cdot \frac{d}{3} \cdot \bar{v} = \frac{d^3 \pi}{12} \cdot \bar{v} \quad (6)$$

In order to generate a correct mass balance, continuous flow into and out of the system (see also subsection A, B), e.g. in terms of desorption or pumping, at a rate  $\mathbf{q}$  and  $\mathbf{r}$  per unit volume, must be added to the right side of Eq. (5):

$$\frac{\partial \mathbf{n}}{\partial t} = \mathbf{a} \frac{\partial^2 \mathbf{n}}{\partial x^2} + \mathbf{q}(x, t) - \mathbf{r}(x, t) \cdot \mathbf{n} \quad (7)$$

Note, that the flow out of the system is always proportional to the prevailing density  $\mathbf{n}$ , whereas the flow into the system can act independently of  $\mathbf{n}$ . Local sinks and sources, e.g. due to lumped pumps or outgassing related to possible tiny leaks are considered in the boundary conditions.

The idea is now to fragment the domain into a finite number of elements, where  $\mathbf{q}$ ,  $\mathbf{r}$  and  $\mathbf{a}$  can be taken as constant vectors. This allows to solve the equation system (7) locally on each element. The piecewise solution concept is identified by an additional index  $k$  (see Fig. 2).

Accordingly, appropriate intersection conditions combine the solutions to a global model. The conservation

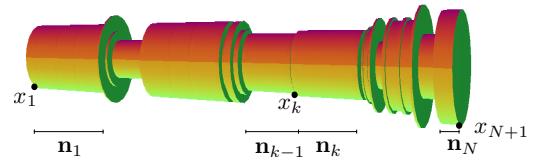


FIG. 2. Segmenting domain in  $N$  parts. Solution  $n_k$  describes density on segment  $k$ .

principle applied at the interface between two elements  $k$  and  $k + 1$  leads to density and flux continuity conditions. Thus, it holds at the intersection point  $x_k$  with a lumped gas source  $\mathbf{g}$  and a lumped pump  $\mathbf{s}$  (ion-pumps, turbomolecular pumps) that:

$$\mathbf{n}_{k-1} = \mathbf{n}_k \quad (8)$$

$$-\frac{D\mathbf{n}_{k-1}}{Dt} + \frac{D\mathbf{n}_k}{Dt} = \mathbf{s}_k \mathbf{n}_k - \mathbf{g}_k, \quad (9)$$

where the total derivative for a space-and-time dependent variable is given by [15, 16]:

$$\frac{D\mathbf{n}}{Dt} := \frac{\partial \mathbf{n}}{\partial t} + \mathbf{a} \cdot \frac{\partial \mathbf{n}}{\partial x} \quad (10)$$

Note, the change of sign in front of the term involving the total derivative: The derivative at the beginning of segment  $k$  points in the positive direction, while at the end of segment  $k - 1$ , it points in the negative direction.

At the extremities of the vacuum chamber open boundary conditions are assumed, hence only half of the pumping speed and half of the gas release is considered.

$$\frac{D\mathbf{n}_1}{Dt} = \frac{\mathbf{s}_1}{2} \mathbf{n}_1 - \frac{\mathbf{g}_1}{2} \quad \text{for } x = x_0 \quad (11)$$

$$\frac{D\mathbf{n}_N}{Dt} = \frac{\mathbf{s}_{N+1}}{2} \mathbf{n}_N - \frac{\mathbf{g}_{N+1}}{2} \quad \text{for } x = x_{N+1} \quad (12)$$

Note, also periodic boundary conditions at the extremities present a possible choice that set  $\mathbf{n}_1$  and  $\mathbf{n}_N$  in the sense of (8) and (9) in relation.

### A. Flow into the vacuum-system $\mathbf{q}$

There are four main phenomena, where particles are added to the system. The first three phenomena, described in the following subsections, are due to beam dynamic effects and are considered as the main impact on the dynamic gas density. In these cases, energetic particles as photons, ions and electrons bombard the chamber. If the energy spectrum of the impinging particles is in the electronic structure of the beam pipe material, then molecular desorption from the chamber walls may take place. The desorption probability is described by the parameter  $\eta$ . Its value is mainly specified by experimental data. In general, we consider three different types of impinging particles as photons, ions and electrons which lead to different desorption phenomena:

#### 1. Photon-induced desorption

Accelerated charged particles emit photons in the presence of magnetic fields. This process is called synchrotron radiation (SR) [17]. Its impact on vacuum systems is common for electron-positron circular colliders as for LEP [18] and could also be observed for high energy-proton circular colliders as the LHC [19]. The total number of photons emitted per second and per meter is described with the photon flux  $\dot{\Gamma}$ . It depends on the energy

of the accelerated particle expressed by the relativistic factor  $\gamma$  and the strength of the magnetic field in terms of the bending radius  $\rho$ :

$$\dot{\Gamma} = \frac{5\sqrt{3}\gamma}{24\pi\epsilon_0\hbar c}, \quad (13)$$

where  $\hbar$  is the reduced Planck constant,  $c$  the speed of light and  $\epsilon_0$  the permittivity of vacuum. The process of the photon-induced desorption depends on the energy spectrum of the impinging photons and on the material of the vacuum chamber. Nearly a linear dependence has been observed between the critical photon energy  $E_c$  in the range from 10-1000eV and the desorption yield for  $\eta_{ph}$  for the most commonly used materials of the beam chambers [20].  $E_c$  is the median of the photon energy spectrum:

$$E_c = \frac{3}{2} \frac{\hbar c}{\rho} \gamma^3,$$

The derived desorption yield for a copper-lined chamber, e.g. is given by [20]:

$$\begin{aligned} \eta(\text{H}_2) &\sim E_c^{0.74}, & \eta(\text{CH}_4) &\sim E_c^{0.94}, \\ \eta(\text{CO}) &\sim E_c^{1.01}, & \eta(\text{CO}_2) &\sim E_c^{1.12} \end{aligned}$$

Note, that photons below 4 eV do not provoke desorption, consequently the previous formula is valid, when the integral up to 4 eV presents only a small fraction of the total integral. In [20], the photon induced desorption was studied for a  $E_c$  up to 300eV.

### 2. Ion-induced desorption

The beam can ionize the RGP [21]. Consequently the generated positive ions are repelled by the positive space charge of the proton beam and impinge on the vacuum chamber walls, where they may cause desorption of tightly bounded molecules from the surface. This phenomena was observed for example in the Intersecting Storage Ring (ISR) at CERN [22].

In this process the different gas species may influence each other. The interaction is described by the desorption yield matrix

$$\mathbf{H}_{\text{ion}} = \begin{pmatrix} \eta_{\text{H}_2^+ \rightarrow \text{H}_2} & \eta_{\text{CH}_4^+ \rightarrow \text{H}_2} & \eta_{\text{CO}^+ \rightarrow \text{H}_2} & \eta_{\text{CO}_2^+ \rightarrow \text{H}_2} \\ \eta_{\text{H}_2^+ \rightarrow \text{CH}_4} & \eta_{\text{CH}_4^+ \rightarrow \text{CH}_4} & \eta_{\text{CO}^+ \rightarrow \text{CH}_4} & \eta_{\text{CO}_2^+ \rightarrow \text{CH}_4} \\ \eta_{\text{H}_2^+ \rightarrow \text{CO}} & \eta_{\text{CH}_4^+ \rightarrow \text{CO}} & \eta_{\text{CO}^+ \rightarrow \text{CO}} & \eta_{\text{CO}_2^+ \rightarrow \text{CO}} \\ \eta_{\text{H}_2^+ \rightarrow \text{CO}_2} & \eta_{\text{CH}_4^+ \rightarrow \text{CO}_2} & \eta_{\text{CO}^+ \rightarrow \text{CO}_2} & \eta_{\text{CO}_2^+ \rightarrow \text{CO}_2} \end{pmatrix}.$$

For clarification, the entry  $H_{4,1} = \eta_{\text{CO}_2^+ \rightarrow \text{H}_2}$  describes the probability that a  $\text{CO}_2^+$  ion desorbs a  $\text{H}_2$  molecule.

The process of desorbed particles is thus described with the product of the desorption yield matrix  $\mathbf{H}_{\text{ion}}$  and the ion flux  $\dot{\mathbf{I}}_{\text{ion}}$ :

$$\mathbf{H}_{\text{ion}} \cdot \dot{\mathbf{I}}_{\text{ion}} \cdot \mathbf{n} = \sum_{j=1}^4 \mathbf{H}_{i,j} \cdot \frac{I}{e} \sigma_j \cdot \mathbf{n}_j,$$

where the summation runs over all impinging species  $j$  that desorb particles of species  $i$ . The summand describes the product of the ion-induced desorption matrix entry ( $H_{i,j}$ ) with the number of ionized particles ( $\frac{I}{e}\sigma_j \cdot \mathbf{n}_j$ ), where  $I$  is the beam current,  $e$  the elementary charge,  $\sigma$  the ionization cross section and  $\mathbf{n}$  the RGP density. The ionization cross section for energies greater than 100 keV for a gas particle is calculated in [23]. Additionally, it is worth mentioning that  $\sigma$  is also depending on the ion energy, which in turn, depends on the beam current, making the ion-induced desorption term quadratic dependent on the beam current.

### 3. Electron-induced desorption - Electron cloud

The beam can generate some electrons from synchrotron radiation, impinging ionized gas molecules and spontaneous desorption induced by sufficiently high electromagnetic fields [24]. These primary electrons are accelerated by the positively charged beam, that hit the chamber wall and may produce a cascade of secondary electrons. The electrons are accelerated towards the positively charged beam, they cross the chamber and hit the wall again at the opposite side - producing more electrons and lead eventually to beam instabilities and gas desorption. This phenomenon depends in a complex way on the beam and chamber parameters and also on the bunch filling pattern. A CERN proprietary software PyECloud [25] addresses this phenomena. Based on observations, we can conclude that the bigger the aperture of the vacuum chamber, the longer is the duration that an electron is accelerated, the bigger is the surface where desorption can take place and the higher is the electron induced desorption. In addition, it has been observed in the LHC that the reduction of the bunch spacing to 25ns causes a significantly increased electron cloud effect in comparison to 50ns or to 100ns [26].

### 4. Other sources and summary of the total flow into the system

Thermal desorption generates what is usually called the static vacuum, which is present even in the absence of the beam. For example, chamber walls and the components within the chamber randomly release gas which was adsorbed at the surfaces or entrapped into

the bulk of the material. Air and water vapour may enter the system through leaks or permeate through seals. Gauges and beam instrumentation provide an additional source of outgassing.

Summarizing the flow into the vacuum system, gives the following expression for  $\mathbf{q}$ :

$$\mathbf{q}(x, t) = \underbrace{\mathbf{H}_{ion} \cdot \dot{I}_{ion} \cdot \mathbf{n}}_{\text{ion-induced desorption}} + \underbrace{\eta_{ph} \cdot \dot{\Gamma}_{ph}}_{\text{photon-induced desorption}} \\ + \underbrace{\eta_e \cdot \dot{N}_e}_{\text{electron-induced desorption}} + \underbrace{\pi \cdot d \cdot \mathbf{q}_{th}}_{\text{thermal outgassing}}$$

### B. Flow out of the vacuum-system $\mathbf{r}$

Particles are continuously added to the UHV-system, as we have seen in the previous section. Therefore sufficient pumping systems have to be installed, in terms of distributed and spatially localized pumps. The latter one is mainly provided by conventional pumps e.g. ion pumps or turbomolecular pumps. Apart from this, impinging RGP may also stick on the wall due to thermodynamic or chemical binding at the surface of the chamber. This describes then distributed pumping. For example, a special surface coating of the vacuum chamber of Al, Zr, Ti, V and Fe, better known as Non-Evaporable Getter (NEG) [27] induces distributed pumping. The RGP of H<sub>2</sub>, CO and CO<sub>2</sub> are first chemically trapped by the NEG coating and then adsorbed into the bulk of the material. After a surface coverage of about one monolayer of adsorption of CO and CO<sub>2</sub> on the surface, the NEG saturates and the pumping efficiency drops down to negligible values. CH<sub>4</sub> and noble gases are not adsorbed by NEG [28]. Distributed pumping also occurs in cryogenic areas, when a gas-particle hits the wall and immediately condenses. This phenomenon is known as cryo-pumping [29]. Generally, the number of molecules impinging on the wall under molecular flow equilibrium conditions is given by

$$\frac{A \cdot \bar{v}}{4}, \quad (14)$$

where  $A$  describes the lateral surface of the vacuum chamber, and  $\bar{v}$  the mean velocity of the RGP as defined in Eq. (4). In contrast to the distributed pumping particles sometimes get pumped only at an orifice on the beam pipe wall. For example, the holes in the LHC beam screen provide a linear pumping [30].

### C. Problem description

The central part of the model are the balance equations and the boundary conditions, summarized here:  
Mass-Balance equation for segment  $k$  (discarding here the index  $k$  for each coefficient):

$$\underbrace{\frac{\partial \mathbf{n}}{\partial t}}_{\text{Time variation of particles}} = \underbrace{\mathbf{a} \circ \frac{\partial^2 \mathbf{n}}{\partial x^2}}_{\text{Diffusion}} + \underbrace{\eta_{ph} \cdot \dot{\Gamma}_{ph}}_{\text{Desorption by photons}} + \underbrace{\eta_e \cdot \dot{N}_e}_{\text{by electrons}} + \boxed{\underbrace{\mathbf{H}_{ion} \cdot \dot{I}_{ion} \circ \mathbf{n}}_{\text{Ionization by beam and desorption by ions}}} + \underbrace{\mathbf{A} \cdot \mathbf{q}_{th}}_{\text{thermal outgassing}} - \underbrace{\alpha \circ \frac{\mathbf{A} \cdot \bar{\mathbf{v}}}{4} \circ (\mathbf{n} - \chi_{cryo} \mathbf{n}_e)}_{\text{wall distributed pumping}} - \underbrace{\mathbf{p}_l \circ \mathbf{n}}_{\text{linear pumping}}$$

*Multigasmodel*

Boundary and intersection conditions for segment  $k-1$  and  $k$ :

$$\mathbf{n}_{k-1}(x_k) = \mathbf{n}_k(x_k) \quad (16)$$

$$-\mathbf{a}_{k-1} \circ \mathbf{n}'_{k-1}(x_k) + \mathbf{a}_k \circ \mathbf{n}'_k(x_k) = \mathbf{s}_k \circ \mathbf{n}_k(x_k) - \mathbf{g}_k \quad (17)$$

$$\mathbf{a}_1 \circ \mathbf{n}'_1(x_1) = \frac{\mathbf{s}_1}{2} \circ \mathbf{n}_1(x_1) - \frac{\mathbf{g}_1}{2} \quad (18)$$

$$-\mathbf{a}_N \circ \mathbf{n}'_N(x_{N+1}) = \frac{\mathbf{s}_{N+1}}{2} \circ \mathbf{n}_N(x_{N+1}) - \frac{\mathbf{g}_{N+1}}{2} \quad (19)$$

**Remark.** The symbol  $\circ$  indicates a component wise multiplication of two vectors. The symbol  $'$  indicates the normal derivative at the boundaries.

Vectors are presented by lower-case bold letters (with the exception of Greek symbols) and matrices are presented by upper-case bold letters.

### III. ANALYTICAL SOLUTION METHOD

The introduced physical description of a vacuum system provides us now a model, that needs to be solved. We focus here on the solution concept from a mathematical point of view. The differential Eq. (15) has a solution that can be written in an exact and closed form under stationary assumptions. This assumption is applicable after a specific amount of pump-down time or when the accelerator operates at stable beam, then time variations are negligible and a stationary solution delivers accurate results. This leads to an elliptic partial differential equation with piecewise constant coefficients.

Introduced variables are summarized again at the end of this section in Table II.

An equivalent stationary problem description of the balance equation is given by:

$$\vec{0}_4 = \mathbf{A}(x) \frac{d\mathbf{n}^2}{dx^2} + \mathbf{B}(x)\mathbf{n} + \mathbf{c}(x) \quad (20)$$

with  $\mathbf{A}, \mathbf{B} \in \mathbb{R}^{4 \times 4}$  and  $\mathbf{c} \in \mathbb{R}^4$  being the matrix and vector assemblies of the parameters from the previous section:

$$\mathbf{A} = \mathbf{a} \cdot \mathbf{I}_4$$

$$\mathbf{B} = \mathbf{H}_{ion} \cdot \dot{I}_{ion} - \alpha \circ \frac{\mathbf{A} \cdot \bar{\mathbf{v}}}{4} - \mathbf{p}_l$$

$$\mathbf{c} = -\chi_{cryo} \cdot \alpha \circ \frac{\mathbf{A} \cdot \bar{\mathbf{v}}}{4} \circ \mathbf{n}_e + \eta_{ph} \cdot \dot{\Gamma}_{ph} + \eta_e \cdot \dot{N}_e + \mathbf{A} \cdot \mathbf{q}_{th}$$

The major challenge in solving this system lies in  $\mathbf{B}$ . A fully occupied matrix  $\mathbf{B}$  couples the balance equation of each specie with each other. The idea is to transform Eq. (20) to a system of first order equations, for which a solution concept is known [13, 31, 32]. Additionally, the idea is to split the domain into a finite number of

segments as it was already done in the previous section (see also Fig. 2), so that Eq. (20) provides constant coefficients on each segment. We solve the equation system independently on each segment and connect the obtained solutions with transformed intersection conditions. Thus, we can finally formulate a global solution  $\mathbf{n}$ :

$$\mathbf{n}(x) = \begin{cases} \mathbf{n}_1(x) & x_1 \leq x \leq x_2 \\ \mathbf{n}_2(x) & x_2 < x \leq x_3 \\ \vdots & \\ \mathbf{n}_N(x) & x_N < x \leq x_{N+1} \end{cases} \quad (21)$$

#### A. Transformed problem description

The problem description (21) is converted to a system of first-order linear equations with a change of variable. This modification reduces the order by one, but also doubles the amount of equations posed.

$$\mathbf{y} := \begin{pmatrix} \mathbf{n} \\ \frac{d\mathbf{n}}{dx} \end{pmatrix}$$

$$\mathbf{M} := \begin{pmatrix} \mathbf{0}_{4 \times 4} & \mathbf{I}_4 \\ -\mathbf{A}^{-1}\mathbf{B} & \mathbf{0}_{4 \times 4} \end{pmatrix}, \mathbf{b} := \begin{pmatrix} \mathbf{0}_{4 \times 4} \\ -\mathbf{A}^{-1}\mathbf{c} \end{pmatrix}$$

$$\mathbf{F}_1 := \begin{pmatrix} -\frac{\mathbf{s}_1 \mathbf{I}_4}{2} & \mathbf{A} \end{pmatrix}, \mathbf{F}_N := \begin{pmatrix} -\frac{\mathbf{s}_{N+1} \mathbf{I}_4}{2} & -\mathbf{A} \end{pmatrix}$$

$$\mathbf{H}_k := \begin{pmatrix} \mathbf{I}_4 & \mathbf{0}_{4 \times 4} \\ \mathbf{0}_{4 \times 4} & -\mathbf{A}_k \end{pmatrix}, \mathbf{S}_k := \begin{pmatrix} \mathbf{0}_{4 \times 4} & \mathbf{0}_{4 \times 4} \\ \mathbf{s}_k \mathbf{I}_4 & \mathbf{0}_{4 \times 4} \end{pmatrix} \text{ and}$$

$$\bar{\mathbf{g}}_k := \begin{pmatrix} \vec{0}_4 \\ -\mathbf{g}_k \end{pmatrix}$$

TABLE I. Model parameters for physical description.

Symbol	Dim	Unit	Description
$\mathbf{n}$	$\mathbb{R}^4$	Particles/m <sup>3</sup>	vector-valued particle density function of H <sub>2</sub> , CH <sub>4</sub> , CO and CO <sub>2</sub>
$\mathbf{a}$	$\mathbb{R}^4$	m <sup>4</sup> /s	Specific conductance
$\dot{\Gamma}_{ph}$	$\mathbb{R}$	photons/(s · m)	Emitted photon flux by the bended beam in the magnetic areas
$\dot{N}_e$	$\mathbb{R}$	electrons/(s · m)	Electron flux impinging on the chamber wall due to the electron cloud phenomena
$\dot{I}_{ion}$	$\mathbb{R}$	ion/(s · m)	Ion flux, it is proportional to $\mathbf{n}$
$\frac{I}{e}$	$\frac{1}{s}$		Number of high energy protons passing per second
$\eta_{ph}$	$\mathbb{R}^4$	1	Photon induced desorption yield ( $\eta \geq 0$ ) describes the number of molecules desorbed per photon
$\eta_e$	$\mathbb{R}^4$	1	Electron induced desorption yield ( $\eta \geq 0$ ) describes the number of molecules desorbed per electron
$\mathbf{H}_{ion}$	$\mathbb{R}^{4 \times 4}$	1	Ion induced desorption yield, probability that ion of specie $i$ desorbs molecule of specie $j$ for $i, j \in \{\text{H}_2, \text{CH}_4, \text{CO}, \text{CO}_2\}$
A	$\mathbb{R}$	m	Lateral surface per unit-length of beam chamber
$\mathbf{r}$			Sinks of a UHV-system
$\mathbf{q}$			Sources of a UHV-system
$\mathbf{q}_{th}$	$\mathbb{R}^4$	1/(m <sup>2</sup> s) <sup>a</sup>	Thermal outgassing rate
$\alpha$	$\mathbb{R}^4$	1	Sticking coefficient
$\bar{\mathbf{v}}$	$\mathbb{R}^4$	m/s	Average Maxwell-Boltzmann velocity of the four gas species
$\mathbf{p}_l$	$\mathbb{R}^4$	m <sup>2</sup> /s	Linear pumping per unit-length
N	$\mathbb{R}$	1	Number of segments
d	$\mathbb{R}$	m	Diameter
L	$\mathbb{R}$	m	Length of segment
T	$\mathbb{R}$	K	Absolute temperature of segment
$\mathbf{s}_k$	$\mathbb{R}^4$	m <sup>3</sup> /s	Pumping speed of lumped pump located on the beginning of segment $k$
x	$\mathbb{R}$	m	Spatial coordinate along beam line
$x_k$	$\mathbb{R}$	m	Intersection point of segment $k - 1$ and $k$
$\mathbf{g}$	$\mathbb{R}^4$	1/s	Local punctual gas source (e.g. gas leak)
$\sigma$		ion/proton · m <sup>2</sup>	Ionisation cross section of residual gas molecules by high energy protons
$k_B$		m <sup>2</sup> kg/(s <sup>2</sup> K)	Boltzmann constant $k_B = 1.3806488 \cdot 10^{-23}$
p	$\mathbb{R}$	Pa	Total pressure
$\mathbf{p}$	$\mathbb{R}^4$	Pa	Equivalent pressure for particle density $\mathbf{n}$ using ideal gas equation
$\chi_{cryo}$	$\mathbb{N}$		$\chi = 1$ for cryogenic areas and 0 for room temperature areas
$\mathbf{n}_e$	$\mathbb{R}^4$	1/m <sup>3</sup>	Background density without beam (static density)

<sup>a</sup> [ $\tilde{\mathbf{q}}$ ] = [ $\frac{\text{mbar}\cdot\text{l}}{\text{s}\cdot\text{cm}^2}$ ] is more common in practice.  $\mathbf{q}_{th} = \tilde{\mathbf{q}} \cdot \frac{10^3}{k_B \cdot T}$

The problem description reads now as follows:

$$\frac{dy}{dx}(x) = \mathbf{My}(x) + \mathbf{b} \quad (22)$$

$$\mathbf{H}_{k-1}\mathbf{y}_{k-1}(L) - (\mathbf{H}_k + \mathbf{S}_k)\mathbf{y}_k(0) = \bar{\mathbf{g}}_k \quad (23)$$

$$\mathbf{F}_1\mathbf{y}_1(0) = -\mathbf{g}_1 \quad (24)$$

$$\mathbf{F}_N\mathbf{y}_N(x_{N+1}) = \mathbf{g}_{N+1}, \quad (25)$$

where (22) describes the balance equation, (23) the intermediate condition, (24) the initial condition and (25) the end condition.

### B. Solution for segment $k$

The existence and uniqueness of a solution  $y(x)$  for segment  $k$  to the Eq. (22) with an arbitrary constant  $u$

is posed by the fundamental Theorem of Picard Lindelöf [33–35]. The index  $k$  is again discarded for readability. For each segment  $k$ , the solution  $y(x)$  can be stated as

$$\boxed{\mathbf{y}(x) = \underbrace{e^{(x-x_k)\mathbf{M}} \mathbf{u}}_{\mathbf{P}(x)} + \underbrace{\int_{x_k}^x e^{(x-\tilde{x})\mathbf{M}} \mathbf{b} d\tilde{x}}_{\mathbf{z}(x)}} \quad (26)$$

for  $x_k \leq x \leq x_{k+1}$ .

The integration constant  $\mathbf{u}$  needs to be determined from the boundary and intersection conditions, demonstrated in subsection C.  $\mathbf{P}(x)$  describes the fundamental system and  $\mathbf{z}(x)$  represents a particular solution of Eq. (22). The integral in  $\mathbf{z}(x)$  can be solved to

$$\mathbf{z}(x) = (\mathbf{P}(x) - \mathbf{I}_8)\mathbf{M}^{-1}\mathbf{b} \quad (27)$$

The solution for an invertible matrix  $\mathbf{M}$ , in case of a no-beam simulation, where  $\mathbf{B}$  equals a zero-matrix, is shown

later in section D.

The validity of the solution (26) can be easily verified by differentiation.

### C. Global solution by implementing boundary and intersection conditions

The local solutions  $\mathbf{y}_k(x)$  are now connected with boundary and intersection conditions to form the global solution  $\mathbf{y}(x)$  (similar to expression (21)) and to determine the integration coefficient  $u_k$ .

Some algebraic transformations of the boundary conditions are needed to proceed. We know that:

$$\mathbf{y}(0) = P(0) \cdot \mathbf{u} + \mathbf{z}(0) \quad (28)$$

$$\mathbf{y}(L) = P(L) \cdot \mathbf{u} + \mathbf{z}(L) \quad (29)$$

We use (28), (29) to transform (23) to the form

$$\begin{pmatrix} \mathbf{u}_k \\ 1 \end{pmatrix} = \mathbf{TM}(k-1, k) \begin{pmatrix} \mathbf{u}_{k-1} \\ 1 \end{pmatrix}, \quad (30)$$

where  $\mathbf{TM} \in \mathbb{R}^{9 \times 9}$  describes the transformation matrix that maps the unknown  $\mathbf{u}$  from segment  $k-1$  to segment  $k$ .  $\mathbf{TM}$  has the following form for  $2 \leq k \leq N$ :

$$\mathbf{TM}(k-1, k) =$$

$$\left( \begin{array}{c|c} [(\mathbf{H}_k + \mathbf{S}_k) \cdot \mathbf{P}_k(0)]^{-1} \cdot & -\bar{\mathbf{g}}_k + \mathbf{H}_{k-1}\mathbf{z}_{k-1}(L) - \\ \mathbf{H}_{k-1}\mathbf{P}_{k-1}(L) & (\mathbf{H}_k + \mathbf{S}_k) \cdot \mathbf{z}_k(0) \\ \hline 0 \dots 0 & 1 \end{array} \right)$$

This form can be deduced by the transformation of the intermediate conditions and further elementary algebraic calculations. For more details see Appendix A.

We observe with this the following expression that maps the integration coefficient of the first segment to the last segment.

$$\begin{pmatrix} \mathbf{u}_N \\ 1 \end{pmatrix} = \underbrace{\prod_{k=2}^N \mathbf{TM}(k, k-1)}_{=: \mathbf{SM}} \cdot \begin{pmatrix} \mathbf{u}_1 \\ 1 \end{pmatrix} \quad (31)$$

The transformation product defines a new matrix  $\mathbf{SM}$ . In the same way we use (28), (29) to modify (24) and (25):

Let  $\bar{\mathbf{F}}_1, \bar{\mathbf{F}}_N \in \mathbb{R}^{4 \times 9}$  and  $\bar{\mathbf{u}}_1, \bar{\mathbf{u}}_N \in \mathbb{R}^9$ , then we can write:

$$\begin{aligned} \left( \begin{array}{c|c} \bar{\mathbf{F}}_1 & \bar{\mathbf{u}}_1 \\ \mathbf{F}_1 \mathbf{P}_1(0) & \mathbf{F}_1 \mathbf{z}_1(0) + \mathbf{g}_1 \end{array} \right) \cdot \underbrace{\begin{pmatrix} \mathbf{u}_1 \\ 1 \end{pmatrix}}_{=: \bar{\mathbf{u}}_1} &= \begin{pmatrix} 0 \\ 0 \\ 0 \\ 0 \end{pmatrix} \\ \left( \begin{array}{c|c} \bar{\mathbf{F}}_N & \bar{\mathbf{u}}_N \\ \mathbf{F}_N \mathbf{P}_N(L) & \mathbf{F}_N \mathbf{z}_N(L) - \mathbf{g}_{N+1} \end{array} \right) \cdot \underbrace{\begin{pmatrix} \mathbf{u}_N \\ 1 \end{pmatrix}}_{=: \bar{\mathbf{u}}_N} &= \begin{pmatrix} 0 \\ 0 \\ 0 \\ 0 \end{pmatrix} \end{aligned}$$

Note, that the additional vector entry of  $\bar{\mathbf{u}}_1$  is required in order to also describe constant algebraic transformations in the boundary conditions.

We rewrite the boundary conditions now to the final system of equations:

$$\left( \begin{array}{c|c} \mathbf{SM} & -I_{(9 \times 9)} \\ \bar{\mathbf{F}}_1 & 0_{(4 \times 9)} \\ \mathbf{0}_{(4 \times 9)} & \bar{\mathbf{F}}_N \\ \hline 0 \dots 0 & 0 \dots 0 - 1 \end{array} \right) \cdot \underbrace{\begin{pmatrix} \bar{\mathbf{u}}_1 \\ \bar{\mathbf{u}}_N \end{pmatrix}}_{\in \mathbb{R}^{18 \times 1}} = \underbrace{\begin{pmatrix} 0 \\ \vdots \\ 0 \\ 0 \end{pmatrix}}_{\in \mathbb{R}^{18 \times 1}} \quad (32)$$

Solving Eq. (32) with a Gauss-Jordan elimination algorithm [36], using the transformation-identity of Eq. (30) and evaluating (26), gives us the solution  $\mathbf{y}(x)$ . The backward transformation of  $\mathbf{y}$  defines the particle density  $\mathbf{n}$  at each axial point of the simulation domain.

### D. Special case: Single-gas model

The equation system (20) becomes decoupled, if the gas species do not interact with each other. This is the case when the ion-induced desorption matrix  $\mathbf{H}_{ion}$  is diagonal, or if  $\mathbf{H}_{ion}$  describes the zero-matrix in the case of no beam.

Note, that a diagonal matrix of  $\mathbf{H}_{ion}$  can be forced to approximate the solution by the following transformation:

$$\tilde{\mathbf{H}}_{\text{single}}^{\text{ion}} = \frac{\sum_l \mathbf{H}_{kl}^{\text{ion}} \cdot \sigma_l}{\sum_l \sigma_l} \quad (33)$$

We solve the equation system individually for each gas species using an exponential approach  $n(x) = \exp(\lambda x)$  for a  $\lambda \in \mathbb{R}$ . This gives us the following real solutions  $n_i(x)$  of Eq. (20) for the gas specie  $i$ :  $n_i(x) =$

$$\begin{cases} C_1 \cdot \exp\left(\sqrt{-\frac{b}{a}}x\right) + C_2 \cdot \exp\left(-\sqrt{-\frac{b}{a}}x\right) - \frac{c}{b} & \text{for } b < 0 \\ C_1 \cdot \cos\left(\sqrt{\frac{b}{a}}x\right) + C_2 \cdot \sin\left(\sqrt{\frac{b}{a}}x\right) - \frac{c}{b} & \text{for } b > 0 \\ C_1 + C_2 x - \frac{c}{2a} x^2 & \text{for } b = 0 \end{cases}$$

$a, b$  and  $c$  are in this case one dimensional coefficients of gas specie  $i$  and  $n_i$  is its one-dimensional density function. The integration constants  $C_1$  and  $C_2$  can be easily obtained with the boundary and intersection conditions, following the simplified solution concept from the previous subsection.

## IV. VALIDATION OF THE MODEL BY BENCHMARK EXAMPLES

The model has been thoroughly tested in the framework of benchmark examples and real-case scenarios for

TABLE II. Model parameters for mathematical description.

Symbol	Dim	Description
$\mathbf{y}$	$\mathbb{R}^8$	vector-valued function describing the RGP density and its derivative
$\mathbf{I}_4$	$\mathbb{R}^{4 \times 4}$	Identity matrix
$\mathbf{0}_{4 \times 4}$	$\mathbb{R}^{4 \times 4}$	Zero matrix
$\vec{\mathbf{0}}_4$	$\mathbb{R}^4$	Zero vector
$x$	$\mathbb{R}$	Spatial coordinate along beam line
$x_k$	$\mathbb{R}$	Intersection point of segment $k - 1$ and $k$
$\mathbf{A}, \mathbf{B}$	$\mathbb{R}^{4 \times 4}$	Coefficients of balance equation
$\mathbf{c}$	$\mathbb{R}^4$	Coefficients of balance equation
$\mathbf{M}$	$\mathbb{R}^{8 \times 8}$	Coefficients of transformed balance equation
$\mathbf{b}$	$\mathbb{R}^8$	Coefficients of transformed balance equation
$\mathbf{P}$	$\mathbb{R}^{8 \times 8}$	Fundamental system of transformed balance equation
$\mathbf{z}$	$\mathbb{R}^8$	Particular solution of transformed balance equation
$\mathbf{u}$	$\mathbb{R}^8$	Integration constants of balance equation
$\bar{\mathbf{u}}$	$\mathbb{R}^8$	Integration constants of balance equation with an artificial extra vector entry at the end.
$\mathbf{F}_1, \mathbf{F}_N$	$\mathbb{R}^{4 \times 8}$	Coefficients of boundary conditions
$\bar{\mathbf{F}}_1, \bar{\mathbf{F}}_N$	$\mathbb{R}^{4 \times 9}$	Coefficients of homogenized boundary conditions
$\mathbf{H}, \mathbf{S}$	$\mathbb{R}^{8 \times 8}$	Coefficients of intersection conditions
$\mathbf{H}_{\text{ion}}, \tilde{\mathbf{H}}_{\text{ion}}$	$\mathbb{R}^{4 \times 4}$	Ion-induced desorption matrix wrt multi- and single-gas framework
$\mathbf{g}$	$\mathbb{R}^4$	Local lumped gas source (e.g. leak)
$s_k$	$\mathbb{R}^4$	Pumping speed of lumped pump located at the beginning of segment $k$
$\bar{\mathbf{g}}$	$\mathbb{R}^8$	Coefficients of intersection conditions
$\mathbf{T}\mathbf{M}$	$\mathbb{R}^{9 \times 9}$	Transformation matrix: maps coefficients from segment ( $k-1$ ) to $k$
$\mathbf{S}\mathbf{M}$	$\mathbb{R}^{9 \times 9}$	Transformation matrix: maps coefficients from the first segment to the last one.
$n(x)$	$\mathbb{R}$	Particle density for one gas specie (Single-gas framework)
$a, b, c$	$\mathbb{R}$	Coefficients of balance equation for one gas specie (Single-gas framework), e.g. $a = A_{11}$
$C_1, C_2$	$\mathbb{R}$	Integration constants of balance equation (Single-gas framework)

the Large Hadron Collider (LHC) at CERN. We give five representative examples out of the many used as benchmark for this study.

The analytical model presented in this paper is referred to as “PyVASCO” in the following section.

### A. Crosscheck with Molflow+

Molflow+ uses a stochastic approach to simulate the RGPs with Test-Particle Monte Carlo methods for one gas specie at a time. Molflow+ traces the trajectory of virtual particles from the gas source to the pumping location and derives from this the RGP density in the vacuum chamber. The advantage of Molflow+ is that it can consider complex geometries. PyVASCO, on the other hand, can consider multiple gas species at a time and beam induced effects. As a side-note, Molflow+ can also consider photon induced desorption by coupling Molflow+ with the closely related program SynRad+ [8]. To meet the assumptions of both models, we choose a simple cylindrical geometry and put the ionization matrix to zero to

avoid intermolecular dependencies. We explicitly tested variations of outgassing rates  $\mathbf{q}$ , sticking coefficients  $\alpha$ , conductances and diameters. In these benchmark examples both models show a very good agreement. For readability reasons, all figures and tables are inserted at the end of the subsections.

The geometry for the first three examples is visualized in Fig. 3. It is one single beam pipe consisting of two materials  $M_1$  and  $M_2$  defined in Table IV-VI.

#### 1. Example - Variation of mass

The first example represents the influence of the particle’s mass to the density distribution. Explicitly, the conductance depends on the mass of the RGP, hence different gas species provide different conductances. Table III lists the molecular masses of  $H_2$ ,  $CH_4$ ,  $CO$  and  $CO_2$ . Fig. 5 presents then the simulation output for the distribution of the particle density assuming the same outgassing  $\mathbf{q}$  and sticking  $\alpha$  properties for each gas species. The results confirm the well-known fact that the higher the molecular mass of the specie, the lower is the conductance and the higher is the RGP density.

#### 2. Example - Variation of outgassing rate

This and the following two examples simulate only the density distribution of  $H_2$  particles for the geometry of Fig. 3. Example 2 focuses on the behaviour of different outgassing values  $\tilde{\mathbf{q}}$  to the simulations. The results are presented in Fig. 6 and they clearly show a linear relation among the different outgassing coefficients  $\tilde{\mathbf{q}}$ . This is an expected result.

#### 3. Example - Variation of sticking coefficient

Example 3 determines the effect of different sticking factors to the density profile. Fig. 7 shows that its effect can not be as easily deduced as it was in Example 2 for the outgassing rate. The reason is that the amount of particles removed from the system due to the sticking coefficient is depending on the prevailing density, see balance Eq. (15) from the previous sections.

#### 4. Example - Variation of diameter

Example 4 is applied to the geometry of Fig. 4 of material  $M_3$  and  $M_4$  listed in Table VII to test the effect of different geometries. The vacuum chamber is described by four segments with an increasing diameter from 100 - 400mm. The results in Fig. 8 show a good match except for the last case that assumes a very high sticking factor  $\alpha \geq 0.1$  and zero outgassing. We want to note here, that this is an hypothetical test case and there

are barely domains in the LHC where this configuration could be found. The explanation of the underestimation of the density profile is due to the beaming effect. This means, that particles from a gas source may propagate along the vacuum chamber direction and these particles do not experience the sticking coefficient at all and increase the density in a domain several meters further away. The piecewise solution implemented in our simulation-method cannot capture such an effect [37].

A solution to this problem is to set an additional very small outgassing rate  $\tilde{q} = 10^{-14} \text{ mbar}\cdot\text{l s}\cdot\text{cm}^2$  in the corresponding domain, here it is set at the first segment that has a diameter of 100mm. The result is plotted in Fig. 9.

### 5. Observations - PyVASCO vs. Molflow+

All benchmark examples show a good match between the analytic code PyVASCO and the Monte-Carlo code Molflow+. The fact that two models with different approaches give the same result increases the credibility of both simulation codes.



FIG. 3. Geometry for Example 1-3: One beam pipe with two materials  $M_1$  and  $M_2$

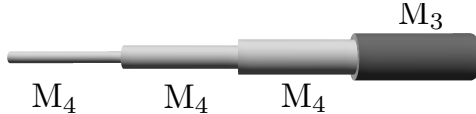


FIG. 4. Geometry for Example 4 with materials  $M_3$  and  $M_4$

TABLE III. Mass of the four main gas species in a UHV system [38].

	$H_2$	$CH_4$	$CO$	$CO_2$
mass[g/mol]	2	16	28	44

TABLE IV. Material  $M_1$  and  $M_2$  specifications for Example 1.

	$\alpha$	$\tilde{q} \times 10^{-12} [\text{mbar}\cdot\text{l s}\cdot\text{cm}^2]$
$M_1$	$8 \cdot 10^{-3}$	3.97
$M_2$	$10^{-12}$	39.8

TABLE V. Material  $M_1$  and  $M_2$  specifications for Example 2 (only  $H_2$ ).

	$\alpha$	$\tilde{q}_1$	$\tilde{q}_2$	$\tilde{q}_3$	$\tilde{q}_4$	$\tilde{q} \times 10^{-14} [\text{mbar}\cdot\text{l s}\cdot\text{cm}^2]$
$M_1$	$8 \cdot 10^{-3}$	1000	100	10	1	
$M_2$	$10^{-12}$	10000	1000	100	10	

TABLE VI. Material  $M_1$  and  $M_2$  specifications for Example 3 (only  $H_2$ ).

	$\alpha_1$	$\alpha_2$	$\alpha_3$	$\tilde{q} \times 10^{-14}$
$M_1$	$10^{-5}$	$10^{-4}$	$10^{-3}$	8
$M_2$	$10^{-13}$	$10^{-12}$	$10^{-11}$	800

TABLE VII. Material  $M_3$  and  $M_4$  specifications for Example 4 (only  $H_2$ ).

	$\alpha_1$	$\alpha_2$	$\alpha_3$	$Q$
$M_3$	$10^{-3}$	$10^{-2}$	$10^{-1}$	$10^{-10}$
$M_4$	$10^{-3}$	$10^{-2}$	$10^{-1}$	0

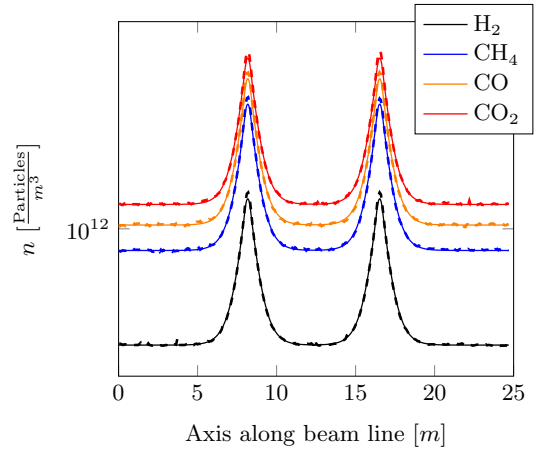


FIG. 5. Example 1: Conductance variation in comparison with PyVASCO (solid line) and Molflow+ (dashed line) for the geometry of Fig. 3.

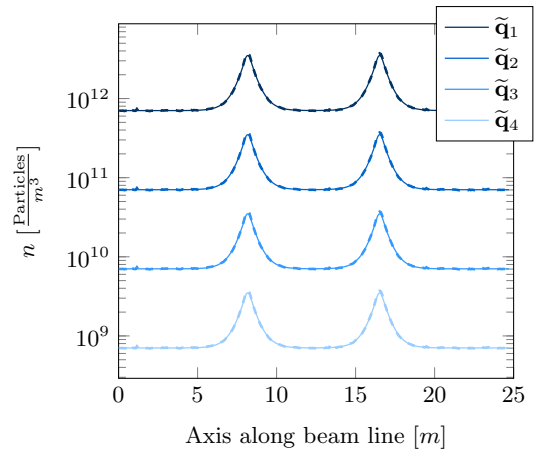


FIG. 6. Example 2: Outgassing variation for  $H_2$  in comparison with PyVASCO (solid line) and Molflow+ (dashed line) for the geometry of Fig. 3.

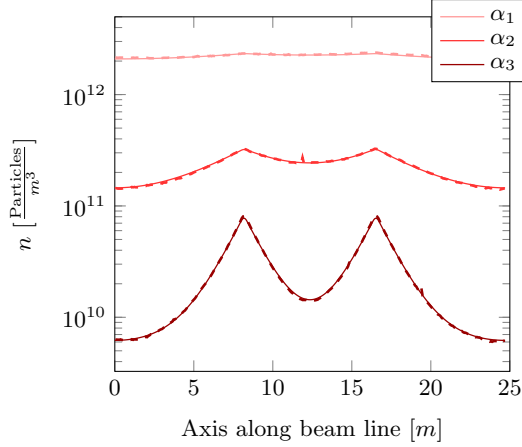


FIG. 7. Example 3: Sticking variation for  $H_2$  in comparison with PyVASCO (solid line) and Molflow+ (dashed line) for the geometry of Fig. 3.

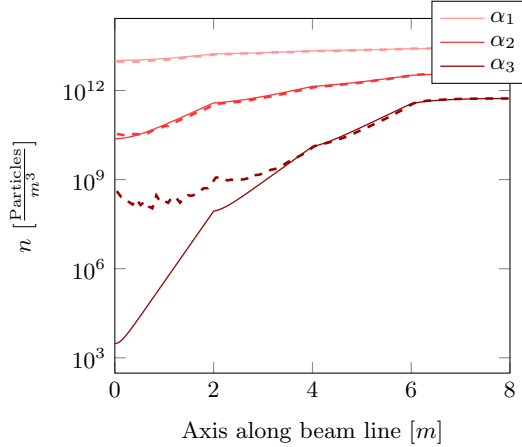


FIG. 8. Example 4: Sticking variation for  $H_2$  in comparison with PyVASCO (solid line) and Molflow+ (dashed line) for the geometry of Fig. 4.

## B. Sensitivity of the ion-induced desorption

We study in this subsection the sensitivity of the ion-induced desorption phenomena (see subsection II.A.2) on the simulation output. A high beam current and a fully occupied matrix  $\mathbf{H}_{\text{ion}}$  imply that the different gas-species influence each other and hence mathematically one numerical instability of one gas-specie can map to the other gas species. Hence, an emphasize lies on a stable influence of this phenomena.

We study therefore the variation in the output, when we use a multi-gas framework ( $\mathbf{H}_{\text{multi}}$ ), a single-gas framework ( $\mathbf{H}_{\text{single}}$ ) and a zero-beam framework ( $\mathbf{H}_{\text{zero}}$ )

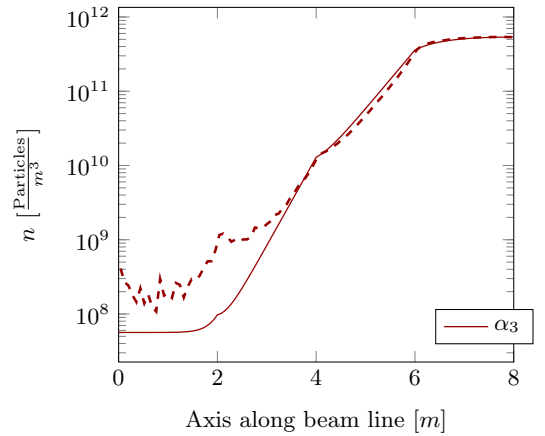


FIG. 9. Example 4: A high sticking factor makes beaming effect visible; comparison PyVASCO (solid line) and Molflow+ (dashed line) with corrected outgassing  $\tilde{\mathbf{q}}$ .

with:

$$\mathbf{H}_{\text{multi}} = \begin{pmatrix} 0.54 & 0.1 & 0.1 & 0.1 \\ 0.1 & 0.54 & 0.1 & 0.1 \\ 0.1 & 0.1 & 0.54 & 0.1 \\ 0.1 & 0.1 & 0.1 & 0.54 \end{pmatrix},$$

$$\mathbf{H}_{\text{single}} = \text{diag}(\mathbf{H}_{\text{multi}}), \quad \mathbf{H}_{\text{zero}} = 0 \cdot \mathbf{H}_{\text{multi}}$$

Fig. 10 shows the 6 m long cylindrical vacuum chamber that we use for this analysis and Table VIII lists the parameter of pumping speed and outgassing rate. The material has no sticking property in this case to illustrate the ion-induced desorption dynamics better.

We compare all three frameworks in Fig. 11, with the presence of a weak beam ( $I = 0.01\text{A}$ ). The matrix entries of  $\mathbf{H}^{\text{ion}}$  are therefore all close to zero and we expect, as shown also in Fig. 11, three times the same result.

In Fig. 12 we see, how a higher beam current of  $I = 10\text{A}$  influences the output for the single-gas framework; the result is as expected. A higher current implies more collisions of beam particles with RGP, which consequently get ionized. They impinge on the wall and hence increase the ion-induced desorption. The heavier  $CO_2$  molecules present a higher ionization cross-section than for example  $H_2$ . The density increase for a higher beam current is therefore stronger for  $CO_2$  than for  $H_2$ .

Fig. 13 reflects the difference between the multi-gas framework and the single-gas framework at a high beam current ( $I = 10\text{A}$ ) and hence especially analyses how the off-diagonal entries influence the result. Firstly, we observe a different values in the density profiles. The additional cross-desorption probability from the off-diagonal entries causes this reasonably small increase. Secondly, the shape of the profile remains the same, as we expect from a stable model, when the input parameters are changed only by a small quantity. Thirdly,  $H_2$  shows

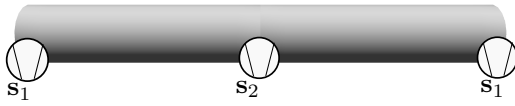


FIG. 10. Beam-pipe with three pumps to test the ion-induced desorption sensitivity.

TABLE VIII. Parameters for pumps and material properties of Fig. 10.

	$H_2$	$CH_4$	$CO$	$CO_2$
$s_1 [l/s]$	1100	1100	1100	1100
$s_2 l/s$	550	550	550	550
$\tilde{q} [\text{mbar} \cdot \text{s}^{-1}] \times 10^{-15}$	1	1	1	1
$\alpha$	0	0	0	0
$\sigma \times 10^{-23}$	4.45	31.8	27.5	42.9

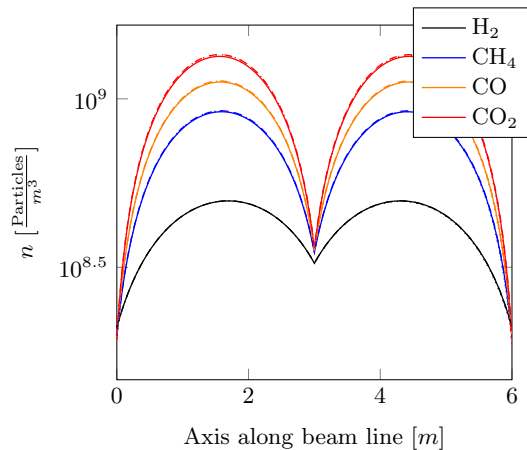


FIG. 11. Comparison of zero-beam (solid line) and single-gas (dashed line) and multi-gas (dotted line) framework with current  $I = 0.01A$

the biggest increase in its density. The reason is that the ion-induced desorption is proportional to the prevailing density  $n$ . This means that the higher density of  $CO_2$  has a stronger influence on the density of  $H_2$  than inverse.

Concluding, the results for testing the sensitivity of the model to the coupled equation term of the ion-induced desorption reflects a stable model and gives no indication to any instabilities.

## V. VALIDATION OF THE MODEL IN COMPARISON TO LHC GAUGE READINGS

The last step to validate the model lies in the comparison of the simulation results with measured data from gauges in the LHC. The LHC contains eight long straight sections (LSS) consisting of two parts of about 265 meters with a point of interest (detector) in the middle. The CMS experiment is installed in one LSS and we

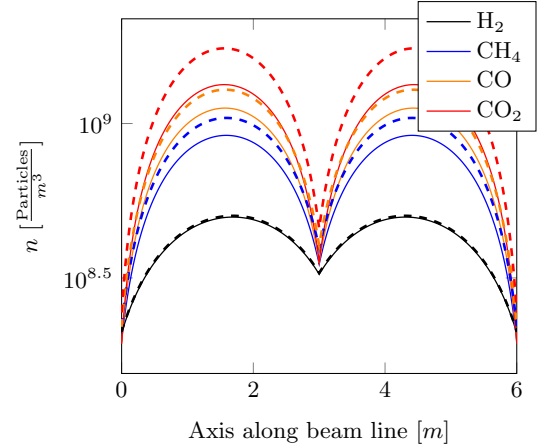


FIG. 12. Difference between zero beam (solid line) and a high beam current  $I = 10A$  (dashed line) for the single-gas framework.

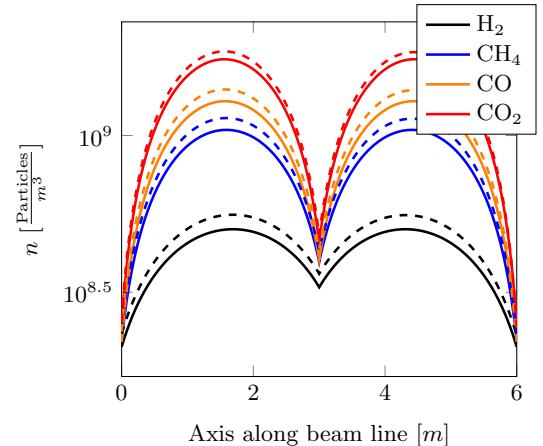


FIG. 13. Difference between single-gas with  $H_{\text{Single}}$  (solid line) and multi-gas with  $H_{\text{Multi}}$  (dashed line) simulations, both at  $I = 10A$ .

compare the pressure gauge readings in this area for a beam of 6.5 TeV with our simulations.

The simulations contain a combination of many different density regimes driven by the 14 varying input of geometries, materials and beam induced effects. We divided the domain into 464 segments on which we assumed constant values for the parameters. The segments are connected with the intersection conditions (16) described previously.

The collision point is at the centre of the simulation domain. This area is dedicated to provide the lowest possible gas density. The components of the vacuum chamber on both sides of the collision point are roughly symmetric: The inner triplets, with high magnetic gradients to focus the beam for the collisions; the normal-conducting separation magnets, that splits the vacuum chambers in two separate parts for each beam; the so called dispersion suppressor that is connected then to the arcs (see Fig. 14).

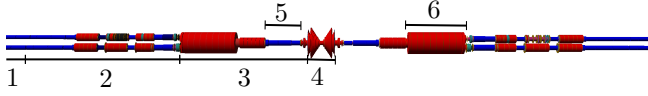


FIG. 14. Sketch of the CMS experimental area: 1: Arc, 2: Dispersion suppressor, 3: Long Straight Section, 4: CMS experimental area, 5: Inner triplet, 6: Recombination chamber

### A. Geometry and material assumption

The LHC database stores all the parameter specifications of the vacuum chamber [39–41]. For our calculations, we have extracted from the database the diameter, length and material specification, that affect the conductance, thermal outgassing and sticking probability.

#### 1. Arc

The bending arcs consist of a repetitive structure of three times 15m long chambers for dipole magnets and of shorter 6m long chambers for focusing magnets and beam instrumentation measurements. The vacuum chambers or so-called cold bores are joined by a short stainless steel bellow. The diameter of the cold bores are small about 40-60mm and additionally, a racetrack-shaped beam screen is implemented inside the chamber [30? ]. To avoid multiple reflections of the photons on the wall a so-called sawtooth surface is indented on the internal side of the beam screen, where the primary synchrotron radiation photons hit. The sawtooth profile is characterized by a reduced photon reflectivity which allows localisation of the molecular desorption and of the photoelectrons (see e-cloud effect in subsection 3). In the strong magnetic regions (as in the arcs) the cold-bores of the superconducting magnets are cooled by liquid helium at 1.9-4.5 K. They act as distributed cryogenic pumps, via the pumping slots on the beamscreen.

#### 2. Transition area

The vacuum chambers of the straight sections are generally kept at room temperature. All transitions from cryogenic to room temperature chambers happen within half a meter containing usually a valve, a vacuum module with beam instrumentation equipment and flanges at their extremities. These chambers are connected with bellows that compensate thermal expansions due to the large temperature gradients during the commissioning of the system.

#### 3. Straight Section

The vacuum chambers in the straight sections are at room temperature and are principally made out of cop-

per with an additional NEG coating, in order to reduce photon-induced desorption and the generation of secondary electrons. In between NEG coated parts, there can be short higher outgassing parts found, e.g. vacuum modules with beam instrumentation or beam collimation equipment. Collimators are often located before sensitive instruments, close to the detectors and at the end of magnet assemblies to intercept stray particles. The most critical area, the vacuum chamber in the centre of CMS, is made out of beryllium. This material has a higher radiation length than copper to provide a higher transparency to, and lower absorption of, the exotic particles resulting from the beams' collisions. Generally, the diameter in the straight section varies from 80 to 230mm. It reaches its maximum aperture in the recombination chamber, where two beam lines combine into one common chamber.

#### 4. Material properties

The realistic outgassing rates and desorption coefficients for the materials are estimated on the basis of laboratory results measured by the BVO section of the vacuum group[42] or by reference values from literature [43–45], [38, 41]. However, material treatment for ultrahigh vacuum, like vacuum firing, bake out, activation and beam-conditioning are special treatments, and therefore parameters may vary in time and from standard values in the literature.

#### 5. Beam induced parameters

During the operation, beam induced effects are the predominant factor that influence the RGP density and hence increase it by orders of magnitude. Fig. 15 shows the correlation between the dynamics of the beam energy and the readings of one specific pressure gauge.

Photon and electron induced desorption take place especially in the magnetic areas of the LHC, which present about 90% of the total accelerator.

Formula (13) implies a photon flux generated by the dipoles in the arcs of

$$\dot{\Gamma}_{ph} = \frac{1.5414 \cdot 10^{21}}{2\rho\pi} = 8.77 \cdot 10^{16} \text{ Photons}/(\text{m s}) \quad (34)$$

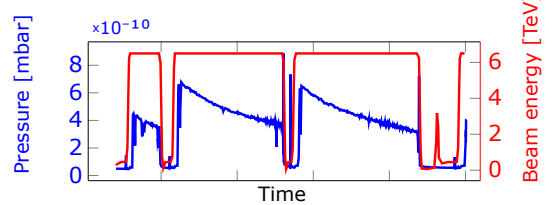


FIG. 15. Time dynamics of gauge VGI.220.1R5.X (blue curve) in the common beam chamber close to CMS from 25.09.2016 to 28.09.2016, derived from [46] and compared to the time-dynamics of the beam energy (red curve).

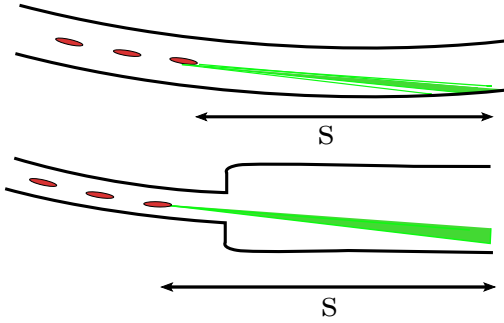


FIG. 16. Distance  $s$  between the generation of a photon and its impingement on the wall in the relativistic case.

where  $\rho = 2795.84$  m,  $I = 0.5$  A and  $E = 6.5$  TeV. Additionally, we consider that synchrotron radiation emitted by the beam travels tangentially to the orbit, deducing a spread between the location of the generation of the photons and their impingement on the chamber wall. This distance can be up to 20 meters and it depends on the geometry of the beam chamber (see Fig. 16).

This implies two consequences for the input parameters: Firstly, there may be photons impinging on the following chambers downstream of the radiation source points even if there is no magnetic field present. Thus, we must take into account a longitudinal shift of the impinging photon flux at the appropriate spot in our simulations. Secondly, a change in the geometry may cause a high spike of impinging photons, when a chamber is smaller than the previous one. Beam collimators for example provide a small variable chamber aperture to remove the beam particles in the halo and consequently are subjected to a high photon bombardment [47]. Additionally, synchrotron radiation is also produced by an off-axis beam in quadrupoles and orbit correctors. However the magnetic strength of these magnets is much less compared to the bending magnets in the arcs. The critical energy  $E_c$  for dipoles in the LHC can be estimated with 40eV, whereas the strong focusing quadrupoles before the experiments provide a maximum of 9eV.

Summarizing, the distribution of the photon flux in the arcs is characterized by a more or less continuous distribution, whereas in the straight sections it consists of distinct peaks.

The electron cloud is strongly depending on the chamber diameter, the material, bunch spacing and the beam energy and intensity.

Moreover, two beams are present in the common chambers of the LHC, that leads to a significant beam-induced density increase especially in the quadrupole triplets close to the detector.

In addition, the study of the evolution of the heat dissipation  $Q$  on the vacuum chambers may also give a hint for values of the beam induced parameters. These parameters are as well logged in [46]. It holds that:

$$Q_{\text{heat}} = Q_{\text{SR}} + Q_{\text{IC}} + Q_{\text{EC}}, \quad (35)$$

where SR refers to synchrotron radiation, IC to image current and EC to electron cloud.

## B. LHC gauges

There are a total of 98 gauges installed in the area of CMS that monitor the vacuum dynamics. The final goal now is to compare the simulation output with the readings of the installed gauges. Most of the LHC gauges are inverted-magnetron penning gauges (IKR 070, Pfeiffer), which mainly measure down to  $10^{-11}$ mbar. However for beam lifetime and radiation background reasons, the pressure in the LHC is in some parts lower than this value, and therefore they serve mainly as an alarm system that indicates potential vacuum degradation. This explains the rather high gauge reading in the NEG-coated recombination chamber in Fig. 19, located about 100 m left and right from the CMS interaction point. Bayard-Alpert ionization gauges (SVT 305) are also employed. These measure down to values of the order of  $10^{-12}$ mbar [48].

For our discussions here, we derived the gauge's readings of four very similar runs from mid-August to the end of October in 2016 indicated with a fill number of 5211, 5338, 5416 and 5451 from the LHC logging database [46]. In Fig. 17 the time evolution of the gauge VGPB.242.7L5.B is plotted for the Fill 5211 and 5338. This graphic should visualize that fills with similar parameters provide similar results. The slight difference is due to a higher monitored emittance for beam of Fill 5211. The monitored pressure value of the gauges is nitrogen equivalent and therefore the gauges' sensitivity to different gas species must be taken into account in our calculations. Unfortunately, the harsh radiation environment of the LHC tunnel does not allow the installation of residual-gas analysers and their delicate electronics.

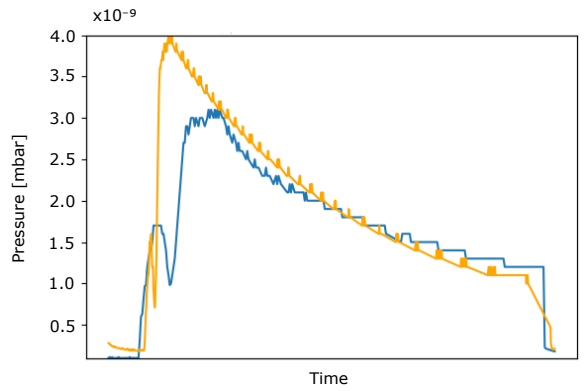


FIG. 17. Time evolution of penning gauge VGPB.242.7L5.B for Fill 5211 (orange line) and Fill 5338 (blue line).

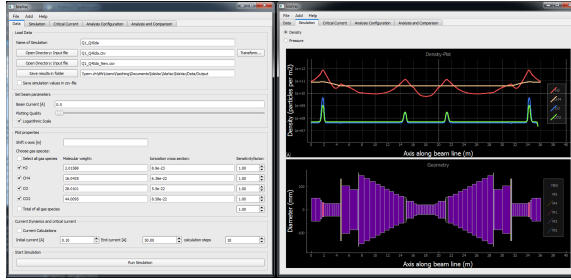


FIG. 18. Screenshot of the simulation program “PyVASCO”.

### C. Results and discussion

The RGP density in the experimental area around CMS provides many different characterizing aspects, that are visualized as our main result in Fig. 19.

We implemented the model in a Python environment and embedded it in a graphical user interface based on the library of PyQt [49–52] (see Fig. 18). Results are calculated within less than a minute.

Fig. 19 shows that the general goal is fulfilled, that the maximum density in the LHC should not exceed  $10^{15} \text{H}_2$ -equivalent gas particles per  $\text{m}^3$  in the presence of the circulating beams. The RGP density in the experimental area is even by orders of magnitude lower to minimize the background noise to the experiments. Hence, a beam lifetime in the order of 100 hours supports an efficient operation of the high energy experiments with respect to vacuum requirements.

The four different graphs in Fig. 19 represent the prevailing densities of  $\text{H}_2$ ,  $\text{CH}_4$ ,  $\text{CO}$  and  $\text{CO}_2$ . Their different shapes symbolize their different behaviours. Hydrogen constitutes the major part of the gas load. Hydrogen’s low mass and low binding energy compared to the other gas species results in a higher probability of beam induced desorption and a higher thermal outgassing of the vacuum chamber walls.

The shape of the plot of  $\text{H}_2$ ,  $\text{CO}$  and  $\text{CO}_2$  show a similar structure.  $\text{CO}$  and  $\text{CO}_2$  are of the same order of magnitude. The biggest difference of each gas specie’s value can range of three orders of magnitude.

The different materials are represented by different colours in the geometry sketch of CMS in Fig. 19. As an outline, cryogenic areas are marked in dark blue with a grey background, room temperature areas are marked in red.

The biggest density gradient can be observed in the transition areas from room temperature to cryogenic area. The following relation holds:

$$\frac{n_1}{n_2} = \sqrt{\frac{T_2}{T_1}} \quad (36)$$

This tells us that the RGP density in areas with lower temperatures is higher than in areas with higher temperatures, assuming the same material specifications. Additionally, the high density has to be related with beam

induced effects that occur mainly in the arcs. The density profile also visualizes the importance of the beam direction. The density is slightly higher, when the beam travels from the arcs to the Straight Section, because of the fact that emitted photons can travel several meters until they impinge on the wall (see Fig. 16).

The density plot for hydrogen shows some peaks in the arcs. They appear exactly at the interconnects between two vacuum chambers. In this part the liquid helium cooling pipe on the beam screen is usually absent for a few centimetres, which leads to a slight temperature rise and hence the hydrogen equilibrium density goes up.

Otherwise, cryo- and NEG pumping results in a flat line, at the equilibrium of surface pumping and degassing. Lumped pumps are only located in room-temperature areas.

Thin-film NEG coating deposited along all room-temperature chambers, capture getterable gas species such as  $\text{H}_2$ ,  $\text{CO}$  and  $\text{CO}_2$ . This configuration provides very efficient distributed surface pumping. Methane is, due to its closed-symmetric atomic structure, not reacting with the surface and is not pumped [28]. This is the main reason, why the density profile of methane is clearly different from the other gas species. Methane is only pumped by lumped ion pumps. Its pressure profile therefore resembles a parabola from one pump to the next. This can be seen very well between the quadrupoles Q4 and Q7 in Fig. 19 about 250 m right of the CMS-interaction point. It should be added that there are indications that  $\text{CH}_4$  is also pumped by beam-ionisation, and therefore if this effect is not taken into account the density curves for this gas are to be intended as worst case scenario [23]. The low RGP density in the collision area is due to the outgassing characteristics of beryllium and the extremely low photon bombardment in this area.

## VI. CONCLUSION

This article introduces a mathematical model and a computer code to calculate and efficiently forecast the residual gas particle density in a particle accelerator. This quantity should be kept as low as possible to support an efficient operation of the machine. Several effects influence it and make this requirement challenging. Among them are beam-induced effects as well as thermal outgassing, diffusion inside the chamber and interactions among the different residual gases. The idea was to combine all of them in one mathematical model which gives as output the density distribution of the four dominating gas species  $\text{H}_2$ ,  $\text{CH}_4$ ,  $\text{CO}$  and  $\text{CO}_2$  inside a beam pipe. A mass-balance equation system of second order serves this purpose. Based on mathematical theorems a solution was found and the fundamental steps to this goal have been shown.

The validation of the model was established by a cross check with the Test-Particle Monte Carlo code Molflow+, a sensitivity analysis of the ion-induced desorption term including a comparison between the single-gas and the

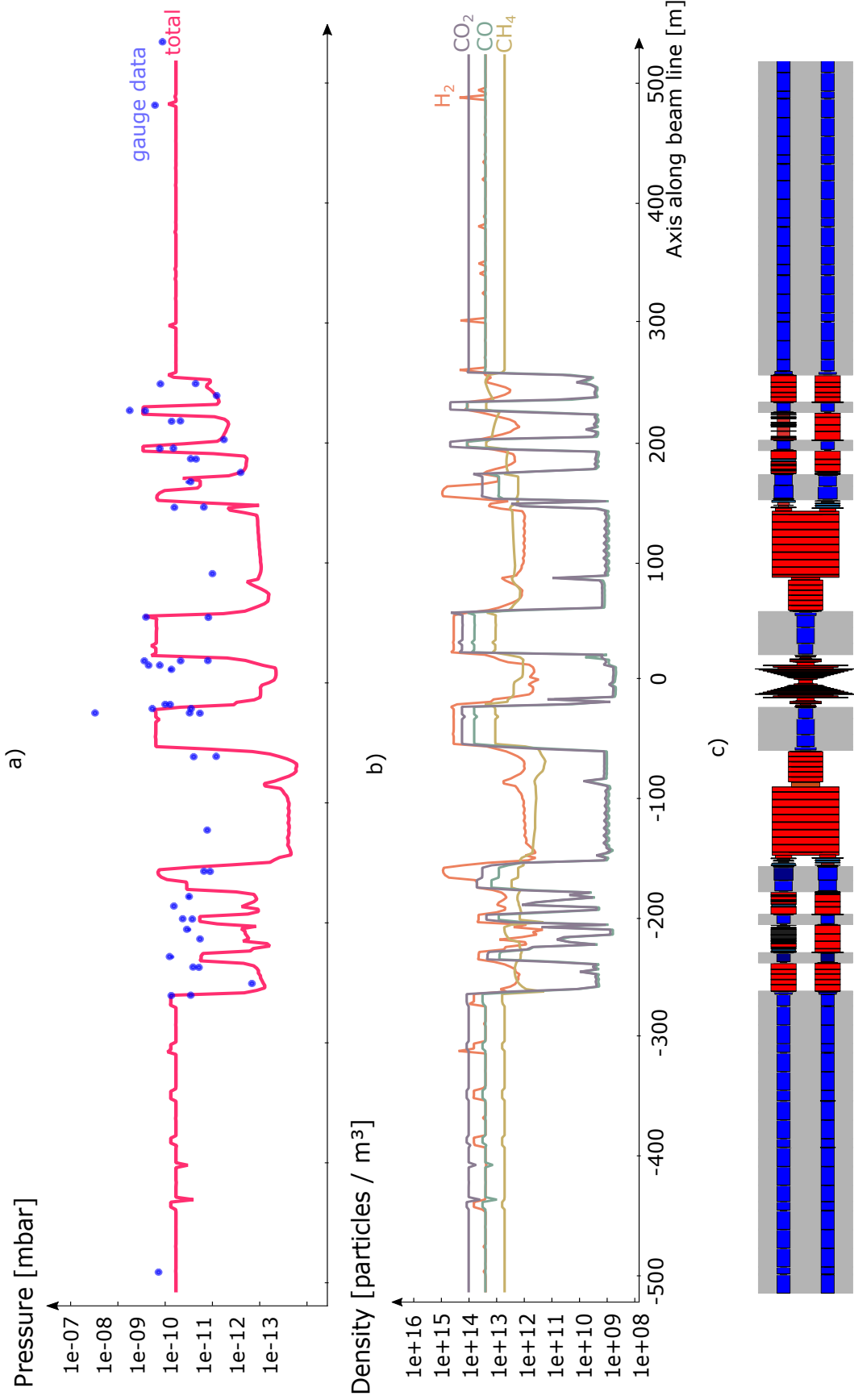


FIG. 19. Vacuum simulation of the Long Straight Section with the CMS detector located in the middle: a) total pressure plot, b) density plot of the four gas species and c) a geometry sketch.

multi-gas framework, and finally by a comparison to gauge readings in the LHC. The latter cross-check was presented for the Long Straight Section close to the CMS experiment. All these simulations show reasonably meaningful results and consequently suggest realistic replication of the vacuum environment. The knowledge on how, where and why these values influence the vacuum quality provides consequently a great aid in the design and analysis of vacuum systems. In addition, the results are computed rather fast in less than 30 seconds, even for large simulation domains.

This model provides the potential to undergo detailed parameter variation studies, hence to understand the main influencing effects at different locations and therefore to detect critical configurations in advance that could lead to vacuum degradation.

Nowadays, CERN's new challenge is to develop concepts for post-LHC circular particle colliders (FCC) [10] and the next step is to use this simulation model to present a variety of possible designs and to choose among

them, in agreement with further specifications, the best possible solution.

## ACKNOWLEDGMENTS

The discussions with Giuseppe Bregliazzzi, Josef Sestak and Vincent Baglin were most helpful to find appropriate input parameters. Many thanks as well to Jan Sopousek, who helped the authors with the implementation of the model in a Python environment and to Marton Ady, who supported the authors with Molflow+ simulations. Thanks also to Adriana Rossi for discussions about the previous model VASCO. All authors work in the Vacuum Surfaces and Coatings group at CERN. This project and its achievements are part of the global future circular collider study hosted by CERN. Ida Aichinger is a doctoral student at the Johannes Kepler University Linz, Austria, supported by the Austrian Doctoral Student Programme of CERN.

## Appendix A: Algebraic transformation of intermediate boundary condition

The value of the unknown  $y$  is posed once at the end of segment  $k-1$  and once at the beginning of segment  $k$ . For the posed solution function  $y$  by the Theorem of Picard Lindelöf, we always need to know the value of  $y$  at the beginning of each segment.

We start with the initial conditions

$$H_{k-1}y_{k-1}(x_k) - (H_k + S_k)y_k(x_k) = G_k$$

and use the identity (28) and (29), we receive:

$$\begin{aligned} H_{k-1}\left(P_{k-1}(L) \cdot y_{0(k-1)} + q_{k-1}(L)\right) - (H_k + S_k) \cdot \underbrace{\left(P_k(0) \cdot y_{0k} + q_k(0)\right)}_{=:(*)} &= G_k \\ (H_k + S_k) \cdot \left(P_k(0) \cdot y_{0k} + q_k(0)\right) &= -G_k + H_{k-1} \underbrace{\left(P_{k-1}(L) \cdot y_{0(k-1)} + q_{k-1}(L)\right)}_{=:(**)} \\ P_k(0) \cdot y_{0k} + q_k(0) &= -(H_k + S_k)^{-1}G_k + \underbrace{(H_k + S_k)^{-1}H_{k-1}}_{=:(***)} \\ y_{0k} &= -P_k^{-1}(0)(H_k + S_k)^{-1}G_k + P_k^{-1}(0) \cdot (***) - P_k^{-1}q_k(0) \\ y_{0k} &= \boxed{\begin{array}{l} \text{=:} M \in \mathbb{R}^{8 \times 8} \\ P_k^{-1}(0) \cdot (H_k + S_k)^{-1}H_{k-1}P_{k-1}(L) \end{array}} y_{0(k-1)} + \\ &\quad \boxed{\begin{array}{l} \text{=:} v \in \mathbb{R}^8 \\ -P_k^{-1}(0)(H_k + S_k)^{-1}G_k + P_k^{-1}(0) \cdot (H_k + S_k)^{-1}H_{k-1}q_{k-1}(L) - P_k^{-1}q_k(0) \end{array}} \\ &\Rightarrow \begin{pmatrix} y_{0k} \\ 1 \end{pmatrix} = \begin{pmatrix} M & | & v \\ 0 \dots 0 & | & 1 \end{pmatrix} \cdot \begin{pmatrix} y_{0(k-1)} \\ 1 \end{pmatrix} \end{aligned}$$

Some more algebraic transformations give finally:

$$\begin{aligned} y_{0k} &= \underbrace{\left[(H_k + S_k) \cdot P_k(0)\right]}_{M_2}^{-1} \cdot \underbrace{\left[H_{k-1}P_{k-1}(L) \cdot y_{0(k-1)} - \underbrace{G_k + H_{k-1}q_{k-1}(L) - (H_k + S_k) \cdot q_k(0)}_{\tilde{V}}\right]}_{M_1} \\ \begin{pmatrix} y_{0k} \\ 1 \end{pmatrix} &= \underbrace{\begin{pmatrix} M_2^{-1}M_1 & | & \tilde{V} \\ 0 \dots 0 & | & 1 \end{pmatrix}}_{=TM(k,k-1)} \cdot \begin{pmatrix} y_{0(k-1)} \\ 1 \end{pmatrix} \end{aligned}$$

- 
- [1] M. Ady and R. Kersevan, in *Proceedings of 5th International Particle Accelerator Conference* (Dresden, Germany, 2014).
- [2] A. Rossi, *VASCO (VAcuum Stability CODE): multi-gas code to calculate gas density profile in a UHV system*, Tech. Rep. (CERN, 2004).
- [3] G. Bird, *Molecular gas dynamics* (Clarendon, Oxford, 1976).
- [4] J. Lafferty, ed., *Foundations of Vacuum Science and Technology* (Wiley, 1998) p. 728.
- [5] S. G. Brush and N. S. Hall, *The Kinetic Theory Of Gases*, History of Modern Physical Sciences, Vol. 1 (Imperial College Press and distributed by World Scientific Publishing CO., 2003).
- [6] S. Harris, *An introduction to the theory of the Boltzmann equation* (Courier Corporation, 2004).
- [7] C. B. Nakhoseen and K. Jousten, *Handbook of vacuum technology* (John Wiley & Sons, 2016).
- [8] M. Ady, *Monte Carlo simulations of ultra high vacuum and synchrotron radiation for particle accelerators*, Ph.D. thesis, EPFL (2016), <https://cds.cern.ch/record/2157666>.
- [9] G. Bregliozi, G. Lanza, V. Baglin, and J. Jimenez, *Vacuum* **86**, 1682 (2012).
- [10] M. Benedikt and F. Zimmermann, *CERN Cour.* **54**, 16 (2014).
- [11] W. Kühnel, *Differential geometry*, Vol. 77 (American Mathematical Soc., 2015).
- [12] S. Chapman and T. G. Cowling, *The mathematical theory of non-uniform gases: an account of the kinetic theory of viscosity, thermal conduction and diffusion in gases* (Cambridge university press, 1970).
- [13] J. Crank, *The mathematics of diffusion* (Oxford university press, 1979).
- [14] M. Knudsen, *Annalen der Physik* **333**, 75 (1909).
- [15] R. B. Bird, W. E. Stewart, and E. N. Lightfoot, *Transport phenomena* (John Wiley & Sons, 2007).
- [16] J. Ferziger and H. Kaper, *American Journal of Physics (AAP)* **41**, 601 (1973).
- [17] A. Hofmann, *The physics of synchrotron radiation*, Vol. 20 (Cambridge University Press, 2004).
- [18] R. Bailey, G. Von Holtey, N. Hilleret, C. Bovet, M. Tavlet, J. Jimenez, M. Placidi, B. Balhan, B. Goddard, and R. Jung, in *Proceedings of the 6th European Particle Accelerator Conference* (Stockholm, Sweden, 1998).
- [19] J. Tückmantel, *Synchrotron radiation damping in LHC and longitudinal bunch shape*, Tech. Rep. (CERN, 2005).
- [20] J. Gómez-Goñi, O. Gröbner, and A. Mathewson, *Journal of Vacuum Science & Technology A: Vacuum, Surfaces, and Films (AVS)* **12**, 1714 (1994).
- [21] W. C. Turner, *Journal of Vacuum Science & Technology A: Vacuum, Surfaces, and Films (AVS)* **14**, 2026 (1996).
- [22] R. Calder, *Vacuum* **24**, 437 (1974).
- [23] A. Mathewson and S. Zhang, *Beam-gas ionisation cross sections at 7.0 TeV*, Tech. Rep. (CERN, 1996).
- [24] G. Iadarola, *Electron cloud studies for CERN particle accelerators and simulation code development*, Ph.D. thesis, Università degli Studi di Napoli Federico II, Italy (2014).
- [25] G. Iadarola and G. Rumolo, arXiv preprint arXiv:1309.6773 (2013).
- [26] B. Bradu, A. Tovar González, E. Blanco Viñuela, P. Plutecki, E. Rogez, G. Iadarola, G. Ferlin, and B. Fernández Adiego, in *7th International Particle Accelerator Conference* (Busan, Korea, 2016).
- [27] C. Benvenuti, P. Chiggiato, P. C. Pinto, A. E. Santana, T. Hedley, A. Mongelluzzo, V. Ruzinov, and I. Wevers, *Vacuum* **60**, 57 (2001).
- [28] P. Chiggiato and P. C. Pinto, *Thin Solid Films* **515**, 382 (2006).
- [29] R. A. Haefer, *Kryo-Vakuumtechnik: Grundlagen und Anwendungen* (Springer-Verlag, 2013).
- [30] P. Cruikshank, K. Artoos, F. Bertinelli, J.-C. Brunet, R. Calder, C. Campedel, I. Collins, J.-M. Dalin, B. Feral, O. Gröbner, et al., in *Particle Accelerator Conference, 1997. Proceedings of the 1997*, Vol. 3 (IEEE, 1997) pp. 3586–3588.
- [31] P.-F. Hsieh and Y. Sibuya, *Basic theory of ordinary differential equations* (Springer Science & Business Media, 2012).
- [32] E. B. Saff and A. D. Snider, *Fundamentals of Matrix Analysis with Applications* (John Wiley & Sons, 2015).
- [33] E. Picard, *Journal de Mathématiques pures et appliquées* **6**, 145 (1890).
- [34] E. Lindelöf, *Journal de Mathématiques Pures et Appliquées* **10**, 117 (1894).
- [35] E. Lindelöf, *Journal de Mathématiques Pures et Appliquées* **6**, 423 (1900).
- [36] Y. Saad, *Iterative methods for sparse linear systems* (SIAM, 2003).
- [37] A. Bonucci, A. Conte, P. Manini, and S. Raimondi, in *AIP Conference Proceedings*, Vol. 879 (AIP, 2007) pp. 432–435.
- [38] U.S. Department of Commerce, “NIST - national institute of standards and technology,” <https://www.nist.gov> (2015).
- [39] “CERN Layout Database,” <https://layout.web.cern.ch> (Accessed in: 2016), sector 45, sector 56.
- [40] “CDD - CERN Drawings Database,” <http://edms-service.web.cern.ch/edms-service/CDD> (Accessed: in 2016), sector 45, sector 56.
- [41] O. Brüning, S. Oliver, P. Collier, P. Lebrun, S. Myers, R. Ostojic, J. Poole, and P. Proudlock, eds., “LHC Design Report,” (CERN, Geneva, Switzerland, 2004) Chap. 12.
- [42] G. Bregliozi, personal communication (2015-2017).
- [43] P. Chiggiato, arXiv preprint arXiv:1404.0960 (2014).
- [44] V. Baglin, C. Grünhagel, I. Collins, O. Gröbner, and B. Jenninger, in *EPAC 2002* (Paris, France, 2002).
- [45] V. Baglin, G. Bregliozi, and R. Kersevan, in *5th International Particle Accelerator Conference* (Dresden, Germany, 2014).
- [46] “LHC logging database extracted via TIMBER v6.3.17,” <https://timber.cern.ch/> (Accessed: in 2016).
- [47] G. Valentino, R. Aßmann, R. Bruce, F. Burkart, V. Previtali, S. Redaelli, B. Salvachua, G. Stancari, and A. Valishev, *Physical Review Special Topics-Accelerators and Beams* **16**, 021003 (2013).
- [48] G. Pigny, N. Chatzigeorgiou, F. Antoniotti, H. Pereira, J.-P. Boivin, J. Gama, P. Krakowski, and P. Gomes, in *15th International Conference on Accelerator and Large Experimental Physics Control Systems* (Melbourne, Australia, 2015).

- [49] B. A. Meier, *Python GUI Programming Cookbook* (Packt Publishing Ltd, 2015).
- [50] M. Newman, *Computational physics* (CreateSpace Independent Publ., 2013).
- [51] M. Lutz, *Learning Python: Powerful Object-Oriented Programming* (O'Reilly Media, Inc., 2013).
- [52] C. Hill, *Learning scientific programming with Python* (Cambridge University Press, 2016).



---

## **Paper 2: Sets of Bounded Remainder for the Billiard on a Square**

---

submitted to "Journal of Uniform Distribution Theory".

# Sets of Bounded Remainder for the Billiard on a Square

IDA AICHINGER\* AND GERHARD LARCHER\*\*

October 18, 2016

## Abstract

We study sets of bounded remainder for the billiard on the unit square. In particular, we note that every convex set  $S$  whose boundary is twice continuously differentiable with positive curvature at every point, is a bounded remainder set for almost all starting angles  $\alpha$  and every starting point  $\mathbf{x}$ . We show that this assertion for a large class of sets does not hold for *all* irrational starting angles  $\alpha$ .

**Keywords:** Bounded remainder set, billiard path, discrepancy, distribution modulo 1, unfolding-technique.

## 1 Introduction and Statement of results

In this paper we will be concerned with bounded remainder sets for the two-dimensional billiard on the unit-square  $I^2 = [0, 1]^2$ .

**Definition 1.** Let  $\mathbf{x} = (x_1, x_2) \in I^2$  and let  $\alpha \in \mathbb{R} \setminus \mathbb{Q}$ . We say that the function  $Y : [0, \infty) \rightarrow I^2$  defined by

$$Y(t) = \left( 2 \cdot \left\| \frac{x_1 + t}{2} \right\|, 2 \cdot \left\| \frac{x_2 + \alpha t}{2} \right\| \right) \quad 0 \leq t < \infty, \quad (1)$$

where  $\|z\| := \min_{a \in \mathbb{Z}} |z - a|$ , is the two-dimensional billiard with starting slope  $\alpha$  and starting point  $\mathbf{x}$ .

---

\*The first author is supported by CERN, European Organization for Nuclear Research, Geneva, as part of the Austrian Doctoral Student Programme.

\*\*The second author is supported by the Austrian Science Fund (FWF): Project F5507-N26, which is part of the Special Research Program "Quasi-Monte Carlo Methods: Theory and Applications".

It is easily checked that this definition indeed coincides with our image of a real billiard-path in the unit interval.

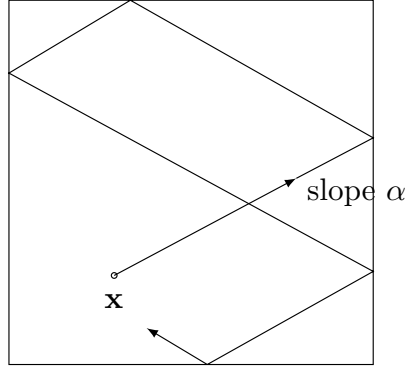


Figure 1

**Definition 2.** Let  $S \subset I^2$  be an arbitrary measurable subset of the unit square with Lebesgue measure  $\lambda(S)$ . We say that  $S$  is a bounded remainder set for the two-dimensional billiard with starting slope  $\alpha$  and starting point  $\mathbf{x} = (x_1, x_2) \in I^2$  if the distribution error

$$\Delta_T^Y(S, \alpha, \mathbf{x}) = \int_0^T \chi_S(Y(t)) dt - T\lambda(S) \quad (2)$$

is uniformly bounded for all  $T > 0$ . Here,  $\chi_S$  denotes the characteristic function for the set  $S$ .

Distribution properties for continuous motions in an  $s$ -dimensional unit cube were studied for example by Drmota in [3] (see also [4] or [7]) and quite recently by Beck [1]. Beck ([1], [2]) especially studied continuous irrational rotations and billiard paths.

For the two-dimensional billiard path for example he showed the following surprising result:

**Theorem.** (Beck) Let  $S \subseteq I^2$  be an arbitrary Lebesgue measurable set in the unit square with positive measure. Then for every  $\epsilon > 0$ , almost all  $\alpha > 0$  and every starting point  $\mathbf{x} = (x_1, x_2) \in I^2$  we have

$$\Delta_T^Y(S, \alpha, \mathbf{x}) = \mathcal{O}\left((\log T)^{3+\epsilon}\right). \quad (3)$$

As pointed out by Beck, the poly-logarithmic error term is shockingly small compared to the linear term  $T\lambda(S)$ . Moreover, it holds for *all* measurable sets  $S$ .

It is thus natural to ask if imposing certain regularity conditions on  $S$  could give an even lower bound on the error term.

We will show in the following that the estimate of Beck indeed can be significantly improved for a large collection of sets  $S$ . We show:

**Theorem 1.**

- a) *For almost all  $\alpha > 0$  and every  $\mathbf{x} \in I^2$ , every polygon  $S \subset I^2$  with no edge of slope  $\alpha$  or  $-\alpha$  is a bounded remainder set for the two-dimensional billiard with starting slope  $\alpha$  and starting point  $\mathbf{x}$ .*
- b) *For almost all  $\alpha > 0$  and every  $\mathbf{x} = (x_1, x_2) \in I^2$ , every convex set  $S \subset I^2$  whose boundary  $\partial S$  is a twice continuously differentiable curve with positive curvature at every point is a bounded remainder set for the two-dimensional billiard with starting slope  $\alpha$  and starting point  $\mathbf{x}$ .*

We will see in the proofs of these results that this Theorem easily follows from an analogous result shown in [5] for the continuous irrational rotation  $X(t) := (\{x_1 + t\}, \{x_2 + \alpha t\})_{t \geq 0}$ , and by the “unfolding-technique” suggested by Beck in [2].

It is obvious that the results given in Theorem 1 do not hold for a rational slope  $\alpha$ .

However one could ask whether the results can be improved first by omitting the condition on the slopes of the edges of the polygon  $S$  in part a) of the Theorem and, second, whether both results maybe are valid even for *all* irrational slopes  $\alpha$ .

We will give an easy argument that indeed the condition on the slopes of the edges cannot be omitted in general. Moreover, we will prove - and this will be the main effort in this paper - that the results of Theorem 1a and 1b in general do not hold for *all* irrational  $\alpha$ .

I.e., we will show:

**Theorem 2.**

- a) *For every  $\alpha > 0$  there is a polygon  $S$  with an edge of slope  $\alpha$  or  $-\alpha$  such that  $S$  is not a bounded remainder set for the billiard with starting-slope  $\alpha$  and for any starting point  $\mathbf{x}$ .*
- b) *For every  $\mathbf{m} \in [0, 1]^2$  there are uncountably many radii  $r$ , dense in an interval of positive length, such that there is a slope  $\alpha$  and a starting point  $\mathbf{x}$  such that the disk with midpoint  $\mathbf{m}$  and radius  $r$  is not a set*

*of bounded remainder with respect to the billiard with starting slope  $\alpha$  and starting point  $x$ .*

In Chapter 2 we prove Theorem 1 and Theorem 2a. In Chapter 3 we carry out the main work, namely the proof of Theorem 2b.

## 2 Proofs of Theorem 1 and of Theorem 2a

The proofs of these two results can be traced back to the results given in [5] via the technique of unfolding.

As was pointed out in detail for example by Beck in [2] the technique of “unfolding” a billiard path ( see Figure 2 )

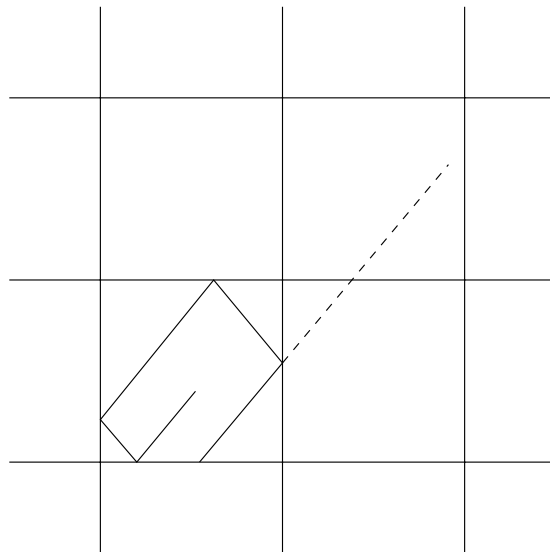


Figure 2

shows that the problem of uniformity of a billiard path in the unit square with respect to a given test set  $S$  is equivalent to the problem of uniformity of the corresponding continuous rotation in the  $2 \times 2$  square, where each one of the four unit-subsquares contains a reflected copy of the given test set (see  $S_1, S_2, S_3, S_4$  in Figure 3) Of course this again can be reduced to the problem of studying continuous irrational rotation in  $[0, 1]^2$  with respect to a factor  $1/2$  reduced versions of  $S_1, S_2, S_3, S_4$ .

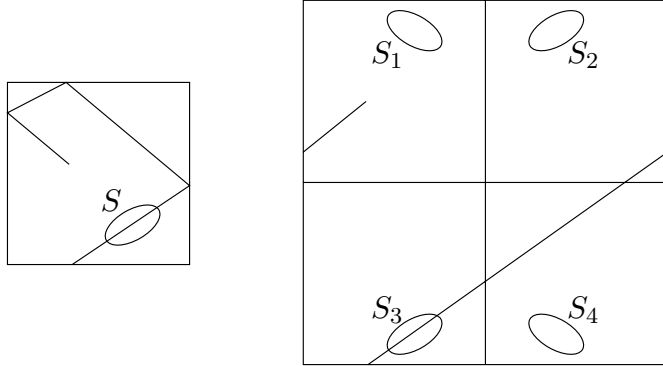


Figure 3

So in all the following, when studying the distribution error  $\Delta_T^Y(S, \alpha, \mathbf{x})$  for the two-dimensional billiard this task can be traced back to the investigation of the distribution error  $\Delta_T^X(\tilde{S}, \alpha, \mathbf{x})$  for the continuous irrational rotation where  $\tilde{S}$  consists of four mirrored and by a factor  $1/2$  reduced copies of  $S$  lying symmetrical to  $(1/2, 1/2)$ .

*Proof of Theorem 1.*

Theorem 1 follows immediately from the above considerations on the unfolding technique and from Theorem 1 and Theorem 2 in [5].  $\square$

*Proof of Theorem 2a.*

Let  $\alpha > 0$  be given. Consider first a triangle  $S$  (see Figure 4) with corners in  $(a, 1)$ ,  $(1, 1 - a\alpha)$ ,  $(1, 1)$ , where  $a$  is such that  $0 < a\alpha < 1$  and such that  $a \neq \frac{1}{\alpha}\{k\alpha\}$  for all  $k \in \mathbb{N}$ .

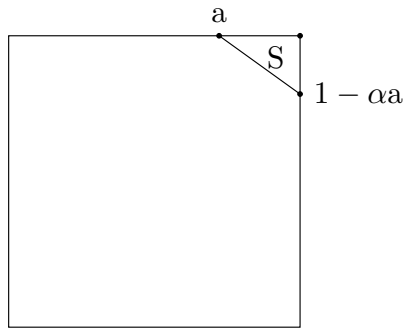


Figure 4

So one side of  $S$  has slope  $-\alpha$ . Unfolding leads to the investigation of

the continuous irrational rotation with slope  $\alpha$  with respect to the parallelogram  $\tilde{S}$  ( see Figure 5 ) with corners in

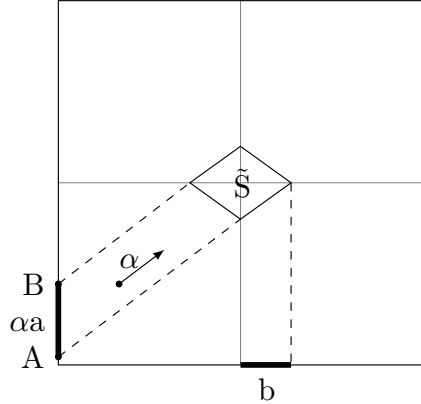


Figure 5

$$\left(\frac{1}{2}, \frac{a}{2}\right), \left(\frac{1}{2}, \frac{1+\alpha a}{2}\right), \left(\frac{1}{2} + \frac{a}{2}, \frac{1}{2}\right), \left(\frac{1}{2}, \frac{1-\alpha a}{2}\right).$$

Note that two sides of  $\tilde{S}$  have slope  $\alpha$ , the other two have slope  $-\alpha$ . The length of the interval  $[A, B]$  is  $a\alpha \neq \{k\alpha\}$  for all  $k \in \mathbb{N}$ . We show that for no starting point  $\mathbf{x}$  the set  $\tilde{S}$  is of bounded remainder for the irrational continuous rotation with slope  $\alpha$ . Hence the set  $S$  is not of bounded remainder for the billiard with starting slope  $\alpha$  (and any starting point  $\mathbf{x}$ ).

Indeed, it is easy to see that for this set  $\tilde{S}$  we have

$$\left| \int_0^T \chi_{\tilde{S}}(\{t\}, \{\alpha t\}) dt - b \cdot \sum_{n=1}^{[T]} \chi_{[A,B]}(\{n\alpha\}) \right| \leq 1.$$

It was shown by Kesten in [6] that

$$\left| \sum_{n=1}^{[T]} \chi_{[A,B]}(\{n\alpha\}) - a\alpha \cdot [T] \right|$$

is unbounded since  $B - A = a\alpha \neq \{k\alpha\}$  for all  $k \in \mathbb{N}$ . Hence (note that  $\lambda(\tilde{S}) = a\alpha \cdot b$ )

$$\left| \int_0^T \chi_{\tilde{S}}(\{t\}, \{\alpha t\}) dt - T \cdot \lambda(\tilde{S}) \right|$$

is unbounded. □

### 3 Proof of Theorem 2b

The proof of Theorem 2b will need the most work. We start with some auxiliary results. Especially we will have to deal with functions of the form

$$g_m(x) := \frac{1}{2m} \sum_{k=0}^{2m-1} \sqrt{1 - (1 - \frac{k}{m} - x)^2} \quad (4)$$

for  $x \in [0, \frac{1}{m}]$ , where  $m$  is a given positive integer. The function  $g_m$  is illustrated in Figure 6.

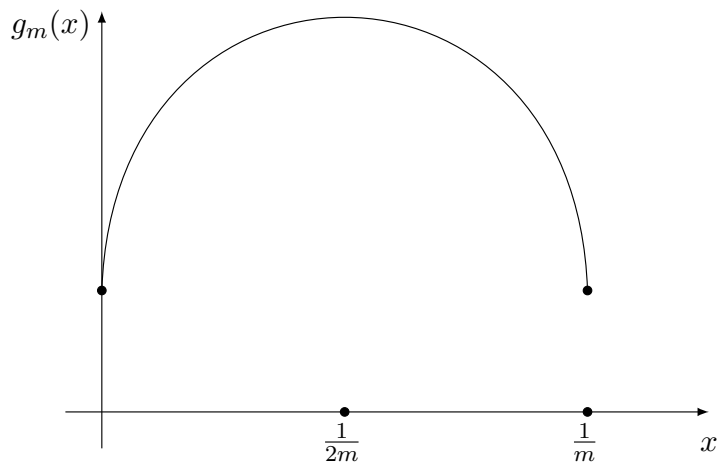


Figure 6

Let now  $m$  be fixed, and  $h_m(x) := g_m(x) - g_m(0)$ . It is easy to see that  $h_m(0) = h_m(\frac{1}{m}) = 0$ ,  $h_m$  is arbitrarily often differentiable on  $(0, \frac{1}{m})$ , continuous on  $[0, \frac{1}{m}]$ , symmetric around  $\frac{1}{2m}$  and strictly convex on  $[0, \frac{1}{m}]$ .

Further we have

**Lemma 1.**

- a) There exist  $c', c''$  with  $0 < c' < c''$  such that for all  $m$  large enough we have

$$c' \cdot \frac{1}{m^{3/2}} < h_m\left(\frac{1}{2m}\right) < c'' \cdot \frac{1}{m^{3/2}}. \quad (5)$$

- b) There exists  $c''' > 0$  such that

$$h_m(x) \geq c''' \cdot \frac{1}{m} \sqrt{x} \quad (6)$$

for all  $x \in [0, \frac{1}{2m}]$ .

*Proof.* This is shown by some tedious but elementary analysis. We do not give all details but just give two hints:

To prepare part a) note that

$$\begin{aligned} h_m(x) &= g_m(x) - g_m(0) = \\ &= \frac{1}{2m} \sum_{k=0}^{2m-1} \left( \sqrt{1 - \left(1 - \frac{k}{m} - x\right)^2} - \sqrt{1 - \left(1 - \frac{k}{m}\right)^2} \right) \\ &= \frac{1}{2m} \sum_{k=0}^m \left( \sqrt{1 - \left(1 - \frac{k}{m} - x\right)^2} - \sqrt{1 - \left(1 - \frac{k}{m}\right)^2} \right. \\ &\quad \left. + \sqrt{1 - \left(1 - \frac{2m-1-k}{m} - x\right)^2} - \sqrt{1 - \left(1 - \frac{2m-1-k}{m}\right)^2} \right) \\ &=: \frac{1}{2m} \sum_{k=0}^m w_m(k, x) \end{aligned}$$

and note that simple calculation shows that for  $k \geq 0$  there are absolute constants  $c'_1, c'_2 > 0$  such that

$$c'_1 \cdot \frac{1}{m^{1/2} \max(k, 1)^{3/2}} \leq w_m(k, \frac{1}{2m}) \leq c'_2 \cdot \frac{1}{m^{1/2} \max(k, 1)^{3/2}}$$

always.

To show part b, note that for  $x$  small, only the first summand of  $h_m$ , i.e., the summand for  $k=0$ ,

$$\frac{1}{m} \sqrt{1 - (1-x)^2} \sim \frac{1}{m} \sqrt{x}$$

is of relevance.

□

### **Lemma 2.**

a) *There exists  $c_1 > 0$  such that*

$$|h'_m(x)| \leq c_1 \cdot \frac{1}{\sqrt{m}} \quad (7)$$

*for all  $x \in [\frac{1}{10m}, \frac{9}{10m}]$  and all  $m$  large enough.*

*Especially it holds that*

$$h'_m(x) \geq -c_1 \cdot \frac{1}{\sqrt{m}} \quad (8)$$

*for all  $x \in [0, \frac{9}{10m}]$ .*

b) *There exists  $c_2 > 0$  such that for all  $m$  large enough we have*

$$h'_m(x) \geq 5c_1 \frac{1}{\sqrt{m}} \quad (9)$$

*for all  $x \in (0, c_2 \frac{1}{m})$ .*

*(Here  $c_1$  is the constant from part a.).*

*Proof.* This follows immediately from Lemma 1 and the convexity of  $h_m$ . □

Let  $m$  large enough be fixed. Moreover in the following let  $a, b, c$  be given reals with  $0 \leq a \leq b \leq c < \frac{1}{m}$ , and

$$\begin{aligned} G_m(x) := & g_m(x) + g_m((x+a) \bmod \frac{1}{m}) \\ & + g_m((x+b) \bmod \frac{1}{m}) + g_m((x+c) \bmod \frac{1}{m}) \end{aligned}$$

Then we have:

**Lemma 3.** *There are  $c_3, c_4 > 0$  such that for all  $m$  large enough and all  $a, b, c$  as above there is an  $x_0 \in \{0, a, b, c\}$  such that  $G_m$  is strictly increasing on  $[x_0, x_0 + c_4 \cdot \frac{1}{m}]$  and*

$$G_m(x_0 + c_4 \cdot \frac{1}{3m}) - G_m(x_0) > c_3 \cdot \frac{1}{m^{3/2}} \quad (10)$$

$$G_m(x_0 + c_4 \cdot \frac{2}{3m}) - G_m(x_0 + c_2 \cdot \frac{1}{3m}) > c_3 \cdot \frac{1}{m^{3/2}} \quad (11)$$

$$G_m(x_0 + c_4 \cdot \frac{1}{m}) - G_m(x_0 + c_2 \cdot \frac{2}{3m}) > c_3 \cdot \frac{1}{m^{3/2}}. \quad (12)$$

*Proof.* At least one of the following relations holds:

$$c < \frac{4}{5m} \quad \text{or} \quad b < c - \frac{1}{5m}, \quad \text{or} \quad a < b - \frac{1}{5m}, \quad \text{or} \quad a > \frac{1}{5m}.$$

Assume for example that  $c < \frac{4}{5m}$  holds (the other cases are treated quite analogously). Then set  $x_0 = 0$ . Let  $c_4 := \min(c_2, \frac{1}{10})$  where  $c_2$  is like in Lemma 2 b). Then for any  $x \in [0, c_4 \frac{1}{m}]$  it holds that:

$$(a+x) \bmod \frac{1}{m}, \quad \text{and} \quad (b+x) \bmod \frac{1}{m}, \quad \text{and} \quad (c+x) \bmod \frac{1}{m}$$

are all in  $[0, \frac{9}{10m})$ :

Hence by Lemma 2a) we have that  $g'_m$  at these places is at least  $-c_1 \cdot \frac{1}{\sqrt{m}}$ . By Lemma 2b) for  $x \in [0, c_4 \frac{1}{m}]$  we have  $g'_m(x) \geq 5c_1 \cdot \frac{1}{\sqrt{m}}$  and hence  $G'_m(x) \geq 2c_1 \frac{1}{\sqrt{m}}$  for all those  $x$ .

From this the assertions of Lemma 3 immediately follow.  $\square$

**Lemma 4.** *For all  $m$  large enough there is a sub-interval  $\Lambda_m$  of  $[0, \frac{1}{m}]$  of length at least  $\frac{c_4}{3} \cdot \frac{1}{m}$  such that either*

$$G_m(x) > 2 \int_0^2 \sqrt{1 - (1-y)^2} dy + \frac{c_3}{2m^{3/2}} = \pi + \frac{c_3}{2m^{3/2}} \quad (13)$$

or

$$G_m(x) < 2 \int_0^2 \sqrt{1 - (1-y)^2} dy - \frac{c_3}{2m^{3/2}} = \pi - \frac{c_3}{2m^{3/2}} \quad (14)$$

holds for all  $x \in \Lambda_m$ .

*Proof.* This follows immediately from Lemma 3.  $\square$

*Proof of Theorem 2b.* For the proof we proceed in analogy to the proof of Theorem 1.7b in [5] where the corresponding result was shown for the continuous irrational rotation, and in the following we sometimes refer to this proof.

Fix an irrational  $\alpha \in (\frac{1}{8}, \frac{1}{4})$  with continued fraction expansion  $\alpha = [0; a_1, a_2, \dots]$  and convergents  $\frac{p_n}{q_n}$  satisfying  $a_{l+1} > q_l^{100}$  and  $p_l$  even, for infinitely many  $l$ . There exist uncountably many such  $\alpha$ . Let  $S$  be a disk with diameter  $d := 2\alpha/\sqrt{1 + \alpha^2}$ . (Note that the set of  $\alpha$  with the above properties is dense in  $(\frac{1}{8}, \frac{1}{4})$ , hence the set of diameters  $d$  is dense in  $(\frac{2}{\sqrt{65}}, \frac{2}{\sqrt{17}})$ .)

Studying the billiard path with respect to  $S$  means to study the continuous rotation with respect to four copies of  $S$  with diameter  $\alpha/\sqrt{1 + \alpha^2}$  each (see Figure 7)

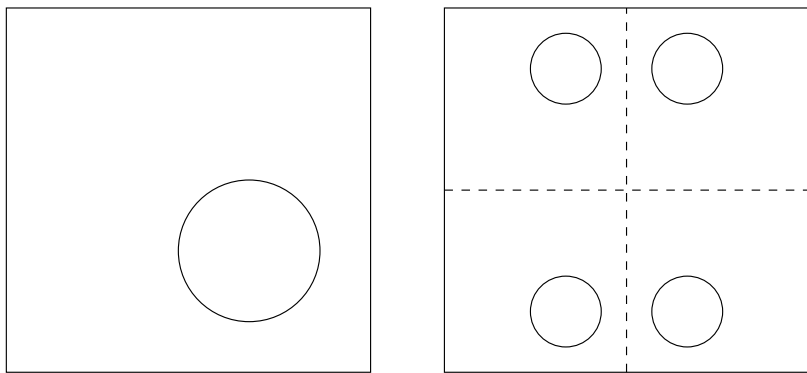


Figure 7

For such  $\alpha$  and one copy of such disks it was shown in Theorem 1.7b in [5] that the continuous rotation is not of bounded remainder for all starting points  $\mathbf{x}$ .

In the proof of this Theorem the result was shown by studying the function  $g_m$  as defined in this current paper at the beginning of Section 3 (in [5] our  $g_m$  is denoted by  $G_m$ ), and it was shown that the validity of the result of Theorem 1.7b in [5] is due to the fact that for every  $m$  there exists a subinterval  $\Lambda_m \subseteq [0, \frac{1}{2m}]$  of length at least  $\frac{1}{6m}$  such that either

$$g_m(x) > \frac{1}{2} \int_0^2 \sqrt{1 - (1-y)^2} dy + \frac{\tilde{c}}{m^{3/2}} = \frac{\pi}{4} + \frac{\tilde{c}}{m^{3/2}} \quad (15)$$

or

$$g_m(x) < \frac{1}{2} \int_0^2 \sqrt{1 - (1-y)^2} dy - \frac{\tilde{c}}{m^{3/2}} = \frac{\pi}{4} - \frac{\tilde{c}}{m^{3/2}} \quad (16)$$

holds for an absolute constant  $\tilde{c} > 0$  and all  $x \in \Lambda_m$ .

By following the proof of Theorem 1.7b in [5] it becomes obvious that studying now four copies of disks instead of one copy means to study

$$g_m(x) + g_m\left((x+a)\text{mod}\frac{1}{m}\right) + g_m\left((x+b)\text{mod}\frac{1}{m}\right) + g_m\left((x+c)\text{mod}\frac{1}{m}\right),$$

for some  $a, b, c$ , i.e., to study the function  $G_m$  as studied in Lemma 3 and Lemma 4 of the current paper. In Lemma 4 it was shown that for  $G_m$  an analogous property (independent of the choices for  $a, b$ , and  $c$ ) holds as stated above for  $g_m$ .

Again by following the proof of Theorem 1.7b in [5] it is obvious that from this property for  $G_m$  (Lemma 4) the result of our Theorem 2b follows.

□

## References

- [1] J. Beck. *From Khinchin's conjecture on strong uniformity to superuniform motions*. Mathematika **61** (2015), 591–707.
- [2] J. Beck. *Strong uniformity*. Radon Series on Computational and Applied Mathematics **15**, Uniform Distribution and Quasi-Monte Carlo Methods, 17–44, De Gruyter, Berlin, 2014.
- [3] M. Drmota. *Irregularities of continuous distributions*. Ann. Inst. Fourier **39** (1989), 501–527.
- [4] M. Drmota, R. Tichy. *Sequences, Discrepancies and Applications*. Springer Lecture Notes in Mathematics 1651, Springer, 1997.
- [5] S. Grepstad, G. Larcher. *Sets of bounded remainder for the continuous irrational rotation on  $[0, 1]^2$* . Acta Arith., to appear, 2016, available at [arXiv:1603.00207](https://arxiv.org/abs/1603.00207)

- [6] H. Kesten. *On a conjecture of Erdős and Szüsz related to uniform distribution mod 1.* Acta Arith. **12** (1966), 193-212.
- [7] L. Kuipers, H. Niederreiter. *Uniform distribution of sequences.* Wiley, New York, 1974.

**Authors address:**

CERN, EUROPEAN ORGANIZATION FOR NUCLEAR RESEARCH,  
385 ROUTE DE MEYRIN, CH-1217 MEYRIN, SWITZERLAND.  
*E-mail address:* ida.aichinger@cern.ch

INSTITUTE OF FINANCIAL MATHEMATICS AND APPLIED NUMBER THEORY,  
JOHANNES KEPLER UNIVERSITY LINZ, ALtenbergerst. 69, A-4040 LINZ,  
AUSTRIA.

*E-mail address:* gerhard.larcher@jku.at

---

## **Paper 3: On Quasi-energy-spectra, pair correlations of sequences and additive combinatorics**

---

submitted to "Ian Sloan's 80th birthday festschrift", published by Springer Verlag, accepted in June 2017.

# ON QUASI-ENERGY-SPECTRA, PAIR CORRELATIONS OF SEQUENCES AND ADDITIVE COMBINATORICS

Ida Aichinger, Christoph Aistleitner, and Gerhard Larcher

**Abstract** The investigation of the pair correlation statistics of sequences was initially motivated by questions concerning quasi-energy-spectra of quantum systems. However, the subject has been developed far beyond its roots in mathematical physics, and many challenging number-theoretic questions on the distribution of the pair correlations of certain sequences are still open. We give a short introduction into the subject, recall some known results and open problems, and in particular explain the recently established connection between the distribution of pair correlations of sequences on the torus and certain concepts from additive combinatorics. Furthermore, we slightly improve a result recently given by Jean Bourgain in [1].

## 1 INTRODUCTION

Some of Ian Sloan's first published papers dealt with topics from mathematical physics, in particular with theoretical nuclear physics. Later he moved his area of research to applied mathematics and numerical analysis, and in particular Ian's ground-breaking work on complexity theory, numerical integration and mathematical simulation is well-known and highly respected among the scientific community

---

Ida Aichinger  
CERN, European Organization for Nuclear Research, 385 Route de Meyrin, CH-1217 Meyrin,  
Switzerland  
e-mail: ida.aichinger@cern.ch

Christoph Aistleitner  
TU Graz, Institute for Analysis and Number Theory, Steyrergasse 30, 8010 Graz, Austria  
e-mail: aistleitner@math.tugraz.at

Gerhard Larcher  
Johannes Kepler University Linz, Institute for Financial Mathematics and Applied Number Theory,  
Altenbergerstraße 69, 4040 Linz, Austria  
e-mail: gerhard.larcher@jku.at

of mathematicians. The techniques developed and analyzed by Ian in these fields are often based on the use of deterministic point sets and sequences with certain “nice” distribution properties, a method which is nowadays widely known under the name of *quasi-Monte Carlo method* (QMC). In the present paper we will combine these two topics, mathematical physics and the distribution of point sets.

Ian’s first research paper appeared 1964 in the Proceedings of the Royal Society (London), entitled “The method of polarized orbitals for the elastic scattering of slow electrons by ionized helium and atomic hydrogen” [24]. In the same journal, but thirteen years later, Berry and Tabor published a groundbreaking paper on “Level clustering in the regular spectrum” [4]. This paper deals with the investigation of conservative quantum systems that are chaotic in the classical limit. More precisely, the paper deals with statistical properties of the energy spectra of these quantum systems, and Berry and Tabor conjectured that for the distribution function of the spacings between neighboring levels of a generic integrable quantum system the exponential Poisson law holds. That means, roughly speaking, the following.

Let  $H$  be the Hamiltonian of a quantum system and let  $\lambda_1 \leq \lambda_2 \leq \dots$  be its discrete energy spectrum. We call the numbers  $\lambda_i$  the *levels* of this energy spectrum. If it is assumed that

$$\#\{i : \lambda_i \leq x\} \sim cx^\gamma$$

for  $x \rightarrow \infty$  and some constants  $c > 0$ ,  $\gamma \geq 1$ , then consider  $X_i := c\lambda_i^\gamma$ . The Berry–Tabor conjecture now states that if the Hamiltonian is classically integrable and “generic”, then the  $X_i$  have the same local statistical properties as independent random variables coming from a Poisson process. Here the word “generic” is a bit vague; it essentially means that one excludes the known obvious (and less obvious) counterexamples to the conjecture. For more material on energy spectra of quantum systems and the following two concrete examples see the original paper of Berry and Tabor [4] as well as [5, 9, 16] and Chapter 2 in [7]. For a survey on the Berry–Tabor conjecture see [17].

Two basic examples of quantum systems are the two-dimensional “harmonic oscillator” with Hamiltonian

$$H = p_x^2 + p_y^2 + w^2(x^2 + y^2)$$

and the “boxed oscillator”. This is a particle constrained by a box in  $x$ -direction and by a harmonic potential in  $y$ -direction; the Hamiltonian in this case is given by

$$H = -p_x^2 - p_y^2 + w^2y^2.$$

The investigation of the distribution of the energy levels in these two examples leads to the investigation of the pair correlation statistics of certain sequences  $(\theta_n)_{n \geq 1}$  in the unit interval. More specifically, one is led to study the pair correlations of the sequence  $(\{n\alpha\})_{n \geq 1}$  in the case of the 2-dimensional harmonic oscillator, and the

pair correlations of the sequence  $(\{n^2\alpha\})_{n \geq 1}$  in the case of the boxed oscillator; here, and in the sequel, we write  $\{\cdot\}$  for the fractional part function. In particular, for these sequences one is led to study the quantity  $R_2$ , which is introduced below.

Let  $(\theta_n)_{n \geq 1}$  be a sequence of real numbers in  $[0, 1]$ , and let  $\|\cdot\|$  denote the distance to the nearest integer. For every interval  $[-s, s]$  we set

$$R_2([-s, s], (\theta_n)_{n \geq 1}, N) = \frac{1}{N} \# \left\{ 1 \leq j \neq k \leq N : \|\theta_j - \theta_k\| \leq \frac{s}{N} \right\}.$$

The subscript “2” of “ $R_2$ ” refers to the fact that these are the *pair* correlations, that is, the correlations of order 2 – in contrast to triple correlations or correlations of even higher order. Note that the average spacing between two consecutive elements of  $\{\theta_1, \dots, \theta_N\}$  (understood as a point set on the torus) is  $1/N$ , and thus for an “evenly distributed” point set one would expect to find roughly  $2s$  other points within distance  $[-s/N, s/N]$  around a given point  $\theta_j$ , causing  $R_2([-s, s], (\theta_n)_{n \geq 1}, N)$  to be approximately  $2s$  for such a point set (after summing over all elements of the point set and then normalizing with division by  $N$ ). Actually, for a sequence of independent,  $[0, 1]$ -uniformly distributed random variables  $\theta_1, \theta_2, \dots$  one can easily show that for every  $s \geq 0$  we have

$$R_2([-s, s], (\theta_n)_{n \geq 1}, N) \rightarrow 2s,$$

almost surely. If this asymptotic relation holds for the distribution of pair correlations of a certain sequence we say that the distribution of the pair correlations is asymptotically *Poissonian*. Informally speaking, a sequence whose distribution of the pair correlations is asymptotically Poissonian may be seen as a sequence showing “random” behavior, and the investigation of the asymptotic distribution of the pair correlations of a deterministic sequence may be seen as studying the pseudorandomness properties of this sequence.

The systematic investigation of the asymptotic distribution of the pair correlation of sequences on the torus (motivated by the applications in quantum physics) was started by Rudnick and Sarnak in [20] for the case of sequences of the form  $(\{n^d\alpha\})_{n \geq 1}$  for integers  $d \geq 1$ . In the case  $d = 1$ , the distribution of the pair correlations is *not* asymptotically Poissonian (independent of the value of  $\alpha$ ); this was remarked for example in [20] with a hint to the well-known *Three Distance Theorem*, which goes back to Świerczkowski and Sós [25]. For  $d \geq 2$  the distribution of the pair correlations is asymptotically Poissonian for almost all  $\alpha$ , which has been proved by Rudnick and Sarnak [20]. The case  $d = 2$  (which corresponds to the energy levels of the *boxed oscillator*) has received particular attention; see for example [14, 18, 21, 29]. A generalization from  $(\{n^d\alpha\})_{n \geq 1}$  to the case of  $(\{a(n)\alpha\})_{n \geq 1}$  with  $a(x) \in \mathbb{Z}[x]$  is obtained in [6]; again the pair correlations are asymptotically Poissonian for almost all  $\alpha$ , provided that the degree of  $a(x)$  is at least 2. Another case which has been intensively investigated is that of  $(\{a(n)\alpha\})_{n \geq 1}$  for  $(a(n))_{n \geq 1}$

being a *lacunary* sequence; see for example [3, 11, 22].

In [1] a general result was proved which includes earlier results (polynomial sequences, lacunary sequences, and sequences satisfying certain Diophantine conditions) and gives a unifying explanation. This result links the distribution of the pair correlations of the sequence  $(\{a(n)\alpha\})_{n \geq 1}$  to the additive energy of the truncations of the integer sequence  $(a(n))_{n \geq 1}$ , a well-known concept from additive combinatorics which has been intensively studied. Recall that the additive energy  $E(A)$  of a set of real numbers  $A$  is defined as

$$E(A) := \sum_{a+b=c+d} 1, \quad (1)$$

where the sum is extended over all quadruples  $(a, b, c, d) \in A^4$ . Trivially one has the estimate  $|A|^2 \leq E(A) \leq |A|^3$ , assuming that the elements of  $A$  are distinct. The additive energy of sequences has been extensively studied in the combinatorics literature. We refer the reader to [28] for a discussion of its properties and applications. To simplify notations, in the sequel whenever a sequence  $A := (a(n))_{n \geq 1}$  is fixed we will abbreviate  $R_2(s, \alpha, N)$  for  $R_2([-s, s], (\{a(n)\alpha\})_{n \geq 1}, N)$ . Furthermore we will let  $A_N$  denote the first  $N$  elements of  $A$ . The result states that if the truncations  $A_N$  of an integer sequence  $A$  satisfy  $E(A_N) \ll N^{3-\varepsilon}$  for some  $\varepsilon > 0$ , then  $(\{a(n)\alpha\})_{n \geq 1}$  has (asymptotically) Poissonian pair correlations for almost all  $\alpha$ . More precisely, the following theorem is true.

**Theorem 1.** *Let  $(a(n))_{n \geq 1}$  be a sequence of distinct integers, and suppose that there exists a fixed constant  $\varepsilon > 0$  such that*

$$E(A_N) \ll N^{3-\varepsilon} \quad \text{as } N \rightarrow \infty. \quad (2)$$

*Then for almost all  $\alpha$  one has*

$$R_2(s, \alpha, N) \rightarrow 2s \quad \text{as } N \rightarrow \infty \quad (3)$$

*for all  $s \geq 0$ .*

Note that the condition of Theorem 1 is close to optimality, since by the trivial upper bound we always have  $E(A_N) \leq N^3$ ; thus an arbitrarily small power savings over the trivial upper bound assures the “quasi-random” behavior of the pair correlations of  $(\{a(n)\alpha\})_{n \geq 1}$ . On the other hand, in [1] Bourgain showed the following negative result.

**Theorem 2.** *If  $E(A_N) = \Omega(N^3)$ , then there exists a subset of  $[0, 1]$  of positive measure such that for every  $\alpha$  from this set the pair correlations of the sequence  $(\{a(n)\alpha\})_{n \geq 1}$  are not asymptotically Poissonian.*

We conjecture that actually even the following much stronger assertion is true.

*Conjecture 1.* *If  $E(A_N) = \Omega(N^3)$  there is **no**  $\alpha$  for which the pair correlations of the sequence  $(\{a(n)\alpha\})_{n \geq 1}$  are Poissonian.*

In this paper we will prove a first partial result which should support this conjecture. However, before stating and discussing our result (which will be done in Section 2 below), we want to continue our general discussion of pair correlation problems. As one can see from the previous paragraphs, the metric theory of pair correlation problems on the torus is relatively well-understood. In contrast, there are only very few corresponding results which hold for a *specific* value of  $\alpha$ . The most interesting case is that of the sequence  $(\{n^2\alpha\})_{n \geq 1}$ , where it is assumed that there is a close relation between Diophantine properties of  $\alpha$  and the pair correlations distribution. For example, it is conjectured that for a quadratic irrational  $\alpha$  this sequence has a pair correlations distribution which is asymptotically Poissonian; however, a proof of this conjecture seems to be far out of reach. A first step towards a proof of the conjecture was made by Heath-Brown [14], whose method requires bounds on the number of solutions of certain quadratic congruences; this topic was taken up by Shparlinski [26, 27], who obtained some improvements, but new ideas seem to be necessary for further steps toward a solution of the conjecture.

It should also be noted that the investigation of pair correlation distributions is not restricted to sequences of the torus. For example, consider a positive definite quadratic form  $P(x, y) = \alpha x^2 + \beta xy + \gamma y^2$ , and its values at the integers  $(x, y) = (m, n) \in \mathbb{Z}^2$ . These values form a discrete subset of  $\mathbb{R}$ , and one can study the pair correlations of those numbers contained in a finite window  $[0, N]$ . See for example [23, 30]. Another famous occurrence of the pair correlation statistics of an unbounded sequence in  $\mathbb{R}$  is in Montgomery's pair correlation conjecture for the normalized spacings between the imaginary parts of zeros of the Riemann zeta function. The statement of the full conjecture is a bit too long to be reproduced here; we just want to mention that it predicts a distribution of the pair correlations which is very different from "simple" random behavior. For more details see Montgomery's paper [19]. There is a famous story related to Montgomery's conjecture; he met the mathematical physicist Freeman Dyson at tea time at Princeton, where Freeman Dyson identified Montgomery's conjectured distribution as the typical distribution of the spacings between normalized eigenvalues of large random Hermitian matrices – an observation which has led to the famous (conjectural) connection between the theory of the Riemann zeta function and random matrix theory. The whole story and more details can be found in [8].

## 2 New results

In the sequel we give a first partial result towards a solution of the conjecture made above. Before stating the result we introduce some notations, and explain the background from additive combinatorics. For  $v \in \mathbb{Z}$  let  $A_N(v)$  denote the cardinality of the set

$$\left\{ (x, y) \in \{1, \dots, N\}^2, x \neq y : a(x) - a(y) = v \right\}.$$

Then

$$E(A_N) = \Omega(N^3) \quad (4)$$

is equivalent to

$$\sum_{v \in \mathbb{Z}} A_N^2(v) = \Omega(N^3), \quad (5)$$

which implies that there is a  $\kappa > 0$  and positive integers  $N_1 < N_2 < N_3 < \dots$  such that

$$\sum_{v \in \mathbb{Z}} A_{N_i}^2(v) \geq \kappa N_i^3, \quad i = 1, 2, \dots \quad (6)$$

It will turn out that sequences  $(a(n))_{n \geq 1}$  satisfying (4) have a strong linear substructure. From (6) we can deduce by the Balog–Szemerédi–Gowers-Theorem (see [2] and [13]) that there exist constants  $c, C > 0$  depending only on  $\kappa$  such that for all  $i = 1, 2, 3, \dots$  there is a subset  $A_0^{(i)} \subset (a(n))_{1 \leq n \leq N_i}$  such that

$$|A_0^{(i)}| \geq cN_i \quad \text{and} \quad |A_0^{(i)} + A_0^{(i)}| \leq C|A_0^{(i)}| \leq CN_i.$$

The converse is also true: If for all  $i$  for a set  $A_0^{(i)}$  with  $A_0^{(i)} \subset (a(n))_{1 \leq n \leq N_i}$  with  $|A_0^{(i)}| \geq cN_i$  we have  $|A_0^{(i)} + A_0^{(i)}| \leq C|A_0^{(i)}|$ , then

$$\sum_{v \in \mathbb{Z}} A_{N_i}^2(v) \geq \frac{1}{C} |A_0^{(i)}|^3 \geq \frac{c^3}{C} N_i^3$$

and consequently  $\sum_{v \in \mathbb{Z}} A_N^2(v) = \Omega(N^3)$  (this an elementary fact, see for example Lemma 1 (iii) in [15].)

Consider now a subset  $A_0^{(i)}$  of  $(a(n))_{1 \leq n \leq N_i}$  with

$$|A_0^{(i)}| \geq cN_i \quad \text{and} \quad |A_0^{(i)} + A_0^{(i)}| \leq C|A_0^{(i)}|.$$

By the theorem of Freiman (see [12]) there exist constants  $d$  and  $K$  depending only on  $c$  and  $C$ , i.e. depending only on  $\kappa$  in our setting, such that there exists a  $d$ -dimensional arithmetic progression  $P_i$  of size at most  $KN_i$  such that  $A_0^{(i)} \subset P_i$ . This means that  $P_i$  is a set of the form

$$P_i := \left\{ b_i + \sum_{j=1}^d r_j k_j^{(i)} \mid 0 \leq r_j < s_j^{(i)} \right\}, \quad (7)$$

with  $b_i, k_1^{(i)}, \dots, k_d^{(i)}, s_1^{(i)}, \dots, s_d^{(i)} \in \mathbb{Z}$  and such that  $s_1^{(i)} s_2^{(i)} \dots s_d^{(i)} \leq KN_i$ .

In the other direction again it is easy to see that for any set  $A_0^{(i)}$  of the form (7) we have

$$|A_0^{(i)} + A_0^{(i)}| \leq 2^d KN_i.$$

Based on these observations we make the following definition:

**Definition 1.** Let  $(a(n))_{n \geq 1}$  be a strictly increasing sequence of positive integers. We call this sequence *quasi-arithmetic of degree  $\mathbf{d}$* , where  $d$  is a positive integer, if there exist constants  $C, K > 0$  and a strictly increasing sequence  $(N_i)_{i \geq 1}$  of positive integers such that for all  $i \geq 1$  there is a subset  $A^{(i)} \subset (a(n))_{1 \leq n \leq N_i}$  with  $|A^{(i)}| \geq CN_i$  such that  $A^{(i)}$  is contained in a  $d$ -dimensional arithmetic progression  $P^{(i)}$  of size at most  $KN_i$ .

The considerations above show that a sequence  $(a(x))_{x \geq 1}$  is quasi-arithmetic of some degree  $d$  if and only if it satisfies (5).

So our conjecture is equivalent to

*Conjecture 2. If  $(a(n))_{n \geq 1}$  is a quasi-arithmetic sequence of integers then there is no  $\alpha$  such that the pair correlations of  $(\{a(n)\alpha\})_{x \geq 1}$  are asymptotically Poissonian.*

In the remaining part of this paper we will prove a theorem which slightly improves the Theorem 2 of Bourgain for the subclass of sequences  $(a(n))_{n \geq 1}$  which are quasi-arithmetic of degree 1.

**Theorem 3.** *If the sequence of integers  $(a(n))_{n \geq 1}$  is quasi-arithmetic of degree 1, then the set of  $\alpha$ 's for which the distribution of the pair correlations of  $(\{a(n)\alpha\})_{n \geq 1}$  is not asymptotically Poissonian has full measure.*

**Remark.** *The class of quasi-arithmetic sequences  $(a(n))_{n \geq 1}$  of degree 1 contains all strictly increasing sequences with positive upper density, i.e.*

$$\limsup_{N \rightarrow \infty} \frac{1}{N} \sum_{\substack{n=1 \\ m \in \{a(n) \mid n \geq 1\}}}^N 1 > 0.$$

*In particular this class contains all strictly increasing sequences which are bounded above by a linear function.*

We will first state two auxiliary results in Section 3, and then give the proof of Theorem 3 in Section 4.

### 3 Auxiliary results

**Lemma 1.** *Let  $(\lambda_n)_{n \geq 1}$  be a strictly increasing sequence of positive integers. Let  $\mu_n$  be the number of fractions of the form  $j\lambda_n^{-1}$  ( $0 < j < \lambda_n$ ) which are not of the form  $k\lambda_q^{-1}$  with some  $q < n$  and  $k < \lambda_q$ . Furthermore, let  $(\psi_n)_{n \geq 1}$  be a non-increasing sequence of positive reals such that  $\sum_{n=1}^{\infty} \psi_n = \infty$  and with the following property (\*):*

*There exists a sequence  $(\tau_n)_{n \geq 1}$  of positive reals tending monotonically to zero, but so slowly that  $\sum_{n=1}^{\infty} \psi_n \tau_n$  still diverges, and such that there exist a constant  $c > 0$  and infinitely many positive integers  $N$  with*

$$\sum_{n=1}^N \mu_n \lambda_n^{-1} \psi_n \tau_n > c \sum_{n=1}^N \psi_n \tau_n.$$

*Then – if (\*) holds – for almost all  $\theta \in \mathbb{R}$  there exist infinitely many positive integers  $n$ , and integers  $m$ , such that*

$$0 \leq \lambda_n \theta - m < \psi_n.$$

*Proof.* This lemma is essentially the divergence part of Theorem IV in [10]. It is shown there that the assertion of our Lemma 1 is true under the slightly stronger condition that  $(\psi_n)_{n \geq 1}$  – as in our Lemma – is a non-increasing sequence of positive reals with  $\sum_{n=1}^{\infty} \psi_n = \infty$ , and that  $(\lambda_n)_{n \geq 1}$  satisfies

$$\liminf_{N \rightarrow \infty} \frac{1}{N} \sum_{n=1}^N \mu_n \lambda_n^{-1} > 0.$$

If we follow the proof of Theorem IV in [10] line by line we see that our slightly weaker condition (\*) also is sufficient to obtain the desired result. In fact replacing Cassel's condition by our condition (\*) is relevant only in the proof of Lemma 3 in [10], which is an auxiliary result for the proof of Theorem IV in [10].  $\square$

**Lemma 2.** *For all  $\delta > 0$  there is a positive constant  $c(\delta) > 0$ , such that for every infinite subset  $A$  of  $\mathbb{N}$  with*

$$\underline{d}(A) := \liminf_{N \rightarrow \infty} \frac{1}{N} \# \{n \leq N \mid n \in A\} > \delta$$

*we have*

$$\liminf_{N \rightarrow \infty} \frac{1}{N} \sum_{\substack{n \leq N \\ n \in A}} \frac{\varphi(n)}{n} \geq c(\delta).$$

*Here  $\varphi$  denotes the Euler totient function.*

*Proof.* Let

$$B(t) := \lim_{N \rightarrow \infty} \frac{1}{N} \left| \left\{ n \leq N \mid \frac{n}{\varphi(n)} \geq t \right\} \right|.$$

Then by the main theorem in [31] the limit  $B(t)$  exists and satisfies

$$B(t) = \exp \left( e^{-t e^{-\gamma} (1 + O(t^{-2}))} \right)$$

for  $t$  to infinity and with  $\gamma$  denoting Euler's constant. Here, and in the sequel, we write  $\exp(x)$  for  $e^x$ .

So there is a constant  $L > 0$  such that

$$B(t) \leq \exp\left(e^{-te^{-\gamma}\left(1-\frac{L}{t^2}\right)}\right)$$

for all  $t \geq 1$ . Hence

$$B(t) \leq \exp\left(e^{-\frac{1}{2}te^{-\gamma}}\right)$$

for all  $t \geq \max(1, \sqrt{2L})$ . Now assume that  $\delta > 0$  is so small that

$$t_0 := 2e^\gamma \log\left(-\log \frac{\delta}{4}\right) > \max(1, \sqrt{2L}).$$

Note that it suffices to prove the lemma for such  $\delta$ . We have

$$B(t_0) = \lim_{N \rightarrow \infty} \frac{1}{N} \left| \left\{ n \leq N \mid \frac{n}{\varphi(n)} \geq t_0 \right\} \right|$$

and

$$B(t_0) \leq \exp\left(e^{-\frac{1}{2}te^{-\gamma}t_0}\right) = \frac{\delta}{4}.$$

Hence there exists  $N_0$  such that for all  $N \geq N_0$

$$\frac{1}{N} \left| \left\{ n \leq N \mid \frac{n}{\varphi(n)} \geq t_0 \right\} \right| \leq \frac{\delta}{3}.$$

Therefore, since  $\underline{d}(A) > \delta$ , for all sufficiently large  $N$  we have

$$\frac{1}{N} \left| \left\{ n \leq N, n \in A \mid \frac{n}{\varphi(n)} \leq t_0 \right\} \right| \geq \frac{\delta}{3}$$

and consequently also

$$\frac{1}{N} \sum_{\substack{n \leq N \\ n \in A}} \frac{\varphi(n)}{n} \geq \frac{\delta}{3} \frac{1}{t_0} =: c(\delta) > 0.$$

□

## 4 Proof of Theorem 3

Let  $(a(n))_{n \geq 1}$  be quasi-arithmetic of degree one and let  $C, K > 0, (N_i)_{i \geq 1}, (A^{(i)})_{i \geq 1}$  and  $(P^{(i)})_{i \geq 1}$  be as described in Definition 1. In the sequel we will define induc-

tively a certain strictly increasing subsequence  $(M_l)_{l \geq 1}$  of  $(N_i)_{i \geq 1}$ .

Set  $M_1 := N_1$  and assume that  $M_1, M_2, \dots, M_{l-1}$  already are defined. If  $M_l = N_{i_l}$  (where  $i_l$  still has to be defined) to simplify notations we write  $A_l := A^{(i_l)}$ ,  $P_l := P^{(i_l)}$ .

We set

$$P_l := \{a_l + r\kappa_l \mid 0 \leq r < KM_l\}$$

and

$$A_l := \left\{ a_l + r_j^{(l)} \kappa_l \mid j = 1, 2, \dots, s_l \right\}$$

with certain fixed  $r_j^{(l)}$  with  $1 \leq r_1^{(l)} < r_2^{(l)} < \dots < r_{s_l}^{(l)} < KM_l$  and  $s_l \geq CM_l$ . Of course we have  $s_l < KM_l$ .

We consider

$$V_l := \left\{ (r_i^{(l)} - r_j^{(l)}) \kappa_l \mid 1 \leq j < i \leq s_l \right\},$$

the set of positive differences of  $A_l$ . Here  $V_l$  is the set itself, whereas by  $\tilde{V}_l$  we will denote the same set of positive differences but counted with multiplicity (so strictly speaking  $\tilde{V}_l$  is a multi-set rather than a set). Hence  $|\tilde{V}_l| < KM_l$ , whereas

$$|\tilde{V}_l| = \frac{s_l(s_l-1)}{2} \geq c_1 M_l^2.$$

Here and in the sequel we write  $c_i$  for positive constants depending only on  $C$  and  $K$ . We note that a value  $u \in V_l$  has multiplicity at most  $s_l$ .

Let  $x$  be the number of elements in  $V_l$  with multiplicity at least  $c_2 M_l$  where  $c_2 := \min(K, \frac{c_1}{2K})$ . Assume that  $x < c_2 M_l$ . Then

$$\begin{aligned} c_1 M_l^2 &\leq |\tilde{V}_l| \leq xs_l + (|V_l| - x)c_2 M_l \\ &\leq xKM_l + (KM_l - x)c_2 M_l \\ &= M_l(x(K - c_2) + Kc_2 M_l) \\ &< M_l^2(c_2(K - c_2) + Kc_2) \\ &< M_l^2 c_1, \end{aligned}$$

a contradiction.

So there are at least  $c_2 M_l$  values  $u \in V_l$  with multiplicity at least  $c_2 M_l$ . We take the  $\frac{c_2}{2} M_l$  largest of these values and denote them by  $T_1^{(l)} < T_2^{(l)} < \dots < T_{w_l}^{(l)}$  with  $w_l \geq \frac{c_2}{2} M_l$  and  $T_j^{(l)} := R_j^{(l)} \kappa_l$ . Note that

$$\frac{c_2}{2} M_l \leq R_1^{(l)} < \dots < R_{w_l}^{(l)} < KM_l. \quad (8)$$

Remember that we still have to choose  $i_l > i_{l-1}$  and to define  $M_l$  as  $N_{i_l}$ . We choose now  $i_l$  so large that

$$M_l > \left( \sum_{p=1}^{l-1} \sum_{q=1}^{w_p} T_q^{(p)} \right)^2. \quad (9)$$

So altogether we have constructed a strictly increasing sequence  $\lambda_1 < \lambda_2 < \lambda_3 < \dots$  of integers given by  $T_1^{(1)} < \dots < T_{w_1}^{(1)} < T_1^{(2)} < \dots < T_{w_2}^{(2)} < T_1^{(3)} < \dots$ .

Furthermore we define a decreasing sequence  $(\psi_n)_{n \geq 1}$  of positive reals in the following way. If  $\lambda_n$  is such that  $T_1^{(l)} \leq \lambda_n \leq T_{w_l}^{(l)}$ , then  $\psi_n := \frac{1}{M_l}$ .

Obviously we have

$$\lim_{n \rightarrow \infty} \psi_n = 0$$

and

$$\sum_{n=1}^{\infty} \psi_n \geq \sum_{l=1}^{\infty} w_l \frac{1}{M_l} \geq \sum_{l=1}^{\infty} \frac{c_2}{2} M_l \frac{1}{M_l} = \infty.$$

We will show below that  $(\lambda_n)$  and  $(\psi_n)$  satisfy the condition (\*) of Lemma 1.

We choose  $N := w_1 + \dots + w_l$  and first estimate  $\sum_{n \leq N} \mu_n \lambda_n^{-1} \psi_n$  from below (for the definition of  $\mu_n$  see Lemma 1). We have

$$\sum_{n \leq N} \mu_n \lambda_n^{-1} \psi_n \geq \sum_{n=N-w_l+1}^N \mu_n \lambda_n^{-1} \psi_n.$$

In the following we estimate  $\mu_n$  from below for  $n$  with  $N - w_l + 1 \leq n \leq N$ , i.e.,  $\lambda_n = T_i^{(l)} = R_i^{(l)} \kappa_l$  for some  $i$  with  $1 \leq i \leq w_l$ .

Consider first  $\lambda_q$  with  $q \leq w_1 + \dots + w_{l-1}$ . Then the number of  $j$  with  $0 \leq j < \lambda_n$  such that  $j \lambda_q^{-1}$  is of the form  $k \lambda_q^{-1}$  with  $0 \leq k < \lambda_q$  trivially is at most  $\lambda_q$ .

Now consider  $\lambda_q$  with  $q > w_1 + \dots + w_{l-1}$  and  $\lambda_q < \lambda_n$ , i.e.,

$$\lambda_q = T_h^{(l)} = R_h^{(l)} \kappa_l$$

for some  $h$  with  $1 \leq h < i$ . Then the number of  $j$  with  $0 \leq j < \lambda_n$  such that  $j \lambda_q^{-1}$  is **not** of the form  $k \lambda_q^{-1}$  with  $0 \leq k < \lambda_q$ , i.e., such that

$$\begin{aligned} \frac{j}{\lambda_n} = \frac{k}{\lambda_q} &\Leftrightarrow \frac{j}{R_i^{(l)} \kappa_l} = \frac{k}{R_h^{(l)} \kappa_l} \\ &\Leftrightarrow \frac{j}{R_i^{(l)}} = \frac{k}{R_h^{(l)}} \end{aligned}$$

does **not** hold, is at least  $\varphi(R_i^{(l)}) \kappa_l$ . Hence by (8) and by (9)

$$\begin{aligned} \mu_n &\geq \varphi(R_i^{(l)}) \kappa_l - \sum_{q=1}^{w_1+\dots+w_{l-1}} \lambda_q \\ &\geq \varphi(R_i^{(l)}) \kappa_l - \sqrt{M_l} \geq \frac{1}{2} \varphi(R_i^{(l)}) \kappa_l \end{aligned}$$

for all  $l$  large enough, say  $l \geq l_0$  (note that  $R_i^{(l)} \geq \frac{c_2}{2} M_l$ ).

Therefore for  $l \geq l_0$

$$\begin{aligned} \sum_{n \leq N} \mu_n \lambda_n^{-1} \psi_n &\geq \sum_{n=N-w_l+1}^N \mu_n \lambda_n^{-1} \psi_n \\ &\geq \frac{1}{M_l} \sum_{i=1}^{w_l} \frac{1}{2} \varphi(R_i^{(l)}) \kappa_l \frac{1}{R_i^{(l)} \kappa_l} \\ &= \frac{1}{2M_l} \sum_{i=1}^{w_l} \frac{\varphi(R_i^{(l)})}{R_i^{(l)}}. \end{aligned} \tag{10}$$

Later on we will use the same chain of inequalities starting from the second expression in (10).

We recall that  $w_l \geq \frac{c_2}{2} M_l$ , and  $R_i^{(l)} \leq KM_l$  for all  $i = 1, \dots, w_l$ . Hence  $R_1^{(l)}, \dots, R_{w_l}^{(l)}$  form a subset of  $\{1, 2, \dots, KM_l\}$  of density at least  $c_3 := \frac{c_2}{2K}$ . Hence by Lemma 2 we have for  $l$  large enough and with  $c$  from Lemma 2 that

$$\sum_{n \leq N} \mu_n \lambda_n^{-1} \psi_n \geq \frac{K}{2} c \left( \frac{c_2}{2K} \right) =: c_4 > 0. \tag{11}$$

This holds for all  $N = w_1 + \dots + w_l$  and all  $l \geq l_0$ .

Finally we have to choose the function  $(\tau_n)_{n \geq 1}$  from condition  $(*)$  in Lemma 1 in a suitable way. If  $\lambda_n$  is such that  $T_1^{(l)} \leq \lambda_n \leq T_{w_l}^{(l)}$ , i.e., if  $\psi_n = \frac{1}{M_l}$ , then we set  $\tau_n := \frac{1}{l}$ . Then

$$\sum_{n=1}^{\infty} \psi_n \tau_n \geq \sum_{l=1}^{\infty} w_l \frac{1}{M_l} \frac{1}{l} \geq \sum_{l=1}^{\infty} \frac{c_2}{2} M_l \frac{1}{M_l} \frac{1}{l} = \infty.$$

Finally, on the one hand for all  $N = w_1 + \dots + w_l$  we have by (10) and (11) that

$$\sum_{n \leq N} \mu_n \lambda_n^{-1} \psi_n \tau_n \geq \sum_{l'=l_0}^l c_4 \frac{1}{l'} \geq c_5 \log l$$

for all  $l \geq l_0$ .

On the other hand we have

$$\sum_{n \leq N} \psi_n \tau_n \leq \sum_{l'=1}^l w_{i_l} \frac{1}{M_l} \frac{1}{l} = \sum_{l'=1}^l K \frac{1}{l} \leq c_6 \log l.$$

Consequently

$$\sum_{n \leq N} \mu_n \lambda_n^{-1} \psi_n \tau_n \geq c_5 \log l \geq \frac{c_5}{c_6} \sum_{n \leq N} \psi_n \tau_n$$

and the conditions of Lemma 1 are satisfied for  $(\lambda_n)_{n \geq 1}$  and  $(\psi_n)_{n \geq 1}$ . We conclude from Lemma 1 that for almost all  $\alpha$  there exist infinitely many  $n$  such that  $\|\lambda_n \alpha\| \leq \psi_n$  holds. Let such an  $\alpha$  be given, and let  $n_1 < n_2 < n_3 < \dots$  be such that  $\|\lambda_{n_i} \alpha\| \leq \psi_{n_i}$  for all  $i = 1, 2, 3, \dots$ . For any  $n_i$  let  $l(n_i)$  be defined such that  $w_1 + w_2 + \dots + w_{l(n_i)-1} < n_i \leq w_1 + w_2 + \dots + w_{l(n_i)}$ , then  $\psi_{n_i} = \frac{1}{M_{l(n_i)}}$ , hence

$$0 \leq \|\lambda_{n_i} \alpha\| M_{l(n_i)} < 1$$

for all  $i$ .

Let  $\rho$  with  $0 \leq \rho \leq 1$  be a limit point of  $(\|\lambda_{n_i} \alpha\| M_{l(n_i)})_{i=1,2,\dots}$ . We distinguish now between two cases.

First case:  $\rho = 0$ .

Then there exists a subsequence  $m_1 < m_2 < m_3 < \dots$  of  $n_1 < n_2 < n_3 < \dots$  such that

$$0 \leq \|\lambda_{m_i} \alpha\| < \frac{1}{M_{l(m_i)}} \frac{c_2}{4K^2}$$

for all  $i$ .  $\lambda_{m_i}$  is an element of  $V_{l(m_i)}$  with multiplicity at least  $c_2 M_{l(m_i)}$ . Hence there exist at least  $c_2 M_{l(m_i)}$  pairs  $(p, q)$  with

$$1 \leq p < q \leq s_{l(m_i)} < KM_{l(m_i)}$$

and

$$\|\{a(q)\alpha\} - \{a(p)\alpha\}\| < \frac{1}{M_{l(m_i)}} \frac{c_2}{4K^2}.$$

Let now  $s = \frac{c_2}{4K}$  then for all  $M = KM_{l(m_i)}$  we have

$$\frac{1}{M} \# \left\{ 1 \leq p \neq q \leq M : \|\{a(q)\alpha\} - \{a(p)\alpha\}\| \leq \frac{s}{M} \right\} \geq \frac{c_2}{K} = 4s,$$

and hence

$$R_2([-s, s], \alpha, M) \not\rightarrow 2s.$$

Second case:  $\rho > 0$ .

Let  $\varepsilon := \min\left(\frac{\rho}{2}, \frac{c_2}{8K^2}\right) > 0$ . Then there exists a subsequence  $m_1 < m_2 < m_3 < \dots$  of  $n_1 < n_2 < n_3 < \dots$  such that

$$0 \leq |M_{l(m_i)} \|\lambda_{m_i} \alpha\| - \rho| < \varepsilon$$

for all  $i$ . Hence there exist at least  $c_2 M_{l(m_i)}$  pairs  $(p, q)$  with  $1 \leq p < q \leq s_{l(m_i)} < KM_{l(m_i)}$  and

$$\|\{a(q)\alpha\} - \{a(p)\alpha\}\| \in \left[\frac{\rho - \varepsilon}{M_{l(m_i)}}, \frac{\rho + \varepsilon}{M_{l(m_i)}}\right].$$

Let  $s_1 := K(\rho - \varepsilon)$  and  $s_2 := K(\rho + \varepsilon)$ , then  $s_2 - s_1 = 2K\varepsilon \leq \frac{c_2}{4K}$ . Let for  $M := KM_{l(m_i)}$  and  $j = 1, 2$ :

$$\Lambda^{(j)} := \frac{1}{M} \# \left\{ 1 \leq p \neq q \leq M : \|\{a(q)\alpha\} - \{a(p)\alpha\}\| \leq \frac{s_j}{M} \right\}.$$

Then  $\Lambda^{(2)} - \Lambda^{(1)} \geq \frac{1}{M} c_2 \frac{M}{K} = \frac{c_2}{K}$ . Hence at least one of

$$\begin{aligned} |\Lambda^{(2)} - 2s_2| &\geq \frac{c_2}{8K} \quad \text{or} \\ |\Lambda^{(1)} - 2s_1| &\geq \frac{c_2}{8K} \quad \text{holds,} \end{aligned}$$

since otherwise

$$\begin{aligned} \frac{c_2}{2K} &\leq |\Lambda^{(2)} - \Lambda^{(1)}| - 2(s_2 - s_1) \\ &\leq |\Lambda^{(2)} - 2s_2 - \Lambda^{(1)} + 2s_1| \leq |\Lambda^{(2)} - 2s_2| + |\Lambda^{(1)} - 2s_1| \\ &\leq \frac{c_2}{4K}, \end{aligned}$$

which is a contradiction. Therefore either

$$R_2([-s_1, s_1], \alpha, M) \not\ni 2s_1 \quad \text{or}$$

$$R_2([-s_2, s_2], \alpha, M) \not\ni 2s_2,$$

which proves the theorem.

**Acknowledgements** The first author is supported by CERN, European Organization for Nuclear Research, Geneva, as part of the Austrian Doctoral Student Programme.

The second author is supported by the Austrian Science Fund (FWF), START-project Y-901.

The third author is supported by the Austrian Science Fund (FWF): Project F5507-N26, which is part of the Special Research Program “Quasi-Monte Carlo Methods: Theory and Applications”.

## References

1. Aistleitner Ch., Larcher G., Lewko M.: Additive energy and the Hausdorff dimension of the exceptional set in metric pair correlation problems. With an appendix by Jean Bourgain. To appear in: Israel J. Math.
2. Balog A., Szemerédi E.: A statistical theorem of set addition. Combinatorica, **14**, 263–268 (1994)
3. Berkes I., Philipp W., Tichy R.: Pair correlations and  $U$ -statistics for independent and weakly dependent random variables. Illinois J. Math., **45**(2), 559–580 (2001)
4. Berry M. V., Tabor M.: Level clustering in the regular spectrum. Proc. R. Soc. (London), A **356**, 375–394 (1977)
5. Bleher P. M.: The energy level spacing for two harmonic oscillators with golden mean ratio of frequencies. J. Stat. Phys. **61**, 869–876 (1990)
6. Boca F. P., Zaharescu A.: Pair correlation of values of rational functions (mod  $p$ ). Duke Math. J., **105**(2), 267–307 (2000)
7. Bogomolny E.: Quantum and arithmetic chaos. Proceedings of the Les Houches Winter School “Frontiers in Number Theory, Physics and Geometry” (2003)
8. Bourgade P.: Tea Time at Princeton. Harvard College Mathematical Review **4**, 41–53 (2012). Available at <http://www.cims.nyu.edu/~bourgade/papers/TeaTime.pdf>.
9. Casati G., Guarneri I., Izrailev F. M.: Statistical properties of the quasi-energy spectrum of a simple integrable system. Phys. Lett. A **124**, 263–266 (1987)
10. Cassels J. W. S.: Some metrical theorems in Diophantine Approximation I. Math. Proc. Cam. Phil. Soc., **46**, 209–218 (1950)
11. Chaubey S., Lanius M., Zaharescu A.: Pair correlation of fractional parts derived from rational valued sequences. J. Number Theory, **151**, 147–158 (2015)
12. Freiman G. R.: Foundations of a Structural Theory of Set Addition. Translations of Mathematical Monographs 37, Amer. Math. Soc., Providence, USA, (1973)
13. Gowers W. T.: A new proof of Szemerédi’s theorem for arithmetic progressions of length four. Geometric and Functional Analysis, **8**, 529–551 (1998)
14. Heath-Brown D. R.: Pair correlation for fractional parts of  $\alpha n^2$ . Math. Proc. Cambridge Philos. Soc., **148**(3), 385–407 (2010)
15. Lev, V.F.: The (Gowers-)Balog-Szemerédi Theorem: An Exposition. <http://people.math.gatech.edu/~ecroot/8803/baloszem.pdf>
16. Marklof J.: Energy level statistics, lattice point problems and almost modular functions. Frontiers in Number Theory, Physics and Geometry. Volume 1: On random matrices, zeta functions and dynamical systems (Les Houches, 9–21 March 2003), Springer, 163–181
17. Marklof J.: The Berry–Tabor conjecture. European Congress of Mathematics, Vol. II (Barcelona, 2000), 421–427, Progr. Math., 202, Birkhäuser, Basel, 2001.
18. Marklof J., Strömbergsson A.: Equidistribution of Kronecker sequences along closed horocycles. Geom. Funct. Anal., **13**(6), 1239–1280 (2003)
19. Montgomery, H. L.: The pair correlation of zeros of the zeta function. Analytic number theory (Proc. Sympos. Pure Math., Vol. XXIV, St. Louis Univ., St. Louis, Mo., 1972), pp. 181–193. Amer. Math. Soc., Providence, R.I., 1973.
20. Rudnick Z., Sarnak P.: The pair correlation function of fractional parts of polynomials. Comm. Math. Phys. **194**(1), 61–70 (1998)
21. Rudnick Z., Sarnak P., Zaharescu A.: The distribution of spacings between the fractional parts of  $n^2\alpha$ . Invent. Math., **145**(1), 37–57 (2001)
22. Rudnick Z., Zaharescu A.: A metric result on the pair correlation of fractional parts of sequences. Acta Arith., **89**(3), 283–293 (1999)
23. Sarnak, P.: Values at integers of binary quadratic forms. Harmonic analysis and number theory (Montreal, PQ, 1996), 181–203, CMS Conf. Proc., 21, Amer. Math. Soc., Providence, RI, 1997.
24. Sloan I.: The method of polarized orbitals for the elastic scattering of slow electrons by ionized helium and atomic hydrogen. Proc. Roy. Soc. (London), A **281**, 151–163 (1964)

25. Sós V. T.: On the distribution mod 1 of the sequence  $n\alpha$ . *Ann. Univ. Sci. Budapest. Rolando Eötvös, Sect. Math.* 1, 127–134 (1958)
26. Shparlinski, I.E.: On small solutions to quadratic congruences. *J. Number Theory* 131 (2011), no. 6, 1105–1111.
27. Shparlinski, I.E.: On the restricted divisor function in arithmetic progressions. *Rev. Mat. Iberoam.* 28 (2012), no. 1, 231–238.
28. Tao T., Vu V.: Additive combinatorics, volume 105 of Cambridge Studies in Advanced Mathematics. Cambridge University Press, Cambridge (2006)
29. Truelsen J. L.: Divisor problems and the pair correlation for the fractional parts of  $n^2\alpha$ . *Int. Math. Res. Not. IMRN*, (16), 3144–3183 (2010)
30. Vanderkam, J. M.: Values at integers of homogeneous polynomials. *Duke Math. J.* 97 (1999), no. 2, 379–412.
31. Weingartner A.: The distribution functions of  $\sigma(n)/n$  and  $n/\varphi(n)$ . *Proc. Amer. Math. Soc.*, **135**, 2677–2681 (2007)



---

## List of Figures

---

1.1.	Collision event in the ATLAS experiment. . . . .	4
1.2.	Selecting a point set for QMC-simulation from a continuous motion in the unit square. . . . .	5
2.1.	Sketch of beam chamber with different materials . . . . .	9
2.2.	Synchrotron radiation is emitted into a narrow cone. . . . .	10
2.3.	Synchrotron spectra of the LHC and FCC . . . . .	12
2.4.	Illustration of the electron cloud phenomenon . . . . .	12
2.5.	Mass spectrum of a UHV system. . . . .	15
2.6.	Schematic of the PyVasco model. . . . .	16
2.7.	Sparse matrix representation in PyVasco . . . . .	24
2.8.	Memory arrangement in PyVasco . . . . .	30
2.9.	Graphical user interface of PyVasco (I) . . . . .	31
2.10.	Graphical user interface of PyVasco (II) . . . . .	32
2.11.	Schematic layout of the FCC . . . . .	33
2.12.	LHC and FCC beam screen . . . . .	35
2.14.	Cross section of FCC-ee vacuum chamber with winglets . . . . .	39
2.15.	Simulation example of the vacuum system for the FCC-ee. . . . .	39
3.1.	Billiard path wit starting point $x$ and slope $\alpha$ . . . . .	45
3.2.	Error bounds for MC and QMC . . . . .	48
3.3.	Similarity of the Kronecker sequence and the torus line. . . . .	51
3.4.	Billiard path with rational slope . . . . .	52
3.5.	Billiard path wir rational and irrational slope . . . . .	52
3.6.	Unfolding technique . . . . .	53
3.7.	Polygons and convex sets present BRS for the billiard path with irrational slope. . . . .	56
3.8.	Analogy of a point set, a billiard path and a torus line . . . . .	57
3.9.	Schematic of disk that is not a BRS (I) . . . . .	58
3.10.	Schematic of disk that is not a BRS (II) . . . . .	59
4.1.	Nuclear scattering of a hydrogen atom . . . . .	64

## LIST OF FIGURES

4.2. Level spacing distribution . . . . .	65
4.3. Distribution of sequence in unit interval . . . . .	66
4.4. Kronecker sequence on the unit circle. . . . .	67
4.5. Specific selection of the interval in case of the Kronecker sequence . . . . .	68
4.6. Classic and quantum mechanic probability density for the harmonic oscillator . . .	74
4.7. Probability density of the hydrogen atom . . . . .	76

---

## List of Tables

---

2.1.	Vacuum classification . . . . .	8
2.2.	Model parameters for physical description. . . . .	19
2.3.	Templat for simulation domain . . . . .	28
2.4.	Template for a pump . . . . .	28
2.5.	Template for a gas source . . . . .	28
2.6.	Template for the input file for one material. The place holder % indicates the users' input. . . . .	29
2.7.	Characteristic parameters for the FCC-hh . . . . .	36
2.8.	Characteristic parameters for the FCC-ee . . . . .	39
2.9.	Model parameters for physical description. . . . .	41
2.10.	Variables used in the mathematical model. . . . .	42
2.11.	Values for most common physical constants. . . . .	43
4.1.	Survey of studied sequences in literature wrt the Poissonian property. . . . .	68



---

## Bibliography

---

- [1] I. Aichinger, R. Kersevan, and P. Chiggiato, “Analytical methods for vacuum simulations in high energy accelerators for future machines based on lhc performances,” *Journal of Physical Review Accelerator and Beam, preprint arXiv:1707.07525*, 2017. submitted in July 2017.
- [2] I. Aichinger and G. Larcher, “Sets of bounded remainder for the billiard on a square,” *Journal of Uniform Distribution Theory*, 2017. submitted 2016.
- [3] I. Aichinger, C. Aistleitner, and G. Larcher, “On quasi-energy-spectra, pair correlations of sequences and additive combinatorics,” *80th birthday festschrift for Ian Sloan published by Springer Verlag*, 2017. submitted 2016, accepted in June 2017.
- [4] M. Benedikt and F. Zimmermann, “The future circular collider study,” *CERN Cour.*, vol. 54, pp. 16 –17, April 2014.
- [5] O. Gröbner, “Overview of the lhc vacuum system,” *Vacuum*, vol. 60, no. 1, pp. 25–34, 2001.
- [6] C. B. Nakhosteen and K. Jousten, *Handbook of vacuum technology*. John Wiley & Sons, 2016.
- [7] A. Hofmann, *The physics of synchrotron radiation*, vol. 20. Cambridge University Press, 2004.
- [8] A. Mathewson and S. Zhang, “Beam-gas ionisation cross sections at 7.0 tev,” tech. rep., CERN, 1996.
- [9] C. Lemieux, *Monte Carlo and Quasi-Monte Carlo Sampling*. Springer, 2009.
- [10] H. Niederreiter, *Random number generation and quasi-Monte Carlo methods*. SIAM, 1992.
- [11] G. Leobacher and F. Pillichshammer, *Introduction to quasi-Monte Carlo integration and applications*. Springer, 2014.
- [12] J. Beck, *Super-uniformity of the typical billiard path*. Springer, 2010.
- [13] H.-J. Stöckmann, *Quantum chaos: an introduction*. Cambridge University Press, 2000.

## BIBLIOGRAPHY

- [14] M. V. Berry and M. Tabor, “Level clustering in the regular spectrum,” in *Proceedings of the Royal Society of London A: Mathematical, Physical and Engineering Sciences*, vol. 356, pp. 375–394, The Royal Society, 1977.
- [15] I. Sloan, “The method of polarized orbitals for the elastic scattering of slow electrons by ionized helium and atomic hydrogen,” *Proceedings of the Royal Society of London A: Mathematical, Physical and Engineering Sciences*, vol. 281, no. 1385, pp. 151–163, 1964.
- [16] A. Rossi, “Vasco (vacuum stability code): multi-gas code to calculate gas density profile in a UHV system,” tech. rep., CERN, 2004.
- [17] I. Aichinger, “Simulation of the evolution of the residual gas particle density – an analytical approach,” in *FCC week 2016*, (Rom, Italy), CERN, 2016.
- [18] I. Aichinger, “Pressure profile in the experimental areas of fcc hh and ee, calculation by an analytical code,” in *FCC week 2017*, (Berlin, Germany), CERN, 2017.
- [19] R. A. Haefer, *Kryo-Vakuumtechnik: Grundlagen und Anwendungen*. Springer-Verlag, 2013.
- [20] A. Roth, *Vacuum technology*. Elsevier, 2012.
- [21] G. Bird, *Molecular gas dynamics*. Oxford: Clarendon, 1976.
- [22] J. Lafferty, ed., *Foundations of Vacuum Science and Technology*. Wiley, 1998.
- [23] J. Ferziger and H. Kaper, “Mathematical theory of transport processes in gases,” *American Journal of Physics (AAPT)*, vol. 41, no. 4, pp. 601–603, 1973.
- [24] P. Chiggiato, “Vacuum technology for ion sources,” *arXiv preprint arXiv:1404.0960*, 2014.
- [25] S. G. Brush and N. S. Hall, *The Kinetic Theory Of Gases*, vol. 1 of *History of Modern Physical Sciences*. Imperial College Press and distributed by World Scientific Publishing CO., 2003.
- [26] M. Knudsen, “Die Gesetze der Molekularströmung und der inneren Reibungsströmung der Gase durch Röhren,” *Annalen der Physik*, vol. 333, no. 1, pp. 75–130, 1909.
- [27] P. Cruikshank, K. Artoos, F. Bertinelli, J.-C. Brunet, R. Calder, C. Campedel, I. Collins, J.-M. Dalin, B. Feral, O. Grobner, *et al.*, “Mechanical design aspects of the lhc beam screen,” in *Particle Accelerator Conference, 1997. Proceedings of the 1997*, vol. 3, pp. 3586–3588, IEEE, 1997.
- [28] R. Calder, “Ion induced gas desorption problems in the isr,” *Vacuum*, vol. 24, no. 10, pp. 437–443, 1974.

## BIBLIOGRAPHY

- [29] W. C. Turner, “Ion desorption stability in superconducting high energy physics proton colliders,” *Journal of Vacuum Science & Technology A: Vacuum, Surfaces, and Films (AVS)*, vol. 14, no. 4, pp. 2026–2038, 1996.
- [30] H. Wiedemann, *Particle accelerator physics*. Springer, 2015.
- [31] K. Wille, *Physik der Teilchenbeschleuniger und Synchrotronstrahlungsquellen*. Teubner, 1996.
- [32] A. W. Chao, K. H. Mess, M. Tigner, and F. Zimmermann, eds., *Handbook of accelerator physics and engineering*. Singapore: World scientific, 2013.
- [33] J. Tückmantel, “Synchrotron radiation damping in LHC and longitudinal bunch shape,” tech. rep., CERN, 2005.
- [34] V. Baglin, C. Grünhagel, I. Collins, O. Gröbner, and B. Jenninger, “Synchrotron radiation studies of the LHC dipole beam screen with COLDEX,” in *EPAC 2002*, (Paris, France), June 2002.
- [35] J. Gómez-Goñi, O. Gröbner, and A. Mathewson, “Comparison of photodesorption yields using synchrotron radiation of low critical energies for stainless steel, copper, and electrodeposited copper surfaces,” *Journal of Vacuum Science & Technology A: Vacuum, Surfaces, and Films (AVS)*, vol. 12, no. 4, pp. 1714–1718, 1994.
- [36] V. Baglin, “The lhc vacuum system: Commissioning up to nominal luminosity,” *Vacuum*, vol. 138, pp. 112–119, 2017.
- [37] R. Kersevan. personal communication.
- [38] M. Ady and R. Kersevan, “Introduction to the latest version of the test-particle Monte Carlo code Molflow+,” in *IPAC*, (Dresden, Germany), November 2014.
- [39] G. Iadarola, *Electron cloud studies for CERN particle accelerators and simulation code development*. PhD thesis, Università degli Studi di Napoli Federico II, Italy, 2014.
- [40] G. Iadarola and G. Rumolo, “Pyecloud and build-up simulations at cern,” *arXiv preprint arXiv:1309.6773*, 2013.
- [41] B. Bradu, A. Tovar González, E. Blanco Viñuela, P. Plutecki, E. Rogez, G. Iadarola, G. Ferlin, and B. Fernández Adiego, “Compensation of beam induced effects in LHC cryogenic systems,” in *7th International Particle Accelerator Conference*, (Busan, Korea), 2016.
- [42] C. Benvenuti, P. Chiggiato, P. C. Pinto, A. E. Santana, T. Hedley, A. Mongelluzzo, V. Ruzinov, and I. Wevers, “Vacuum properties of tizrv non-evaporable getter films,” *Vacuum*, vol. 60, no. 1, pp. 57–65, 2001.

## BIBLIOGRAPHY

- [43] P. Chiggiato and P. C. Pinto, “Ti–zr–v non-evaporable getter films: From development to large scale production for the large hadron collider,” *Thin Solid Films*, vol. 515, no. 2, pp. 382–388, 2006.
- [44] A. Bonucci, A. Conte, P. Manini, and S. Raimondi, “The transmission factor method: in-situ characterization of getter coated pipes,” in *AIP Conference Proceedings*, vol. 879, pp. 432–435, AIP, 2007.
- [45] J. Crank, *The mathematics of diffusion*. Oxford university press, 1979.
- [46] Y. Saad, *Iterative methods for sparse linear systems*. SIAM, 2003.
- [47] E. B. Saff and A. D. Snider, *Fundamentals of Matrix Analysis with Applications*. John Wiley & Sons, 2015.
- [48] P.-F. Hsieh and Y. Sibuya, *Basic theory of ordinary differential equations*. Springer Science & Business Media, 2012.
- [49] E. Picard, “Mémoire sur la théorie des équations aux dérivées partielles et la méthode des approximations successives,” *Journal de Mathématiques pures et appliquées*, vol. 6, pp. 145–210, 1890.
- [50] E. Lindelöf, “Sur l’application des méthodes d’approximations successives à l’étude des intégrales réelles des équations différentielles ordinaires,” *Journal de Mathématiques Pures et Appliquées*, vol. 10, pp. 117–128, 1894.
- [51] E. Lindelöf, “Démonstration de quelques théorèmes sur les équations différentielles,” *Journal de Mathématiques Pures et Appliquées*, vol. 6, pp. 423–441, 1900.
- [52] B. A. Meier, *Python GUI Programming Cookbook*. Packt Publishing Ltd, 2015.
- [53] M. Newman, *Computational physics*. CreateSpace Independent Publ., 2013.
- [54] M. Lutz, *Learning Python: Powerful Object-Oriented Programming*. O'Reilly Media, Inc., 2013.
- [55] C. Hill, *Learning scientific programming with Python*. Cambridge University Press, 2016.
- [56] M. Ady, *Monte Carlo simulations of ultra high vacuum and synchrotron radiation for particle accelerators*. PhD thesis, EPFL, CERN, 2016.
- [57] J. Wenninger, M. Benedikt, K. Oide, and F. Zimmermann, “Future circular collider study lepton collider parameters,” *CERN EDMS*, vol. 1346082, 2014.

## BIBLIOGRAPHY

- [58] A. Ball, M. Benedikt, L. Bottura, O. Dominguez, F. Gianotti, B. Goddard, P. Lebrun, M. Manzano, D. Schulte, E. Shaposhnikova, R. Tomas, and F. Zimmermann, “Future circular collider study hadron collider parameters,” *CERN EDMS*, 2014.
- [59] K. Oide, B. Holzer, A. Blondel, Y. Cai, A. Bogomyagkov, Y. Papaphilippou, S. Sinyatkin, B. Häger, M. Sullivan, M. Boscolo, *et al.*, “Design of beam optics for the fcc-ee collider ring,” in *7th International Particle Accelerator Conference*, (Busan, Korea), 2016.
- [60] O. Brüning, S. Oliver, P. Collier, P. Lebrun, S. Myers, R. Ostojic, J. Poole, and P. Proudlock, eds., *LHC Design Report*, vol. 1. Geneva, Switzerland: CERN, June 2004.
- [61] P. Loiez, P. Rakosy, and L. Guiraud, “Beam screens for the LHC beam pipes. Les conduits pour les faisceaux LHC.” Reportnumber: CERN-AC-9705015, May 1997.
- [62] M. Brice, “FCC-hh beam screen prototype,” Apr 2016. General Photo in: CERN-PHOTO-201604-074.
- [63] F. Perez and P. Chiggiato, “Measurement setup at light source operational: Milestone M4.3,” Tech. Rep. CERN-ACC-2016-0110, CERN, Geneva, Aug 2016.
- [64] F. hh design study, “Fcc-hh design study: Machine parameters,” 2017-09-21.
- [65] R. Bailey, G. Von Holtay, N. Hilleret, C. Bovet, M. Tavlet, J. Jimenez, M. Placidi, B. Balhan, B. Goddard, and R. Jung, “Synchrotron radiation effects at lep,” in *Proceedings of the 6th European Particle Accelerator Conference*, (Stockholm, Sweden), June 1998.
- [66] R. Kersevan, “Proposal and simulation of the fcc-ee vacuum system,” in *FCC week 2017*, (Berlin), CERN, 2017.
- [67] F. ee design study, “Fcc-ee design study: Machine parameters,” 2017-09-21.
- [68] “CERN Layout Database.” <https://layout.web.cern.ch>, Accessed in: 2016. sector 45, sector 56.
- [69] “CDD - CERN Drawings Database.” <http://edms-service.web.cern.ch/> edms-service/CDD, Accessed: in 2016. sector 45, sector 56.
- [70] “LHC logging database extracted via TIMBER v6.3.17.” <https://timber.cern.ch/>, Accessed: in 2016.
- [71] E. Novak and H. Wozniakowski, *Tractability of multivariate problems*, vol. 1. EMS, Zürich, 2008.
- [72] L. Kuipers and H. Niederreiter, *Uniform distribution of sequences*. Courier Corporation, 2012.

## BIBLIOGRAPHY

- [73] H. Kesten, “On a conjecture of erdös and szüsz related to uniform distribution mod 1,” *Acta Arithmetica*, vol. 12, no. 2, pp. 193–212, 1966.
- [74] J. Beck, *Strong uniformity*, vol. 15. Berlin: Radon Series on Computational and Applied Mathematics, 2014.
- [75] A. Y. Khinchin, *Continued fractions. English translation of the 3rd Russian Edition*. Chicago: University of Chicago Press, 1964.
- [76] S. Grepstad and G. Larcher, “Sets of bounded remainder for the continuous irrational rotation on  $[0, 1)^2$ ,” *arXiv preprint arXiv:1603.00207*, 2016.
- [77] O. Bohigas, M.-J. Giannoni, and C. Schmit, “Characterization of chaotic quantum spectra and universality of level fluctuation laws,” *Physical Review Letters*, vol. 52, no. 1, p. 1, 1984.
- [78] M. L. Mehta, *Random matrices*, vol. 142. Academic press, 2004.
- [79] J. Harriet, “In theory: Why bother with theoretical physics?,” March 2016.
- [80] F. A. Haight, *Handbook of the Poisson distribution*. Publications in operations research, New York, NY: Wiley, 1967.
- [81] G. Casati, B. Chirikov, and I. Guarneri, “Energy-level statistics of integrable quantum systems,” *Physical review letters*, vol. 54, no. 13, p. 1350, 1985.
- [82] S. project, “Quasi-monte carlo methods: Theory and applications.” <http://www.sfb-qmc.jku.at/>. Accessed: 2017-09-01.
- [83] Z. Rudnick and P. Sarnak, “The pair correlation function of fractional parts of polynomials,” *Communications in mathematical physics*, vol. 194, no. 1, pp. 61–70, 1998.
- [84] S. Grepstad and G. Larcher, “On pair correlation and discrepancy,” *Archiv der Mathematik*, 2017. arXiv preprint arXiv:1612.08008.
- [85] D. Heath-Brown, “Pair correlation for fractional parts of  $\alpha n^2$ ,” in *Mathematical Proceedings of the Cambridge Philosophical Society*, vol. 148, pp. 385–407, Cambridge University Press, 2010.
- [86] J. Marklof and A. Strömbärgsson, “Equidistribution of kronecker sequences along closed horocycles,” *Geometric and Functional Analysis*, vol. 13, no. 6, pp. 1239–1280, 2003.
- [87] Z. Rudnick, P. Sarnak, and A. Zaharescu, “The distribution of spacings between the fractional parts of  $n^2\alpha$ ,” *Inventiones mathematicae*, vol. 145, no. 1, pp. 37–57, 2001.
- [88] J. L. Truelson, “Divisor problems and the pair correlation for the fractional parts of  $n^2\alpha$ ,” *International Mathematics Research Notices*, vol. 2010, no. 16, pp. 3144–3183, 2010.

## BIBLIOGRAPHY

- [89] F. P. Boca, A. Zaharescu, *et al.*, “Pair correlation of values of rational functions (mod p),” *Duke Mathematical Journal*, vol. 105, no. 2, pp. 267–307, 2000.
- [90] I. Berkes, W. Philipp, R. Tichy, *et al.*, “Pair correlations and  $u$ -statistics for independent and weakly dependent random variables,” *Illinois Journal of Mathematics*, vol. 45, no. 2, pp. 559–580, 2001.
- [91] S. Chaubey, M. Lanius, and A. Zaharescu, “Pair correlation of fractional parts derived from rational valued sequences,” *Journal of Number Theory*, vol. 151, pp. 147–158, 2015.
- [92] Z. Rudnick and A. Zaharescu, “A metric result on the pair correlation of fractional parts of sequences,” *Acta Arithmetica*, vol. 89, no. 3, pp. 283–293, 1999.
- [93] T. Tao and V. H. Vu, *Additive combinatorics*, vol. 105. Cambridge University Press, 2006.
- [94] C. Aistleitner, G. Larcher, and M. Lewko, “Additive energy and the hausdorff dimension of the exceptional set in metric pair correlation problems,” *To appear in: Israel J. Math.*, 2016. preprint arXiv:1606.03591.
- [95] G. H. Hardy and J. E. Littlewood, “Some problems of diophantine approximation,” *Acta mathematica*, vol. 37, no. 1, pp. 155–191, 1914.
- [96] W. Greiner, *Quantum mechanics: An introduction*. Springer Science & Business Media, 2001.
- [97] A. Davydov, *Quantum Mechanics*. Oxford: Pergamon, 1965.
- [98] N. P. on Technology Enhanced Learning (NPTEL), “Lecture 4 : The schrödinger wave equation for hydrogen atom.” <http://nptel.ac.in/courses/104103069/module1/lec4/2.html>. Accessed: 2017-09-26.
- [99] Wikipedia, “Atomic orbital.” [https://en.wikipedia.org/wiki/Atomic\\_orbital](https://en.wikipedia.org/wiki/Atomic_orbital). Accessed: 2017-09-26.



---

---

### **Eidesstattliche Erklärung**

Ich erkläre an Eides statt, dass ich die vorliegende Dissertation selbstständig und ohne fremde Hilfe verfasst, andere als die angegebenen Quellen und Hilfsmittel nicht benutzt bzw. die wörtlich oder sinngemäß entnommenen Stellen als solche kenntlich gemacht habe. Die vorliegende Dissertation ist mit dem elektronisch übermittelten Textdokument identisch.

Ida Aichinger  
Genf, Oktober 2017



---

# Curriculum Vitae

---

Ida Aichinger

born on February 27, 1991 in Graz, Austria.

ADDRESS    10, Rue des Hautains  
              01630 St. Genis-Pouilly  
              France  
E-MAIL      [ida.aichinger@cern.ch](mailto:id.aichinger@cern.ch)



## Research Interests

scientific simulation ◊ programming ◊ simulation techniques ◊ mathematics ◊ physics ◊  
particle physics ◊ stochastic numerics ◊ (quasi-) Monte Carlo methods ◊ numerical solvers ◊  
FEM analysis ◊ neuronal networks ◊ artificial intelligence

## Education

- 2014 - 2017 **PhD in Technical Sciences: Industrial Mathematics**, *CERN, CH; JKU Linz, A.*  
2012 - 2014 **MSc in Industrial Mathematics**, with distinction, *JKU Linz, Austria*.  
2009 - 2012 **BSc in Technical Mathematics**, *JKU Linz, Austria*.

## Publications

- July 2017 **Analytical methods for vacuum simulations in high energy accelerators for future machines based on LHC performances**, *I. Aichinger, R. Kersevan, P. Chiggiato*, Physical Review Accelerators and Beams, submitted.
- June 2017 **On Quasi-energy-spectra, pair correlations of sequences and additive combinatorics**, *I. Aichinger, C. Aistleitner, G. Larcher*, 80th birthday festschrift for Ian H Sloan, accepted for a book chapter.
- Oct. 2016 **Sets of Bounded Remainder for the Billiard on a Square**, *I. Aichinger, G. Larcher*, Uniform Distribution Theory, submitted.
- Feb. 2015 **Value at Risk - Mathematische Modellierung des Portfoliowertes mit Monte-Carlo-Simulationen**, *I. Aichinger*, AkademikerVerlag, published.

## Conferences

- May 2017 **FCC week 2017, Berlin, Germany**, Poster: “Pressure profile in the experimental areas of FCC hh and ee, calculation by an analytical code”.
- April 2016 **FCC week 2016, Rom, Italy**, Talk: “Simulation of the Evolution of the Residual Gas Particle Density – an Analytical Approach”.
- July 2015 **The Tenth IMACS Seminar on Monte Carlo Methods (MCM 2015), Linz, Austria**, participation.

## Schools and Courses

- June 2017 **Graz Summer School on Applications of Quasi-Monte Carlo methods, 3 days**, TU Graz, Austria.
- Apr. 2017 **Scientific writing - getting started, 16 hours**, CERN, Switzerland.
- Mar. 2017 **Convincing Scientific Presentations, 16 hours**, CERN, Switzerland.
- Nov. 2016 **Python: Advanced Hands-On, 32 hours**, CERN, Switzerland.
- Sep. 2016 **Magnetization measurements of superconductors, 4 hours**, CERN, Switzerland.
- Feb. 2016- **Joint Universities Accelerator School: The technology and applications of particle accelerators, 5 weeks**, Archamps, France.
- Mar. 2016 **Joint Universities Accelerator School: The science of particle accelerators, 5 weeks**, Archamps, France.
- Jan. 2016- **Joint Universities Accelerator School: The science of particle accelerators, 5 weeks**, Archamps, France.
- May, 2015 **13th IUVSTA School on Vacuum Gas Dynamics: Theory, Experiments and Applications, 4 days**, Thessaloniki, Greece.
- Jan. 2015 **AXEL: Introduction to Particle Accelerators, 15 hours**, CERN, Switzerland.
- Fall 2014 **General and Professional French courses, 60 hours**, CERN, Switzerland.
- 2014-2017 **Official PhD reports, biweekly**, CERN, Switzerland.

## Computer skills

- |                                 |  |
|---------------------------------|--|
| Python                          | Analytical vacuum model (3 years), CERN, Switzerland.                        |
| C++                             | Development of a finite element solver for PDE (2 years), JKU Linz, Austria. |
| Mathematica, Matlab             | Regular use, full proficiency.   |
| L <sup>A</sup> T <sub>E</sub> X | Regular use to write documents and presentations.                            |
| methods                         | version-control (Git, Mercurial), unit testing and GUI (PyQt).               |

## BIBLIOGRAPHY

### Internships

- Feb. 2012 - 2014 **Association of mathematical talent promotion**, Kefermarkt, Austria,  
*Scientific assistant*, 3 weeks.
- Summer 2012 **DMCE, subsidiary of INTEL**, Linz, Austria,  
*Statistical analysis*, Division of telecommunication, 8 weeks.
- Summer 2011 **Au-pair 4you**, London, United Kingdom  
*Au-pair*, 7 weeks.
- Summer 2009-  
Summer 2010 **Österreichische Post**, Asten, Austria,  
*Operator*, 16 weeks.
- Summer 2008 **Hubauer GmbH**, St. Florian, Austria,  
*Geometrical computations*, Division of hydraulic lifting equipments, 4 weeks.
- Summer 2007 **Kindergarten**, Asten, Austria,  
*Supervisor*, 3 weeks.
- Summer 2006 **Pharmacy**, Linz, Austria,  
*Assistant*, 3 weeks.

### Language Skills

- German Mother tongue.
- English **C1**, full professional proficiency.
- French **B1**, limited professional proficiency.

### Volunteering

- 2017 Volunteer for EUCAS (European Conference on Superconductivity), CERN, Geneva.
- 2015-2017 Participation in Q&A for Austrian teacher and student program, CERN, Geneva.
- 2015 Participation in FCC gender equality interviews, CERN, Geneva.
- 2008 Committee member of the graduation ball, BRG Enns, Austria.

### Hobbies

- Sports Alpinism, skiing, climbing, running, ice hockey, volley ball, yoga.
- Music Guitar (classical and modern), choir.